STUDIA UNIVERSITATIS
BABEŞ-BOLYAI

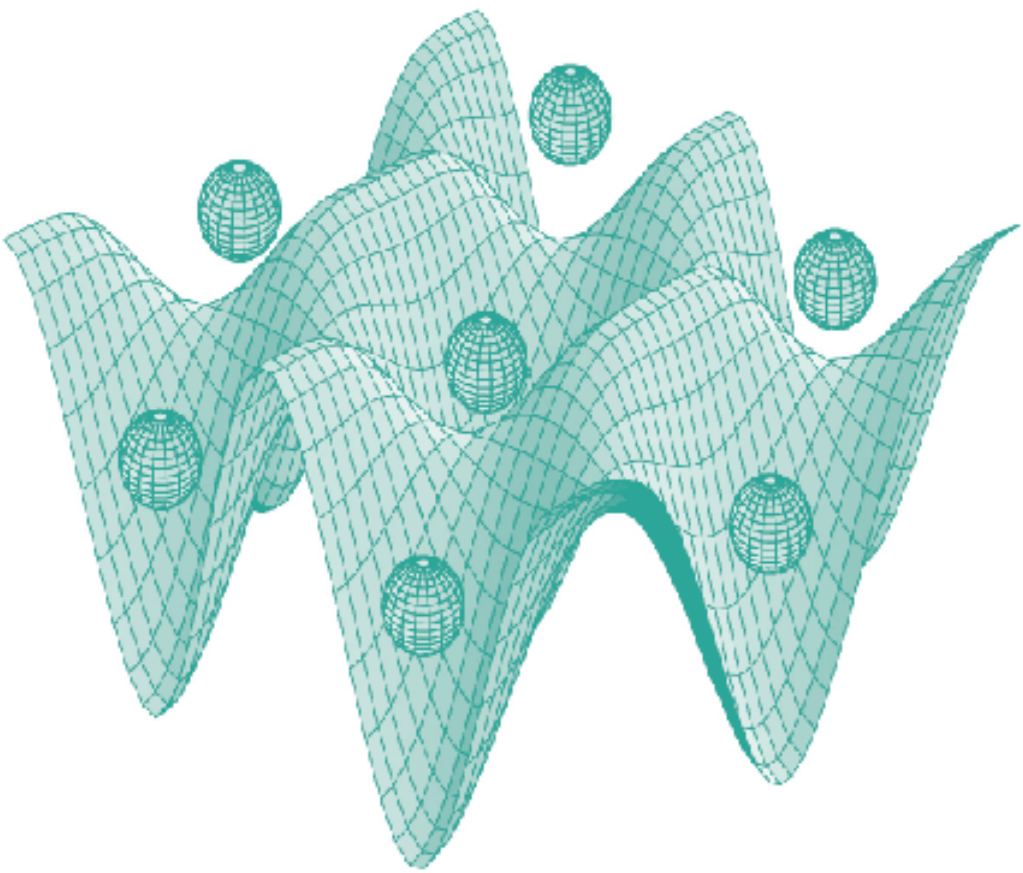

PHYSICA

1/2016

STUDIA
UNIVERSITATIS BABEŞ-BOLYAI
PHYSICA

1/2016

June

EDITORIAL OFFICE OF STUDIA UBB PYSICA:
1, M. Kogălniceanu St., Cluj-Napoca, ROMANIA, Phone: +40 264 405300
http://www.studia.ubbcluj.ro/serii/physica/index_en.html

YEAR **Volume 61 (LXI) 2016**
MONTH **JUNE**
ISSUE **1**

S T U D I A
UNIVERSITATIS BABEŞ–BOLYAI

PHYSICA

1

Dedicated to Professor Dr. Cozar Onuc on His 70th Anniversary

STUDIA UBB EDITORIAL OFFICE: B.P. Hasdeu no. 51, 400371 Cluj-Napoca, Romania, Phone + 40 264 405352

CUPRINS – CONTENT – SOMMAIRE – INHALT

STUDIA UBB PHYSICA, Vol. 61 (LXI), 1, 2016, pp. 5-7
(RECOMMENDED CITATION)

Foreword

Anniversary of Professor Onuc Cozar

Professor Onuc Cozar was born in 1946, march 29, Sancraiu-Almasului, Salaj.

He graduated Babes-Bolyai University Cluj-Napoca in 1970. Since 1972 worked at "Babes-Bolyai" University, Faculty of Physics, first as teaching assistant (1970-1983), assistant professor (1983-1990) and professor (1990-present), respectively.

Prof. Onuc Cozar earned in 1979 his PhD in Physics with thesis "Molecular structure and adsorption dynamics of some Cu(II) complexes determined by EPR spectroscopy**"**.

Prof. O. Cozar was visiting professor at: University of Padova (1993), U.N.E.D. Madrid (1996), Univ. Claude Bernard Lyon (1999, 2002, 2005) and Technical University Aachen (2003), respectively.

Professor Onuc Cozar presented courses, lectures and laboratory for disciplines: Physics of atoms and molecule, Nuclear Physics, Molecular Symmetry, Dosimetry and Radiation Protection, Detection of nuclear radiation and Nuclear spectroscopy. Understanding the importance of modern directions in science, he introduced new courses. In the framework of Master of Science Program he has been involved in teaching advanced courses in Resonance methods with biomedical applications and Complements of physics of molecule. At doctoral school presented lectures on Methods and theoretical models in atomic physics. In the position of PhD coordinator he supervised 29 theses (of which 3 in joint supervision with Claude Bernard University, Lyon).

The courses are very clearly presented and at high scientific level, and the teaching activities performed by Prof. Onuc Cozar are much appreciated by the students.

The scientific activities of Prof. Onuc Cozar were directed particularly the:

- Structure and molecular dynamics;
- The interaction between metallic paramagnetic ions with some compounds of biomedical interest (drugs, aminoacids, nucleotides);
- Solvent effects and molecular association mechanisms;
- The identification of the irradiation products in different biomolecules – their kinetics;

- Estimation of the structures and molecular properties using non-empirical methods (DFT); EPR on paramagnetic coupled systems (clusters);

- Local structure and interaction between paramagnetic ions in oxide matrices;

- Applications of physical methods in medical diagnosis and therapy.

The scientific results of Prof. Onuc Cozar were published in 466 papers, 200 being in ISI quoted journals (J. Molec. Structure, Chem. Physics, Vibrational Spectroscopy, J. Mass Spectrometry, Appl. Magn. Resonance, J. Chem. Soc. Dalton Transaction, J. Raman Spectroscopy etc.). Around 27 papers were published in Romanian ISI Journals and international ISI Proceedings, 42 papers in non ISI International Journals, 173 papers in Romanian Journals of Physics, 52 papers in Proceedings of other International and National Conferences. He has Hirsch indices H=21 (Scopus).

His theoretical and experimental researches as well as his pedagogic experience were fructified into a series of 16 books, frequently used by the students in area of their courses. These are remarkable for their accuracy and clarity as well as scientific level the monography "Electron spin resonance for metallic complexes" (Romanian Academy Publishing Houses-Bucharest 2001).

Professor Onuc Cozar is member of many Romanian and international scientific societies as: Romanian Physical Society, Romanian Society for Radioprotection, Romanian Society of Magnetic Materials, European Physical Society, Balkan Physical Society, International Society of Resonance (ISMAR), Ampere Group, American Association of Physicist in Medicine (AAPM).

He has done extensive research in management sciences, holding several management positions: Dean of the Faculty pf Physics, Cluj-Napoca (2007 – 2011), Head of the Research Center "Molecular systems of biomedical and environmental interest" (2001 - 2011), Member of the First Exact Sciences Commision, CNEAA – Bucharest (1998 - 2006), Head of Atomic, Nuclear and Environment Department, Faculty of Physics (1990 - 2003), Member of Scientific Research Council of "Babes-Bolyai" University (1998 - 2002), Scientific Secretary of Faculty of Physics (1996 - 2000).

Professor O. Cozar has extensive experience in the management of national / international scientific projects, gaining over 33 scientific contracts and grants.

Professor O. Cozar is member of the Editorial Board of some Romanian Journals (Studia UBB Physica, "Babes-Bolyai" University Cluj, Annals of the Timișoara, University and Oradea University-Series Physics) and Reader to a series of international scientific journals.

Professor Onuc Cozar, member of Academy of Romanian Scientists, has been awarded by Romanian Academy and by "Babes-Bolyai" University (11 diploma of excellence and professor emeritus in 2012), respectively. He was involved in scientific

programs with University Claude Bernard Lyon (France), University of Padova (Italy), University of Aachen (Germany).

He was invited to sustain plenary presentations at many national and international meetings and conferences. Professor O. Cozar organized several national and international conferences, symposiums and summer school as: National symposium on solid state physics (1978, Cluj-Napoca), Symposium: methods, models and technics in physics and related fields (Cluj-Napoca in 1982, 1984, 1986), The Conference of Isotopic and Molecular Processes (Cluj-Napoca in 1999, 2001, 2003, 2005, 2007). The 5th Conference on Medical Physics of ARFM (Cluj-Napoca, Romania, 25-27 oct. 1995), Summer School "The Physics of Radiation Therapy" (10-14 June 1999, Cluj-Napoca, Romania), Ecole d'été „Methodes avancées d'analyse spectroscopique. Aplications" (25 Aug. – 3 Sept. 2001, Cluj-Napoca, Romania), Applications of FT-IR, FT-Raman and Micro-Raman Techniques to Physical, Chemical, Biological, Medical and Environmental Research, Workshop (28-29 May, 2002, Cluj-Napoca, Romania), Advanced Spectroscopies on Biomedical and Nanostructured Systems, (NANOSPEC) (Cluj-Napoca, Romania, 2004, 2006, 2008, 2011), The 31st European Congress on Molecular Spectroscopy. EUCMOS (2012, Cluj-Napoca).

Today, at seventy years old, Prof. Onuc Cozar is surrounded by researchers which continue his scientific activity.

Happy birthday and all the best!

Prof.dr. Aurel Pop
Dean-Faculty of Physics

STUDIA UBB PHYSICA, Vol. 61 (LXI), 1, 2016, pp. 9-19
(RECOMMENDED CITATION)

Dedicated to Professor Dr. Cozar Onuc on His 70th Anniversary

UV-VIS PH DEPENDENCE OF DACARBAZINE: EXPERIMENTAL AND TD-DFT INVESTIGATIONS

MIHAELA CHIŞ[a], MONICA BAIA[a,b], CĂLIN CĂINAP[c], VASILE CHIŞ[a]*

ABSTRACT. Dacarbazine (DTIC) is one of the most used chemotherapeutic drugs in the treatment of patients with metastatic malignant melanoma. Depending on the pH of the solution, different conformers or tautomers of the drug are expected to exist, eventually with different biological activities. In this study the UV-Vis absorption spectroscopy coupled with quantum chemical calculations were used to get new insights about the molecule's structure and the pH influence on the absorption spectra of dacarbazine. The attention was focused on the possible conformers and tautomers of the molecule, on their stability and energetic order in gas-phase as well as in liquid state. Correlating the experimental UV-Vis data and Time dependent density functional theory (TD-DFT) computational results the conformers of DTIC, which are responsible for the absorption spectrum in water at different pH values, were identified. Subtle features of the absorption spectrum of DTIC were reliably explained using proper computational models and techniques. By using convergent approximations the experimental UV-Vis spectrum of dacarbazine was reproduced within the experimental errors. The changes that appear in the absorption spectra as a result of a pH change, have been attributed to the presence of protonated and deprotonated species of DTIC present in acidic and alkaline solutions, respectively.

Keywords: *dacarbazine, UV-Vis, pH, TD-DFT*

1. INTRODUCTION

Dacarbazine (5-(3,3-dimethyltriazeno)imidazol-4-carboxamide, DTIC), is one of the most researched chemotherapeutic drugs used in the treatment of patients with metastatic malignant melanoma [1]. Dacarbazine's mode of action is still uncertain, but

[a] *Babeş-Bolyai University, Faculty of Physics, M. Kogălniceanu 1, 400084 Cluj-Napoca, Romania*
[b] *Babeş-Bolyai University, Interdisciplinary Research Institute on Bio-Nano-Sciences, T. Laurian 42, 400027, Cluj-Napoca, Romania*
[c] *The Oncology Institute "Prof. Dr. Ion Chiricuță", Republicii 34-36, 400015 Cluj-Napoca, Romania*
* *Coresponding author: vasile.chis@phys.ubbcluj.ro*

most sources state that this drugs works similar to other cytotoxic drugs classified as „alkylating agents". These agents stop the cancer cells from multiplying by binding together the strands of the cell's genetic material. This makes the strands unable to uncoil and separate, which is necessary in DNA replication. As a result, the cells can no longer divide and therefore they die. The faster the cells are dividing, the more likely it is that chemotherapy will kill the cells, causing the tumor to shrink [2].

Considering the importance of this drug in chemotherapy, in the present study we used UV-Vis absorption spectroscopy coupled with quantum chemical calculations based on density functional theory (DFT) to get new insights about the molecule's structure.

It is known that depending on pH value of the solution, different conformers or tautomers of a drug are expected to have different biological activities [3]. Moreover, a study by Saunders et al. [4] shows that dacarbazine's toxicity is dependent on illumination and also greatly affected by the pH of the environment. Therefore, the pH influence on the absorption spectra of DTIC was further investigated. The lowest energy conformers of DTIC have been identified by DFT calculations. Our attention was focused on the possible conformers and tautomers of the molecule, on their stability and energetic order in gas phase as well as in liquid state. Subsequently, the corresponding optimized geometry was used for electronic structure calculations. Quantum chemical calculations performed in the framework of DFT enabled us to explain in detail the experimentally derived data.

2. EXPERIMENTAL

Materials and Methods

For the experimental measurements, dacarbazine powder was purchased from Sigma Aldrich, and used as received without any further purification.

The UV-Vis spectra were firstly recorded for aqueous solutions at different concentrations (ranging from 10^{-4} M to 10^{-6} M) and at normal pH value, and secondly at a concentration of 10^{-5} M for different pH values in the range between 2 and 13.

The desired concentrations for the measurements were obtained from an initial stock solution with a concentration of 10^{-2} M. For preparing the aqueous solutions, ultrapure water was used. The samples were stored at room temperature in plastic recipients wrapped in aluminum foil. The pH of the solutions was changed by adding small amounts of 1% solutions of hydrochloric acid (HCl) or sodium hydroxide (NaOH).

The UV-Vis spectra were recorded using a Jasco V630 UV-Vis double beam spectrophotometer with a silicon photodiode detector. The samples were placed in 1 cm path length quartz cuvettes, in a distilled water solution. The spectra were recorded in the 190-1100 nm range.

Computational Details

Density functional theory (DFT) calculations were employed in order to obtain the optimized geometries of the investigated compounds. As starting geometries for energy minimizations, we used the X-ray structures derived from crystallographic data reported by Freeman and Hutchinson [5]. The calculations on monomers and dimers were performed at B3LYP/6-31+G(2d,2p) level of theory, with and without dispersion correcting potentials (DCPs) on the atoms of molecule, according to the procedure proposed by DiLabio's group [6].
The absorption spectra were calculated using the TD-DFT formalism and the solvent effects were accounted for by using the Polarizable Continuum Model (PCM) [7]. The conformer energies, molecular structures and the absorption spectra calculations were performed by using the Gaussian package [8].

3. RESULTS AND DISCUSSION

3.1. Tautomers and conformers stability

When investigating a drug, the dissimilarities in biological activities arising from different conformers or tautomers of the same drug must be taken into consideration. Combining experimental techniques and quantum chemical calculations is an adequate approach to answer for the high interest in structural and spectroscopic characterization of a given drug [3].

Thus, our first interest was to investigate the stability of the possible tautomers and conformers of dacarbazine. The starting geometries used for the structure optimizations, were derived from the X-ray diffraction data reported by Freeman and Hutchinson [5]. This data shows the existence of two tautomers in the asymmetric unit (Fig. 1). The difference between them is related to the position of the second hydrogen in the imidazole ring. In one molecule, the protonated nitrogen of the imidazole ring is adjacent to the triazene group, while in the other one it is adjacent to the carboxamide group.

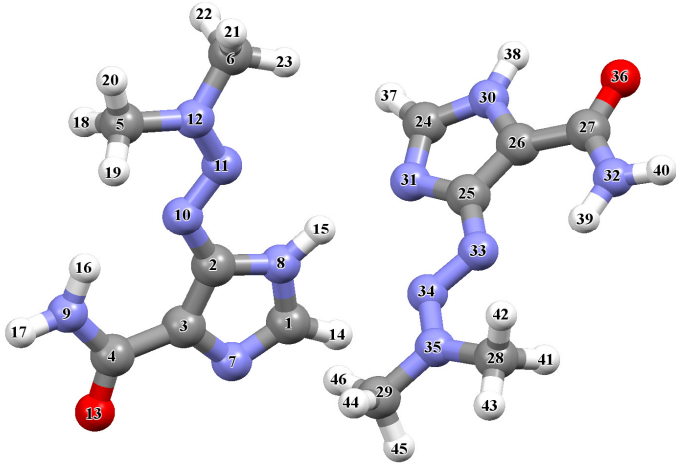

Figure 1. Optimized dimeric structure of DTIC as obtained from the crystallographic data.

We started by investigating the energetic stability of the possible tautomers and conformers of dacarbazine. For this purpose, we used a B3LYP exchange-correlation functional and the 31+G(2d,2p) basis set. The theoretical simulations for geometry optimization were carried out on both tautomers revealed by the crystallographic data (m1_cx and m2_cx), two conformers and one tautomer of m1 (denoted m1_c2, m1_c3 and m1_c2_t2), as well as two conformers of m2 (denoted m2_c2 and m2_c3). The geometry for the conformers is dependent on the orientation of the carboxamide or the triazene groups around the imidazole ring connective bond (Fig. 2).

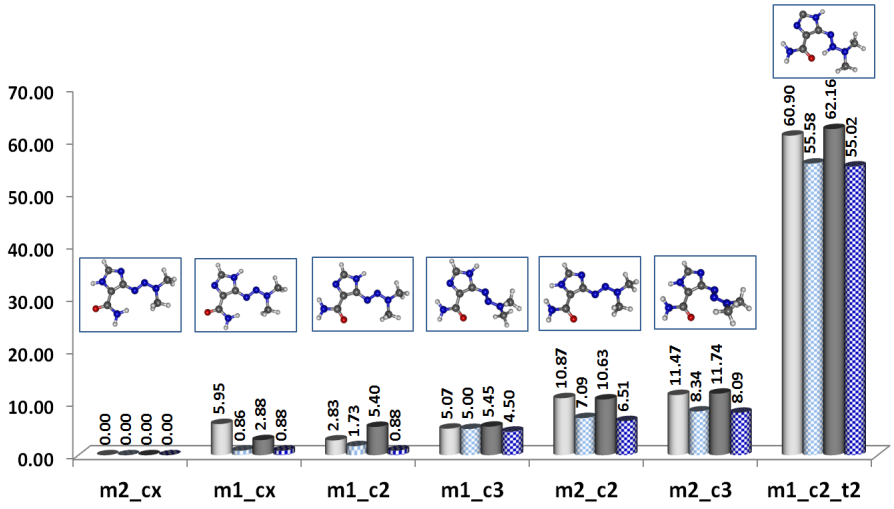

Figure 2. B3LYP/6-31+G(2d,2p) optimized geometries and relative energies (ΔE – light color, ΔG – dark color) of the DTIC monomers in vacuo (full fill) and water (squared fill).

All the optimizations were performed firstly in gas-phase, and then, by considering water as a solvent. To account for the interaction between the drug molecule and water, we used the Polarizable Continuum Model (PCM) [7].

In order to find the most stable conformer, in other words for the energetic order characterization, we used the relative energies (ΔE) but also the relative Gibbs free energies (ΔG), the last quantity being very recently recommended for such analyses and for calculating the relative Boltzmann populations [9].

Our results suggest that m2_cx monomer is more stable than the other structures in both gas-phase and in water. Structure optimizations show that water considerably stabilizes all geometries and an important difference is noticed between the gas-phase and the liquid state of m1_cx and m2_cx. The ΔG values of the three most stable geometries, with respect to the m2_cx are identical in water (0.88 kcal mol^{-1}) with relative Boltzmann populations of 15.4 %, while that of m2_cx is 69.1 %. All the other investigated conformers and tautomers have negligible populations with respect to the three most stable ones (Table 1).

Table 1. Relative free Gibbs energies and Boltzmann populations at room temperature for all conformers

Conformer	Relative Gibbs free energy in water (kcal/mol)	Boltzmann population at RT (%)
m2_cx	00.00	69.14
m1_cx	0.88	15.41
m1_c2	0.88	15.41
m1_c3	4.5	0.03
m2_c2	6.51	0.00
m2_c3	8.09	0.00
m1_c2_t2	55.02	0.00

The small relative Gibbs energy of the m1 and m2 tautomers in water points to the possibility of coexistence of these structures in water solutions since their structural interconversion could be activated at room temperature. Thus, the spectroscopic response of DTIC in water solution must be explained considering the contribution coming from both m2_cx and m1_cx tautomers.

3.2. Absorption spectrum of dacarbazine

Next, the absorption spectrum of dacarbazine was investigated by correlating the experimental results with the theoretical ones. For this purpose the calculations were performed by using the TD-DFT approach. By using convergent approximations, we were able to reproduce the experimental UV-Vis spectrum of DTIC within the experimental errors.

As observed in Fig. 3, the experimental absorption spectrum shows two peaks: one at 328 nm, representing the electronic transition between the ground and the first allowed excited state, and the second one at 236, assigned to a transition between the ground and the second allowed excited state. Both absorption peaks preserve their shape or position, when changing the concentration of DTIC in solution.

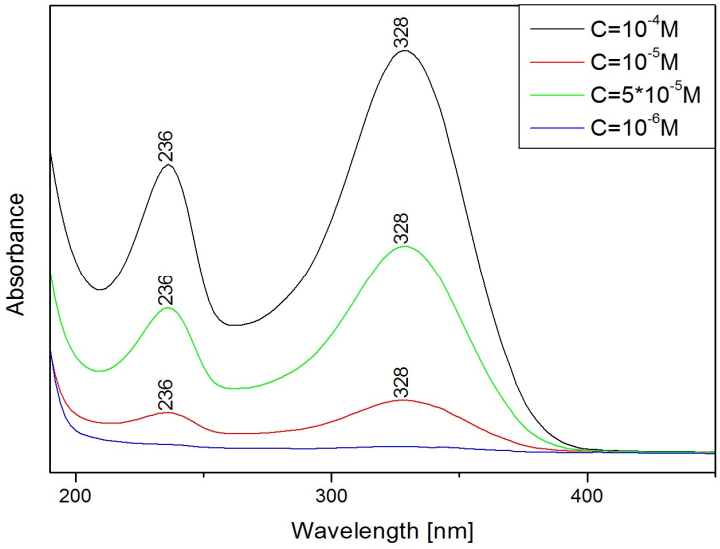

Figure 3. UV-Vis absorption spectrum of dacarbazine in water at different concentrations as indicated.

Subsequently, we investigated the absorption peaks in the UV-Vis spectrum and analyzed the excited states involved in these transitions. The necessary calculations were performed at B3LYP/6-31+G(2d,2p) level of theory on both tautomers found in solid state and the m1_c2 conformer, whose stability has been discussed in the previous section.

The obtained results reproduce the excitation energies values for all three monomers. Particularly, we were able to obtain an excellent agreement between the experimental energy of the first excited state at 328 nm and the calculated one at 324 nm. For the second transition, observed at 236 nm the calculated bands are found at 219, 224 and 231 ((228+233)/2) nm for the gas-phase m1_cx, m1_c2 and m2_cx monomers, respectively (Table 2). Therefore, for the gas-phase, we can state that a better agreement between experiments and TD-DFT calculations is obtained for m1_cx for the first excited state, and for m2_cx for the second excited state.

Table 2. Calculated electronic transition of dacarbazine in gas-phase and water at B3LYP/6-31+G(2d,2p) level of theory. Theoretical values (λ_{teor}) compared to experimental values (λ_{exp})

Gas phase					
System	**λ_{teor} (nm)**	**λ_{exp} (nm)**	**f**	**Transitions**	**Orbital Contributions**
m2_cx	298	328	0.53	H-L	98%
	233	236	0.11	H-4-L	61%
	228	236	0.18	H-3-L	40%
Water					
System	**λ_{teor} (nm)**	**λ_{exp} (nm)**	**f**	**Transitions**	**Orbital Contributions**
m1_cx	323	328	0.61	H-L	90%
	224	236	0.20	H-4-L	73%
m1_c2	320	328	0.68	H-L	99%
	224	236	0.18	H-4-L	76%
m2_cx	310	328	0.62	H-L	99%
	232	236	0.28	H-3-L	79%

The theoretical data obtained for the two monomers in water shows that the solvent affects very slightly the energy of the first excited state for m1_cx. However, for m2_cx we can observe a better agreement with the experiment, the new calculated transition energy being 310 nm. This is also true for the second transition whose calculated energy (232 nm) is also in better agreement with the experimental value (236 nm).

The calculated transition energies for both excited states are influenced more by considering the solvent effects in case of m2 monomer than for m1. It is also worth noting that the molecular orbitals involved in the transition corresponding to the first excited state are HOMO and LUMO, for both m1 and m2 monomers. The second excited state involves basically the transitions HOMO->LUMO+4, HOMO-4->LUMO or HOMO-LUMO+1. These orbitals are depicted in Fig. 4.

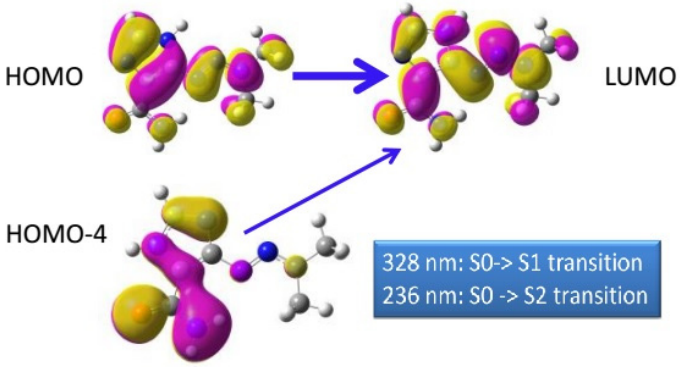

Figure 4. Molecular orbitals involved in the transition corresponding to the first and second electronic excited states of dacarbazine.

3.3. Dacarbazine – UV-Vis spectrum – pH dependence

The UV-Vis spectra of DTIC water solutions at different pH values were recorded in the 2-13 pH range (Fig. 5). With increasing the pH values the spectra exhibit considerable changes. We can easily observe the appearance of a new band located at 204 nm (pH 13) in addition to a red shift of the bands associated to the first and second excited states. Thus, the first band shows a displacement from 322 nm at pH=2 to 342 nm at pH=13. The second band shifts from 222 to 248 nm.

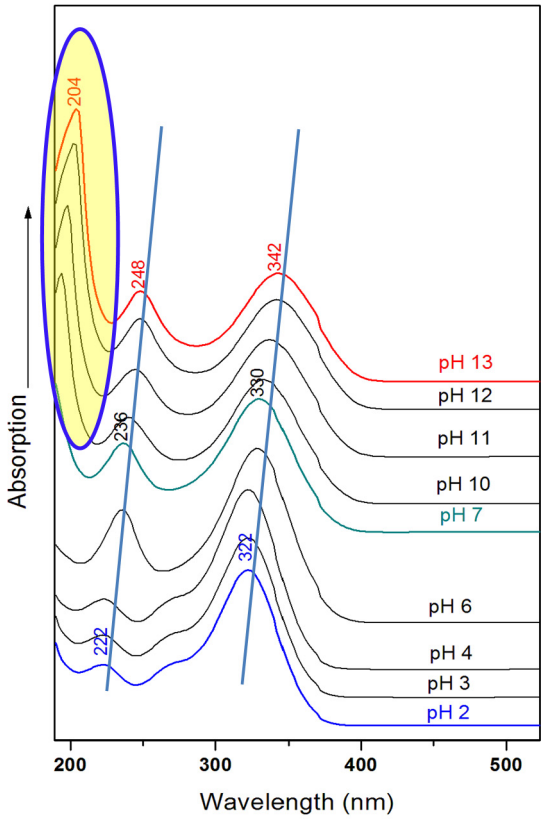

Figure 5. pH dependent UV-Vis spectra of dacarbazine in water.

We assume that this shift can be due to the presence of different molecular species of dacarbazine depending on the pH of the solution. Thus, by decreasing the pH value of the solution the protonated species are predominant, while after increasing the pH value the deprotonated species become predominant (Fig. 6).

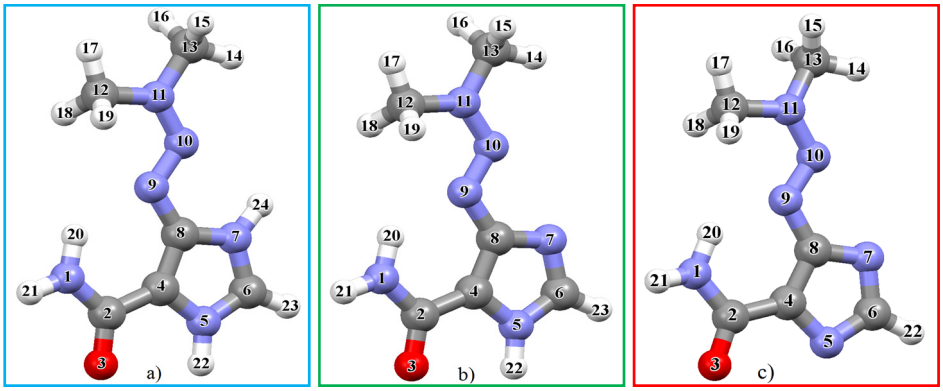

Figure 6. Species of the m2 conformer of dacarbazine found at different pH values: a) protonated; b) neutral; c) deprotonated.

To verify this hypothesis, we calculated the UV-Vis spectra for both protonated and deprotonated species. The results completely explain the experimental data (Fig. 7). Thus, we can observe a red shift of the entire spectrum for the deprotonated species, and a blue shift for the protonated ones. Moreover, as one can see from Fig. 7 the calculations reproduce not only the shifts of the transitions but also their relative intensities.

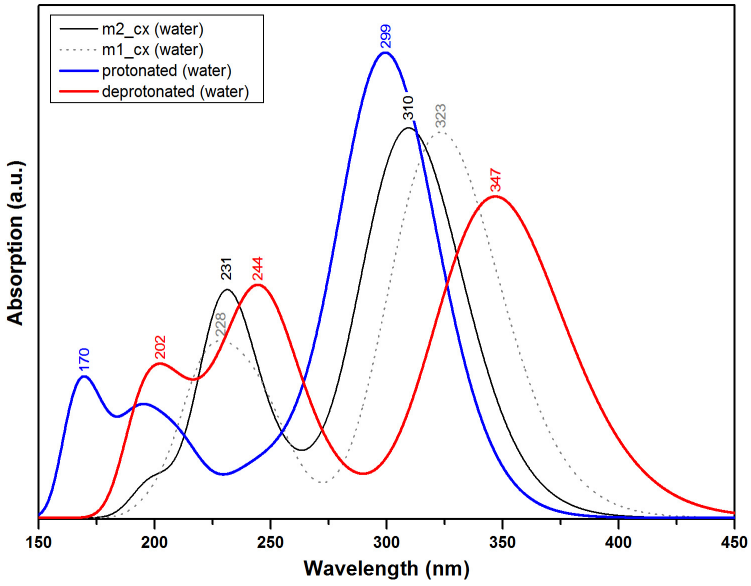

Figure 7. Calculated absorption spectra of pH dependent species of dacarbazine.

4. CONCLUSIONS

The herein presented results clearly demonstrate that there is need for a careful analysis of all possible conformers and tautomers of a drug's molecule as different conformations can give different spectroscopic responses. Special attention must be paid especially before any analysis of the liquid spectra.

The UV-Vis absorption measurements of aqueous solutions at several pH values correlated to TD-DFT calculations enabled us to give an assignment for the electronic transitions corresponding to the observed bands. Excellent agreement between the experimental UV-Vis data and TD-DFT results has been obtained considering the Boltzmann populations averaged molecular properties. In order to achieve a reliable assignment of UV-Vis spectra, it is necessary to take into consideration the solvent effects and the selection of the corresponding molecular models. Additionally, we identified the species that appear as a result of pH changes of the solution, namely protonated species at low pH values, and deprotonated species at high pH values.

REFERENCES

[1] A.M.M. Eggermont, J.M. Kirkwood, Re-evaluating the role of dacarbazine in metastatic melanoma: what have we learned in 30 years?, *Eur. J. Cancer*, 40 (2004) 1825–1836.

[2] G.P. Warwick, The mechanism of action of alkylating agents, Cancer Res, 23 (1963), 1315-1333.

[3] Balsamo A., Crotti P., Lapucci A., Macchia B., Macchia F., Del Tacca M., Mazzanti L., Ceserani R., Conformational effects on the activity of drugs. 7. Synthesis and pharmacological properties of 2-(p-nitrophenyl)-substituted morpholines, *J. Med. Chem.*, 22 (1979), 738-41.

[4] P. Saunders, W. DeChange, L. Chao, Mechanisms of 5-(3,3-dimethyl-1-triazeno)imidazole-4-carboxymaide (dacarbazine) cytotoxicity toward chinese hamster ovary cells in vitro are dictated by incubation conditions, *Chem. Biol. Interactions,* 58 (1986) 319–331.

[5] H.C. Freeman and D. Hutchinson, The Crystal Structure of the Anti-Tumor Agent 5-(3,3-Dimethyl-l-triazenyl)imidazole-4-earboxamide (NSC-45388), *Acta Cryst*., B35 (1979), 2051-2054.

[6] E. Torres, G.A. DiLabio, (Nearly) Universally Applicable Method for Modelling Noncovalent Interactions Using B3LYP, *J. Phys. Chem. Lett*., 3 (2012) 1738−1744.

[7] B. Mennucci, J. Tomasi, R. Cammi, J.R. Cheeseman, M.J. Frisch, F.J. Devlin, S. Gabriel, P.J. Stephens, Polarizable Continuum Model (PCM) Calculations of Solvent Effects on Optical Rotations of Chiral Molecules, *J. Phys. Chem. A*, 106 (2002), 6102-6113.

[8] Gaussian 09, Revision E.01, M.J. Frisch, G.W. Trucks, H.B. Schlegel, G.E. Scuseria, M.A. Robb, J.R. Cheeseman, G. Scalmani, V. Barone, B. Mennucci, G.A. Petersson, H. Nakatsuji, M. Caricato, X. Li, H.P. Hratchian, A.F. Izmaylov, J. Bloino, G. Zheng, J.L. Sonnenberg, M. Hada, M. Ehara, K. Toyota, R. Fukuda, J. Hasegawa, M. Ishida, T. Nakajima, Y. Honda, O. Kitao, H. Nakai, T. Vreven, J.A. Montgomery, Jr., J.E. Peralta, F. Ogliaro, M. Bearpark, J.J. Heyd, E. Brothers, K.N. Kudin, V.N. Staroverov, R. Kobayashi, J. Normand, K. Raghavachari, A. Rendell, J.C. Burant, S.S. Iyengar, J. Tomasi, M. Cossi, N. Rega, J.M. Millam, M. Klene, J.E. Knox, J.B. Cross, V. Bakken, C. Adamo, J. Jaramillo, R. Gomperts, R.E. Stratmann, O. Yazyev, A.J. Austin, R. Cammi, C. Pomelli, J.W. Ochterski, R.L. Martin, K. Morokuma, V.G. Zakrzewski, G.A. Voth, P. Salvador, J.J. Dannenberg, S. Dapprich, A.D. Daniels, Ö. Farkas, J.B. Foresman, J.V. Ortiz, J. Cioslowski, and D.J. Fox, Gaussian, Inc., Wallingford CT, 2009.

[9] P.H. Willoughby, M.J. Jansma, T.R. Hoye, A guide to small-molecule structure assignment through computation of (^{1}H and ^{13}C) NMR chemical shifts, *Nature Protoc*., 9 (2014) 643-660.

STUDIA UBB PHYSICA, Vol. 61 (LXI), 1, 2016, pp. 21-26
(RECOMMENDED CITATION)

Dedicated to Professor Dr. Cozar Onuc on His 70th Anniversary

EPR STUDY OF ORGANICALLY-GROWN VERSUS GREENHAOUSE STRAWBERRIES

I. CSILLAG[a] and G. DAMIAN[a,*]

ABSTRACT. EPR spectroscopy was used to characterize changes in main paramagnetic components (Fe^{3+}, free radical, Mn^{2+}) and antioxidant capacity of two types of strawberries (grown in the greenhouse and in natural conditions). The results of studied samples show the interpretable differences between the analyzed samples, which may be consequences of different types of biochemical processes involved in the growth and maturation of fruits depending on the environmental conditions in which they are grown.

Keywords: *strawberry, EPR spectroscopy, antioxidant capacity*

INTRODUCTION

Scientific research on food quality and nutritional extracts are targets of major importance, both in commercial terms and on their impact on human health [1,2] One of the most common questions about fruits and vegetables in the market, is to detect in those grown in the greenhouse or organically [3].

Most organic greenhouse fruits and vegetables are grown in soil amended with compost and organic fertilizers. But these amended soils do not contain the full range of elements and substances essential [4]. This can have a significant impact on nutritional quality of fruits and vegetables used in the human diet. Growers in of natural organic matter can enhance soil structure, improve the water-holding capacity of the soil, and as a source of high quality nutrients. Therefore, organic foods are much preferred in worldwide because they are free of diseases pure and possess good physiochemical features [5].

[a] *Babeş-Bolyai University, Faculty of Physics, 1 Mihail Kogalniceanu str., 400084, Cluj-Napoca, Romania*
[*] *Corresponding author: grigore.damian@phys.ubbcluj.ro*

What are the differences can be measured spectroscopically? Different research methods follow some characteristic features and allow qualitative and quantitative evaluation of specific parameters [6, 7]

In our work we try to find an answer of this question, by using EPR spectroscopy for two types of strawberries, namely grown in the greenhouse and in natural conditions (organically). Strawberries with remarkable content of antioxidants and phytonutrients with anti-inflammatory role, protect the heart and reduce oxidative stress, preventing damage blood vessels in the body [8,9,10]. Among all healthy fruits, strawberries have the highest level of vitamin C. After raspberries and grapes, these fruits are known as one of the best sources of manganese. As we know, manganese is an important antioxidant mineral, because of its key role as a trace element that is part of composition of the enzyme superoxide dismutase, powerful free radical scavenger that prevents cell damage and helps cell regeneration. In addition, strawberries is a rich source of B vitamins, especially folic acid and vitamin B6 and several essential minerals (such as iron, calcium, magnesium) [11]. EPR spectroscopy has been able to characterize changes in main paramagnetic components, which may be consequences of different types of biochemical processes involved in the growth and maturation of fruits.

EXPERIMENTAL

Freeze-dried two types of strawberries fruits (grown in the greenhouse and organically) and their fresh juice we have analyzed in terms of EPR structure and antioxidant activity. EPR measurements were performed on a Bruker EMX spectrometer operating in X band (~ 9 GHz) with 100 kHz modulation frequency, at room temperature. Antioxidant activity was measured according to their ability to scavenge 2,2'-azinobis(3-ethylbenzothiazoline-6-sulfonic acid) radical cation ($ABTS^+$) in the reaction mixture. 100 μl $ABTS^+$ solution was added in 20 μl strawberry juice.

The homogenized solution was injected with a Hamilton microsyringe into a quartz capillary of about 10 cm length and an interior diameter about 1 mm. The rate of reaction between antioxidant compounds and $ABTS^+$ was monitorised by using normalized double integrated residual EPR signal which is correlated with number of paramagnetic species in time [14]. The integral intensities of EPR spectra were obtained by evaluating their double integrals using Origin8 software.

RESULTS AND DISCUSSION

EPR spectra of lyophilized strawberries are shown in Figure 1.

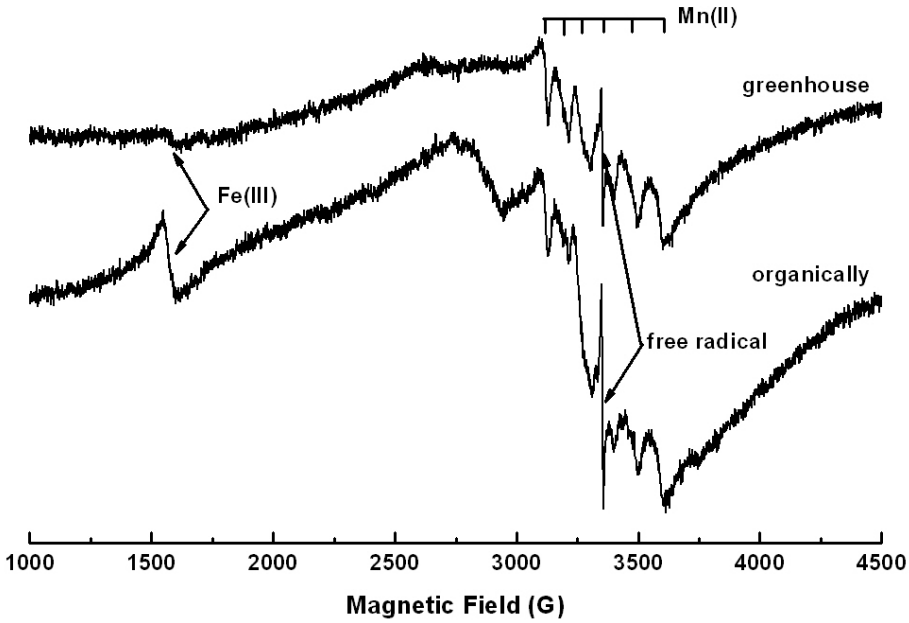

Figure 1. EPR spectra of freeze-drying of strawberries

Main features of the EPR spectra are given by the signal of organic free radicals in addition to traces of Mn^{2+} and Fe^{3+} with various signal intensities and degree of resolution for Mn^{2+} sextet lines (I=5/2) due to hyperfine interaction.

Thus, in the case of strawberries grown in the greenhouse, the signal characteristic of Fe^{3+} is very weak, which shows a small presence of iron in the paramagnetic state. This may be due to iron deficiency which is related with Fe uptake by plant and the level of available Fe concentration in soil and environmental conditions (high pH, low organic matter content, low soil temperature) [12,13]. In addition, manganese signal is well resolved sextet, reflecting the presence of partial unbounded Mn^{2+}. On the other hand, EPR spectrum of strawberries grown in natural conditions, presents some spectral features. First an intense signal of narrow band at g =4.3 indicating that there is isolated high spin Fe^{3+} (S=5/2) with a rhombic symmetry in the complexes and second, an increase of the line broadening of the Mn^{2+} signal, probably due to the fact that manganese ion is bound to other

nutritional macromolecules (Carbohydrates, Lipids, Proteins, and Nucleic Acids). It can be also noticed a difference between the signal intensities centered on g ≈ 2.0 due to the free radical (possibly semiquinones) overlapped with the signal of low-spin Fe^{3+} (S=1/2) and can be correlated with the antioxidant activity of the studied samples. Antioxidant activity was measured according to their ability to scavenge $ABTS^{+}$ in the reaction mixture.

The rate of reaction between antioxidant compounds (fresh juice) and $ABTS^{+}$ was monitorised by using normalized double integrated residual EPR signal which is correlated with number of paramagnetic species in time (Fig.2).

The best fit was obtained using the first order exponential decay:

$$I(t) = I_0 + I_1 e^{-kt}$$

were I_0, and I_1 are the fitation constants, and k is the kinetic constants of reaction corresponding to each type of extracts. The k constant is specific to each type of sample and processing way. It represents the oxido-reduction rate of the ABTS+ radical cation in time. The EPR spectra of studied samples show the interpretable differences between the analyzed samples.

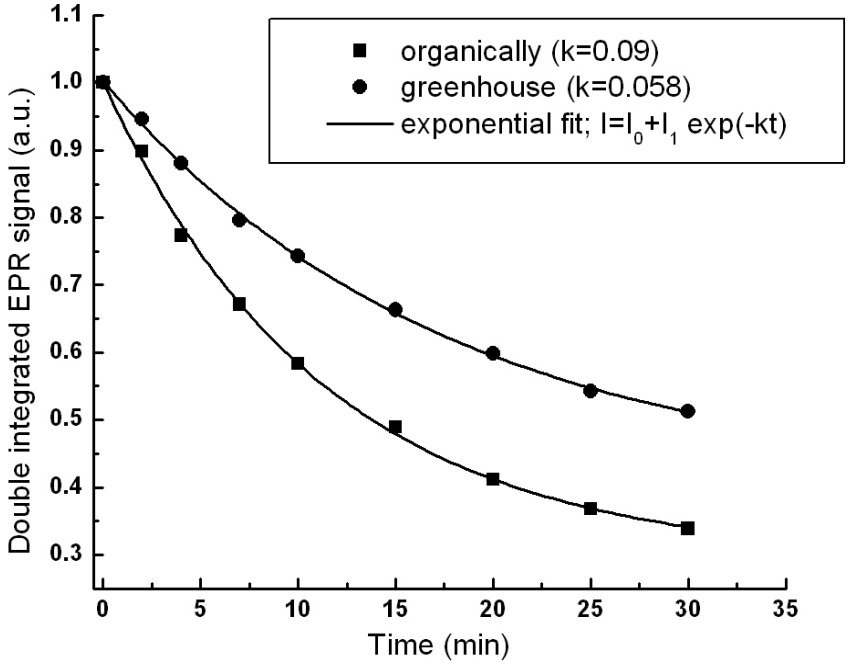

Figure 2. Antioxidant activity of fresh strawberries juices

The analysis of the antioxidant activity of extracts of strawberry shows that antioxidant capacity of strawberries grown naturally (organically) is significantly higher than those grown in the greenhouse.

CONCLUSIONS

In the present study, we tried applying the EPR spectroscopy to evaluate the possibility to characterize strawberry fruits grown in the greenhouse and in the natural conditions (organically). The result shows that ESR spectroscopy has been able to characterize changes in main paramagnetic components, i.e. iron, manganese and native semiquinone-like free radicals. The differences between the EPR spectra of the studied samples may be consequences of different types of biochemical processes involved in the metabolic process of growth. Detection and characterization of these paramagnetic species can be an important indicator (a spectroscopic fingerprint) in the detection of the fruits grown in the greenhouse and grown in natural conditions.

In addition, the study of the antioxidant activity of fresh strawberry juice showed that antioxidant capacity of strawberries grown naturally (organically) is significantly higher than those grown in the greenhouse.

REFERENCES

1. S.A. El Sohaimy, *World Applied Sciences Journal*, *20 (5)*, 691 (2012)
2. K.B. Pandey, S.I. Rizvi, *Oxid Med Cell Longev*, *2(5)*, 270 (2009)
3. www.sciencedaily.com/releases/2014/08/140827111944.htm, American Chemical Society "How to prevent organic food fraud"
4. A.A. Torun, N. Erdem, Y. AkaKaçar, S. Serçe, *Not Bot Horti Agrobo*, *41(2)*, 560 (2013)
5. D. Bourn, J. Prescott, *Crit. Rev. Food Sci. Nutr*. *42*, 1 (2002)
6. M. Hohmann, N. Christoph, H. Wachter, U. Holzgrabe, *J. Agric. Food Chem*., *62(33)*, 8530 (2014)
7. A. Tres, G. van der Veer, M.D. Perez-Marin, S.M. van Ruth, A. Garrido-Varo, *J Agric Food Chem. 60(33)*, 8129 (2012)
8. A. Basu, D.X Fu, M. Wilkinson, B. Simmons, M. Wu, N.M. Betts, M. Du, T.J. Lyons, *Nutr. Res., 30(7)*, 462 (2010)
9. H.D. Sesso, J.M. Gaziano, D.J. Jenkins, J.E. Buring, *J. Am. Coll. Nutr. 26*, 303 (2007)
10. D.E. Wedge, K.M. Meepagala, J.B. Magee, S.H. Smith, G. Huang, L.L. Larcom, *Journal of Medicinal Food*, *4(1)*, 49 (2001)
11. F. Giampieri, J.M. Alvarez-Suarez; M. Battino, *J. Agric. Food Chem*., *62(18)*, 3867 (2014)

12. W. M. Stewart, D. W. Dibb, A. E. Johnston, T. J. Smyth, *Agronomy Journal*, *97*, 1 (2005)
13. Y. Yi, M. L. Guerinot, *The Plant Journal*, *10(5)*, 835 (1996)
14. N.S. Vedeanu, D.A. Magdas, L. Bolojan, G. Damian, *Chemical Papers*, *66(6)*, 612 (2012)

STUDIA UBB PHYSICA, Vol. 61 (LXI), 1, 2016, pp. 27-34
(RECOMMENDED CITATION)

Dedicated to Professor Dr. Cozar Onuc on His 70th Anniversary

XPS INVESTIGATIONS OF $La_{0.67}Sr_{0.33}Co_{1-x}Mn_xO_3$ COMPOUNDS

R. DUDRIC[a,*], I.G. DEAC[a], M. NEUMANN[b] and R. TETEAN[a]

ABSTRACT. The electronic structure of the polycrystalline $La_{0.67}Sr_{0.33}Co_{1-x}Mn_xO_3$ perovskites with $0 \le x \le 0.5$ has been investigated by X-ray photoelectron spectroscopy (XPS). The valence band spectra shows several features, due to Mn 3d, Co 3d and extensively hybridized Mn3d-O2p and Co3d-O2p states, while the core level spectra show the presence of Co^{4+} and Co^{2+} states.

Keywords: *Manganites, Cobaltites, X-ray photoelectron spectra*

INTRODUCTION

The discovery of the colossal magnetoresistance (CMR) effect in the manganites $R_{1-x}A_xMnO_3$ (where R is lanthanum or a rare earth ion and A is a divalent alkali) [1] stimulated the interest to the new perovskite-type materials such as the cobaltites with a similar formula $R_{1-x}A_xCoO_3$ [2,3]. These latter compounds have technical application potential due to their high electrical and ionic conductivities, their use in ferroelectric thin film capacitors [4], in solid oxide fuel cells [5], as oxygen permeable membranes [6], as possible applications as magnetostrictive actuators [7], in thermoelectric elements [8] and as active catalysts [9]. The occurrence of CMR effect and of ferromagnetism in manganites had been attributed to the double-exchange (DE) interaction between Mn^{3+} and Mn^{4+} ions intermediated by $2p^6$ O ions [1]. In the mentioned cobaltites, the origin of ferromagnetism seems to be different. $LaCoO_3$ is a nonmagnetic insulator at low temperature and $SrCoO_3$ is a long range ferromagnet [2]. Substitution of Sr^{2+} for La^{3+} in $LaCoO_3$ gives rise to a partial oxidation of Co^{3+} to Co^{4+} ($3d^6$) as in the similar formula manganites. This doping makes the material to segregate into hole-rich metallic ferromagnetic clusters and a hole-poor matrix similar to $LaCoO_3$ [10].

[a] *Faculty of Physics, Kogalniceanu 1, 400084 Cluj-Napoca, Babes-Bolyai University, Romania*
[b] *Universität Osnabrück, Fachbereich Physik, D-4500 Osnabrück, Germany*
[*] *Corresponding author: roxana.pacurariu@phys.ubbcluj.ro*

A ferromagnetic order can occur, with a Curie temperature lower than 280 K, and the ferromagnetism is assumed to be of an itinerant electron type. [11]. For low Sr content ($0.05 \leq x \leq 0.2$) $La_{1-x}Sr_xCoO_3$ has spin-glass-like behaviour [12]. The striking feature of cobaltites, deciding their magnetic properties as compared to the CMR manganites, is the presence of the various spin states for Co^{3+} and Co^{4+} ions, i.e. they can be present in low-, intermediate- or high-spin state [2,3,10]. This fact is possible as a result of the competition between the comparable magnitudes of crystal field and intraatomic Hund energy, which dictates the occupation of the t_{2g} and e_g electron energy levels. The doped perovskites, $La_{1-x}Sr_xMnO_3$ [1,13] and $La_{1-x}Sr_xCoO_3$ [2,10-12] were extensively studied for the richness of their physical properties. For $x = 0.33$, the both systems exhibit long range ferromagnetic order. In the solid solution $La_{0.67}Sr_{0.33}Co_{1-x}Mn_xO_3$, a multitude of interactions between the magnetic ions, mediated by the oxygen ions is expected: Mn^{3+}–O–Mn^{4+}, Mn^{3+}–O–Mn^{3+}, Mn^{4+}–O–Co^{2+} and Mn^{4+}–O–Mn^{4+}, Co^{2+}–O–Co^{2+}, Co^{2+}–O–Mn^{3+} [14,15-17]. The chemical disorder as well as the magnetic ions disorder can cause major changes in the magnetoelectronic properties of these compounds.

Previously, we systematically studied the structural, electrical and magnetic properties of the compounds $La_{0.67}Sr_{0.33}Co_{1-x}Mn_xO_3$ with $0.5 \leq x \leq 1$ [15-17]. The samples, prepared by conventional ceramic method, were pseudo-cubic perovskites with slight rhombohedral distortions. The magnetic measurement indicated that the long range ferromagnetism from the optimal doped manganite $La_{0.33}Sr_{0.67}MnO_3$ is destroyed when more than half of the Mn ions are replaced by Co ions and a cluster glass magnetic state occurred (i.e. ferromagnetic clusters embedded in a non ferromagnetic matrix). This state was suggested by *M(H)* measurements and also by the frequency dependence of the ac susceptibility $\chi_{ac}(T)$ in the region of the freezing temperature T_f, described by a Vogel–Fulcher law that presumes correlations between spin clusters [15]. The samples showed low electrical resistivity with $\rho(T)$ curves indicating semiconductor behavior and rather high negative magnetoresistance, up to 18 % for x= 1. The resistivity is lower with increasing Co^{3+} ions content and its behavior in the high temperature range was attributed to a hoping mechanism in the presence of a charge disproportionation effect of Co^{3+} ions in Co^{2+} and Co^{4+} [18]. Besides these properties, $La_{0.67}Sr_{0.33}Co_{1-x}Mn_xO_3$ compounds were found [17] to show moderate magnetocaloric effect, comparable to that obtained in other perovskite-type compounds operating in the intermediate temperature range.

The present work is an extension of our previous studies [15-17] on the electrical and magnetic behavior of the system $La_{0.67}Sr_{0.33}Co_{1-x}Mn_xO_3$, to complete our data and to probe our assumptions with the information about the electronic structure of our samples. XPS technique [19] was used to investigate the chemical states of manganese and cobalt ions and the changes in the band structure in these compounds.

EXPERIMENTAL

The $La_{0.67}Sr_{0.33}Co_{1-x}Mn_xO_3$ samples were the same we used in our previous works [15-17], where the details of sample preparation and characterization measurements can be found. The samples were characterized by using magnetization, electrical transport and x-ray diffraction measurements.

The XPS measurements were performed by using an an ESCA (PHI 5600ci) spectrometer equiped with monochromatized Al Kα radiation with hν = 1486.6 eV. The measurements were performed under a base vacuum maintained below 10^{-9} mbar. In order to have samples with fresh surfaces the samples were cleaved in situ. The spectra were recorded at room temperature and calibrated against the Au $4f_{7/2}$ signal from an Au foil (80.0 eV).

RESULTS AND DISCUSSION

The XPS valence band spectra of $La_{0.67}Sr_{0.33}Co_{1-x}Mn_xO_3$ perovskites show several features below 12 eV, as presented in Fig. 1a. The structure below 2 eV has a large Co 3d contribution at about 1 eV and hence decreases in intensity with the decrease of Co content [20]. In the spectral region between 2 eV and 5 eV there are several contributions from the Mn 3d (t_{2g}), Co 3d and of extensively hybridized Mn3d-O2p and Co3d-O2p states [21-23]. The third feature situated above 5 eV is associated with the O 2p bands.

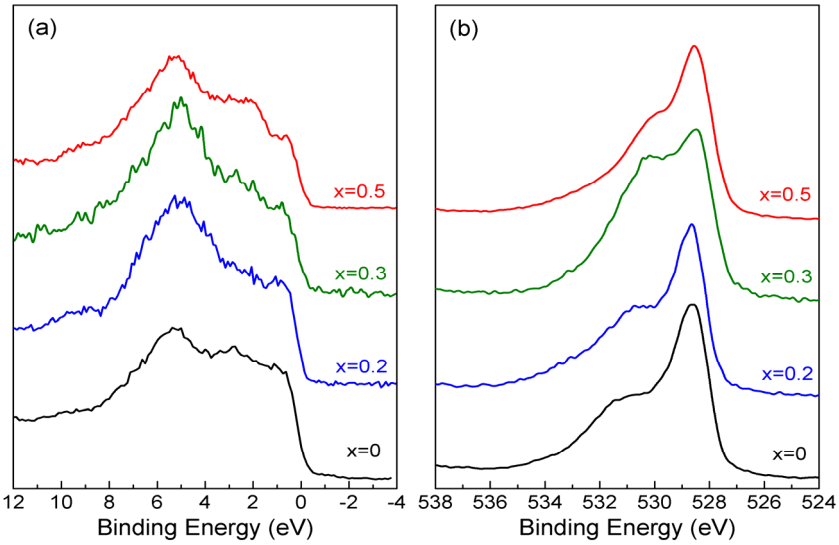

Fig. 1. a) XPS valence band spectra and b) XPS O 1s core level of $La_{0.67}Sr_{0.33}Co_{1-x}Mn_xO_3$ perovskites

The O 1s core level spectra shown in Fig. 1b present two distinct features for all the samples. The lower binding energy peak is generally assigned to the lattice oxygen (oxygen-metal bonds), while the higher binding energy peak is assigned to less electron-rich oxygen species and can be attributed to extrinsic effects such as defects in crystal lattice and surface contamination (adsorbed oxygen, hydroxyl, and carbonate species). For sintered samples, the relative contribution of this peak depends on the fabrication conditions and surface preparation.

The XPS spectra of the La 3d and La 4d levels, shown in Fig. 2, are very similar for all the samples. The La 3d photoelectron signal exhibits a spin orbit splitting of about 16.8 eV, typical for La^{3+} compounds. An additional split due to the transfer of an electron from the oxygen valence band to the empty La 4f level [24] leads to the double peak structures of nearly identical intensity of both the $3d_{3/2}$ and $3d_{5/2}$ levels. The separation between the main peak and the satellite peak does not change with the variation of Mn/Co content (~4 eV), suggesting that the interaction between the La ions and the transition-metal ions is very weak [24].

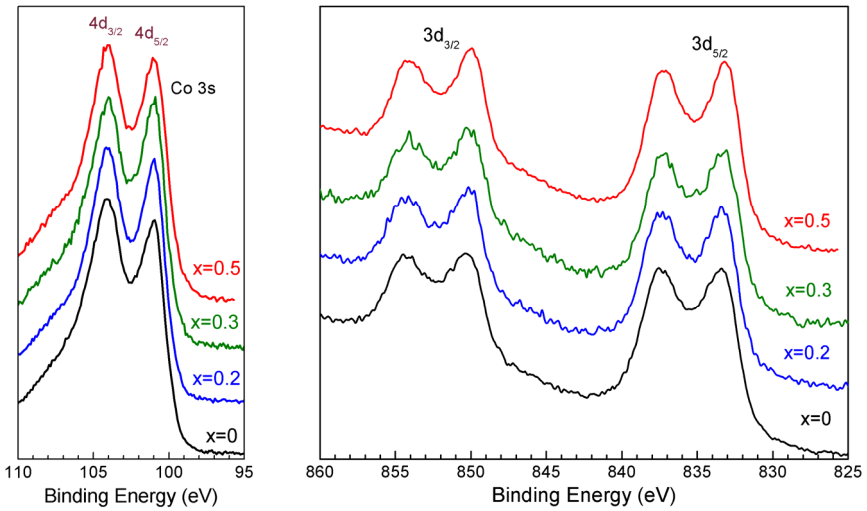

Fig. 2. XPS La 4d (left) and La 4d (right) core level spectra of $La_{0.67}Sr_{0.33}Co_{1-x}Mn_xO_3$ perovskites

The Mn 2p and Co 2p XPS spectra, shown in Fig. 3, provide valuable information about the transition metal ions valence state. There is no significant shift between the Mn 2p core level spectra of the investigated samples, which indicates that the Mn^{3+}/Mn^{4+} ratio does not change with the increase of Mn concentration. All spectra show a spin orbit splitting between the Mn $2p_{3/2}$ and Mn $2p_{1/2}$ levels of about 11.6 eV.

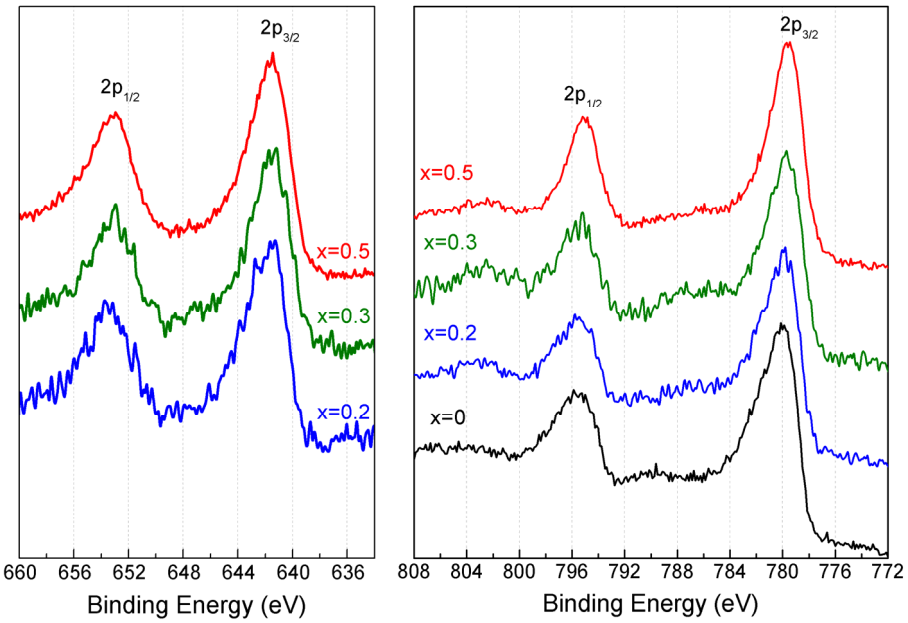

Fig. 3. XPS Mn 2p (left) and Co 2p (right) core level spectra of $La_{0.67}Sr_{0.33}Co_{1-x}Mn_xO_3$ perovskites

The Co 2p XPS spectra of all investigated samples present two main peaks situated at about 780 eV ($2p_{3/2}$) and 795.5 eV ($2p_{1/2}$) which indicates that Co is predominantly present as Co^{3+} state. The presence of a shoulder on the high energy side of the Co $2p_{3/2}$ and Co $2p_{1/2}$ components imply the presence of Co^{4+} states, with binding energies around 781.4 eV and 796.7 eV. The satellite features situated at 785-788 eV and 802-804 eV confirm also the presence of Co^{2+} ions in the samples with x>0 [25,26]. The satellite intensity in Co compounds is related to the spin states and increases with the increase of unpaired atomic electrons [27]. With the increase of Mn content one can notice a slight shift of the two main peaks towards lower binding energies, as well as a changes in widths and asymmetries. Fig. 4a shows the XPS spectra of Co $2p_{3/2}$ core level after background removal, using a Shirley-type background shape [28]. By analyzing the binding energy and full width at half maximum (FWHM) of the Co $2p_{3/2}$ core level we found that both decrease with the increase of Mn content, as presented in Fig. 4b and Fig. 4c, respectively.

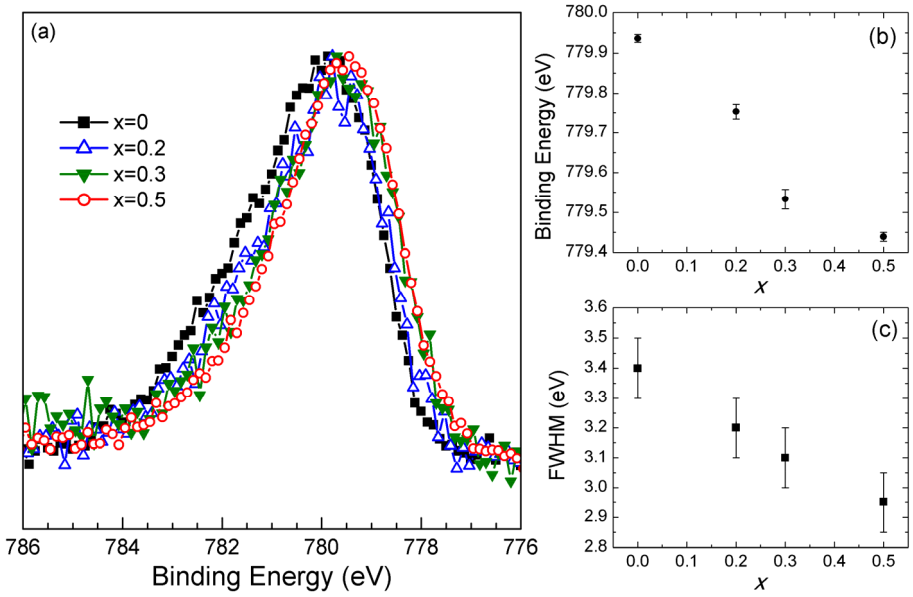

Fig. 4. (a) XPS spectra, (b) binding energies and (c) full width half maximum (FWHM) of Co $2p_{3/2}$ core level for $La_{0.67}Sr_{0.33}Co_{1-x}Mn_xO_3$ perovskites

CONCLUSIONS

The electronic structures of the $La_{0.67}Sr_{0.33}Co_{1-x}Mn_xO_3$ compounds were investigated by using the XPS technique. The XPS valence band spectra show several features below 12 eV, with several contributions from the Mn 3d, Co 3d and of extensively hybridized Mn3d-O2p and Co3d-O2p states in the spectral region between 2 eV and 5 eV. By analyzing the Mn 2p core level spectra we can conclude that the Mn^{3+}/Mn^{4+} ratio does not change with the increase of Mn concentration. The XPS Co 2p spectra confirm the presence of Co^{4+} and Co^{2+} states.

ACKNOWLEDGEMENTS

This work was supported by the grant IDEI code PN-II-ID-PCE-2011-3-0583 of CNCS, Romania.

REFERENCES

[1] For reviews see A.P. Ramirez, *J. Phys.: Condens. Matter* 9 (1997) 81; J. M. D. Coey, M. Viret, and S. von Molnar, *Adv. Phys.* 48 (1999) 167.

[2] R. Ganguly, A. Maignan, C. Martin, M. Hervieu, and B. Raveau*, J. Phys.: Condens. Matter* 14 (2002) 8595; K. Yoshii and H. Abe, *Phys. Rev. B* 67 (2003) 094408;

[3] R. Caciuffo, D. Rinaldi, G. Barucca, J. Mira, J. Rivas, M.A. Senaris-Rodriguez, P.G. Radaelli, D. Fiorani, and J.B. Goodenough, *Phys. Rev. B* 59 (1999) 1068.

[4] S. Sadashivan, S. Aggarwal, T.K. Song, R. Ramesh, J.T. Evans, Jr., B.A. Tuttle, W.L. Warren, and D. Dimos, *J. Appl. Phys.* 83 (1998) 2165.

[5] H. Uchida, S. Arisaka, and M. Watanabe, *J. Electrochem. Soc*. 149 (2002) A13.

[6] X. Qi. Y.S. Li, L. S. Swartz, *Ind. Eng. Chem. Res*. 39 (3) (2000) pp 646–653.

[7] M.R. Ibarra, R. Mahendiran, C. Marquina, B. Garcia-Landa, and J. Blasco, *Phys. Rev. B* 57 (1998) R3217.

[8] S. Hébert, S. Lambert, D. Pelloquin, and A. Maignan, *Phys. Rev. B* 64 (2001) 172101.

[9] J.L. Hueso, A. Caballero, M. Ocaña, A.R. González-Elipe*, J. Catal*. 257 (2008) 334–344.

[10] M. Senaris-Rodriguez and J.B. Goodenough, *J. Solid State Chem*. 118, (1995) 323 and references therein.

[11] P. Raccah and J.B. Goodenough, *Phys. Rev.* 155, (1967) 932–943; P. Ravindran, H. Fjellvåg, A. Kjekshus, P. Blaha, K. Schwarz, and J. Luitz*, J. Appl.Phys.* 91(2002) 291-303.

[12] J. Wu and C. Leighton, *Phys. Rev.* 67 (2003) 174408.

[13] P. Schiffer, A.P. Ramirez, W. Bao, and S-W. Cheong, PRL75 (1995) 3336-3339.

[14] I.O. Troyanchuk, L.S. Lobanovski, D. D. Khalyavin, N.S. Pastushonok, H. Szymczak, *J. Magn. Magn. Mater.* 210, 63 (2000); H. Gamari-Seale, I.O. Troyanchuk, A.P. Sazonov, K.L. Stefanopoulos, D.M. Toebbens, *Physica B* 403 (2008) 2924–2929.

[15] I.G. Deac, R. Tetean and E. Burzo, *Physica B* 403 (2008) 1622–1624.

[16] I.G. Deac, R. Tetean and E. Burzo, *J Optoelectron. Adv. M.* 9 (2007) 1108-1112.

[17] R. Tetean, I.G. Deac, E. Burzo and A. Bezergheanu, *J. Magn. Magn. Mater.* 320 (2008) e179–e182.

[18] C. Autret, J. Hejtmanek, K. Knizek, M. Marysko, Z. Jirak, M. Dlouha and S. Vratislav, *J. Phys.: Condens. Matter* 17, 160 (2005), and references therein.

[19] M. Neumann, K. Kuepper, *Surf. Sci.* 603 (2009) 1613–1621.

[20] T. Saitoh, A.E. Bocquet, T. Mizokawa, H. Namatame, A. Fujimori, M. Abbate, Y. Takeda, M. Takano, *Phys. Rev. B* 51 (1995) 13942.

[21] J.-H. Park, S-W. Cheong and C.T. Chen, *Phys Rev B* 55 (1997) 11072.

[22] S.K. Pandey, Ashwani Kumar, S. Patil, V.R.R. Medicherla, R.S. Singh, K. Maiti, D. Prabhakaran, A.T. Boothroyd, and A.V. Pimpale, *Phys Rev B* 77 (2008) 045123.

[23] D.N. McIlroy, C. Waldfried, Jiandi Zhang, J.-W. Choi, F. Foong, S.H. Liou, and P.A. Dowben, *Phys Rev B* 54 (1996) 17438.

[24] D.J. Lam, D.W. Veal, D.E. Ellis, *Phys. Rev. B* 22 (1980) 5730

[25] M.C. Falub, V. Tsurkan, M. Neumann, I.O. Troyanchuk, V.R. Galakhov, E.Z. Kurmaev, H.H. Weitering, *Surf. Science* 532 (2003) 488.

[26] M. Oku, Y. Sato, *Appl. Surf. Sci.* 55 (1992) 37.
[27] Yu.G. Borod'ko, S.I. Vetchinkin, S.L. Zimont, I.N. Ivleva, Yu.M. Shul'ga, *Chem Phys Lett* 42 (1976) 264.
[28] D.A. Shirley, *Phys. Rev. B* 5 (1972) 4709.

STUDIA UBB PHYSICA, Vol. 61 (LXI), 1, 2016, pp. 35-46
(RECOMMENDED CITATION)

Dedicated to Professor Dr. Cozar Onuc on His 70th Anniversary

FINITE ELEMENT ANALYSIS OF FRICTION PARAMETERS ON 6060 ALUMINIUM ALLOY IMPRESSION DIE COLD FORGING PROCESS

M. POP[a,*], D. FRUNZA[a]

ABSTRACT. In this paper cold forging process of aluminium alloy 6060 is simulated and analyzed at different stages of forging and with different quality of lubricants. Finite element (FE) method is extensively employed in solving linear and non-linear problems and widely used particularly in analyzing a forming process. Three-dimensional modeling of initial material and die are performed by Solid Works, while simulation and analysis of forging are performed by Forge. Based on the computer simulation the required dies are designed and the workpieces are formed.

Keywords**:** *Aluminium alloy, Impression die forging, FE analysis, Simulation.*

INTRODUCTION

One of the major concerns in the research of manufacturing processes is to find the optimal production conditions in order to reduce production costs and lead time. In order to optimize a process, the effect of the most important process parameters has to be investigated. Conducting experiments, can be very time consuming and expensive. Therefore, various computational methods have been developed and used to reduce the number of necessary experiments. One of these methods, FEM, has proved to be the most powerful analysis tool. With the increasing use of computers in industry, FEM has steadily gained importance in the simulation of metal-forming processes.

Cold forging is an essential process and widely used in a typical manufacturing production. In the process, the metal is continuously pressed under high pressure into high strength parts and as a result, the material experienced extensive plastic deformation during the progression.

[a] *Technical University, Faculty of Materials Engineering and Environment, B-dul Muncii 103-105, Cluj-Napoca, Romania*
[*] *Corresponding author: Mariana.Pop@ipm.utcluj.ro*

Besides, cold forging has a high performance on the production rate and repeatability. The parts with cold forging process are largely produced at high rate compare to those achieved by the machining processes as the parts are immediately ready for use after the forging; the process is conducted by automated production lines that directly converts the workpiece to the finished parts. The repeatability of the process becomes excellent with optimal die design, low temperature and optimal lubrication [1,7,8]. Another important advantage of cold forging process is the amount of waste material for finished part is very insignificant. The process is a "chipless machining", in which sometimes requires less or no cutting process as well as eliminates secondary grinding.

The prediction of material flow can be achieved completely by computer simulation. Main parameters in computer simulation are filling the die completely without leaving any defect, reducing material loss and stress in die and increasing die life.

Finite element analysis (FEA) has been developed during the last decades as a very useful tool for analysis of metal forming processes [2,3,4,9]. Recent progress in FEA, together with increasingly powerful computers, has permitted increased use of such numerical modeling. Hence, today it is possible to FEM-simulate the metal forming processes at various design stages.

Process modeling of closed-die forging using finite-element modeling (FEM) has been applied in aerospace forging for a couple of decades [2].

Aluminum alloy A6060 is one of the most used high-strength material for aircraft structural components. Also is commonly used for architectural sections for windows, doors, curtain walls, interior fittings, lighting, furniture and office equipment, structural applications where surface finish is important.

Friction has an important influence in metalforming operations, as it contributes to the success or otherwise of the process. In the present investigation, the effect of friction on metal forming was studied by simulating close die forging on AA6060 aluminium alloy using the finite element method (FEM) technique. However, the coefficient of friction between the die–work-piece interfaces was varied. It was concluded that the variations in the coefficient of friction between the dies and the work-piece directly affect the strain, stress distribution and deformation force.

The present study used rigid-plastic finite element (FE) Forge software to investigate the plastic deformation behavior of an aluminum alloy (A6060) workpiece.

THEORETICAL ASPECTS

Figure 1 present the impression die forging principle.

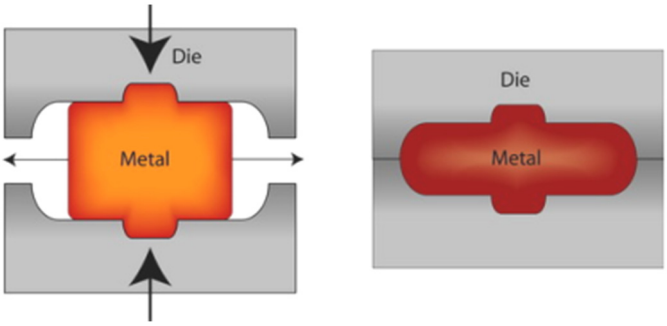

Fig. 1. Impression die forging principle.

During the forging process, metal flow, die fill, and forging load are largely determined by the flow stress of the forging materials, the friction and cooling effect at the die/material interface, and the complexity of the forging shape.

The interrelationships of the most significant forging variables are illustrated in the block diagram in Fig. 2.

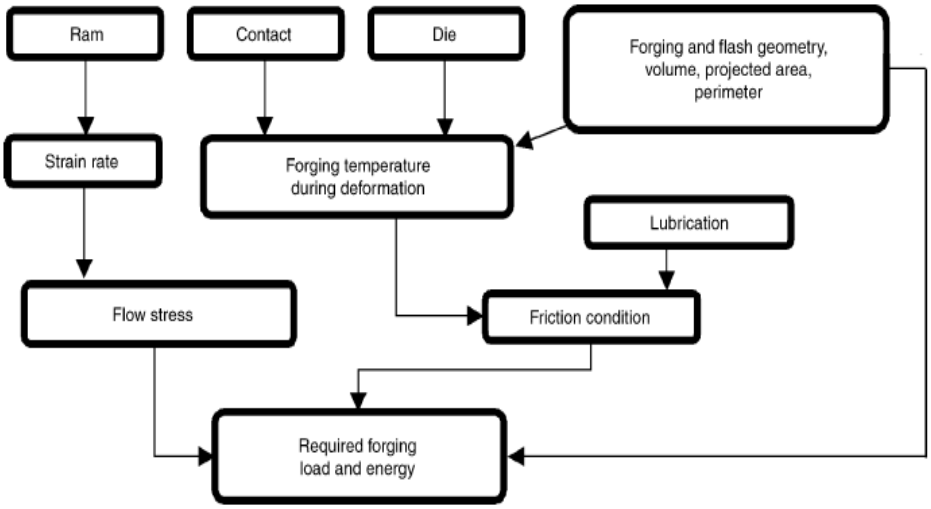

Fig. 2. Interaction of significant variables in impression die forging process [2].

In metal forming, friction is a crucial factor that determines whether an industrial process can be run with acceptable, economic result.

The basic function of any lubricant is to reduce friction between two surfaces and to reduce wear. In the case of forging, a good forging die lubricant must have the following properties: reduce friction, reduce forging load, enable uniform metal flow to fill the die cavity, serve as a barrier to heat transfer.

In impression die forging the metal is confined in between two dies. Under these circumstances, the contact pressure rise much higher than the flow stress of the workpiece material. Under high contact pressure, the Coulomb friction model may fail to describe the actual friction conditions. A friction model different from the Coulomb model is the Tresca friction model. This model is able to give a better description of the friction over the workpiece–die interface in the case of high contact pressures. These friction models have been developed for quantitative evaluation of friction in bulk metal forming, and are applied in FE analysis [10]. Coulomb friction model based on Amonton's law can be expressed as:

$$\boldsymbol{\tau = \mu\sigma} \tag{1}$$

where τ is the frictional shear stress, m the coefficient of friction at the die/workpiece interface, σ the normal stress.

Tresca's friction model is commonly expressed the following way:

$$\boldsymbol{\tau = mk = \frac{m}{\sqrt{3}}\sigma_c} \tag{2}$$

where m is the frictional shear factor, K the shear yield strength, if m=1, then $\tau = \tau_{max} = K$ for the condition of maximum friction force, namely sticking friction, whereas m=0 for a frictionless condition, σ_0 is shear flow stress of the workpiece material.

SIMULATION DETAILS

The tensorial form of the Norton-Hoff law used in FORGE 3® is written as [9]:

$$s = 2A(T, \bar{\varepsilon}, ...)(\sqrt{3} * \bar{\varepsilon})^{m-1} \dot{\varepsilon} \tag{3}$$

$$A(T, \bar{\varepsilon}) = A_0 * (\bar{\varepsilon} + \bar{\varepsilon}_0)^n * e^{\frac{\beta}{T}} \tag{4}$$

where ***s*** is the deviatoric stress tensor, A is the consistency of material, $\bar{\varepsilon}$ is the equivalent strain, m is the strain rate sensitivity, $\dot{\varepsilon}$ is the equivalent strain rate, β is the material constant, n is the strain hardening index and $\bar{\varepsilon}_0$ is a small constant.

The flow formulation introduced by Hensel and Spittel is written as:

$$\sigma = A * e^{m_1 T} * T^{m9} * \varepsilon^{m2} * e^{m4/\varepsilon} * (1+\varepsilon)^{m5T} * e^{m7\varepsilon} * \dot{\varepsilon}^{m3} * \dot{\varepsilon}^{m8T} \tag{5}$$

where m_1, m_2,..m_9 are sensitivity parameters.

A simulation of the close die forging process was performed using the finite element software. This was achieved by constructing an accurate three dimensional CAD model of the process. The model was meshed with appropriate elements and material properties and boundary conditions were added. The geometries of the billet and dies, were generated in SolidWorks and the meshes within their space domains in FORGE 3D. The physical properties of the aluminium alloy used in the computer simulation are given in Table 1. The billet was considered thermo-viscoplastic while the tools rigid, and both of these material models neglected the elastic deformation. The shear-type friction conditions at the workpiece and tooling interfaces were imposed as part of the boundary conditions.

Table 1.

Properties	Material A6060
Density (kg/m^3)	2800
Heat capacity (N/m$^{2\,0}$C)	2,39
Thermal conductivity (W/mK)	250
Emissivity	0,05

The process parameters used in the simulations are given in Table 2.

Table 2.

Billet height [mm]	15
Billet diameter [mm]	40
Upper die speed [mm/s]	0,5
Friction factor at the workpiece–die interface	0,1;0,3;0,4
Billet temperature [^{0}C]	20
Dies temperature [^{0}C]	20

The geometries of the billet, die, container and ram were generated in SolidWorks and the meshes within their space domains in FORGE 3D. Fig. 3 shows the initial meshes of the billet and the tooling, together with a cross-section cutting through the die. The die had a rotational symmetry, which allowed one-quarter of objects to be modelled in order to save computing time. The present analysis adopts the following assumptions: (1) the mold and die are all rigid bodies; (2) the aluminum alloy (A6060) billet is a rigid-plastic material. The parameters from the constitutive equation are presented below.

```
Thermoecroui: Hansel Spittel Nb1,
! Material name: AA  6060
! Material type: Al-alloys
! Material subtype: Al-Mg-Si
! Properties type: cold forming
! Units: MPa,degC
! Validity domain:
! Temperature: 20 - 250
! Strain: 0.04 - 3
! Strain rate: 0 - 500
A1=201.29204,
m1=-0.00156,
m2=0.00000015737,
m3=0.01648,
m4=0.00116,
m5=0,
m6=0,
m7=0,
m8=0,
m9=0,
eps_ss = 0.
```

Fig. 3 shows the initial mesh of the billet and the geometrical model of the dies.

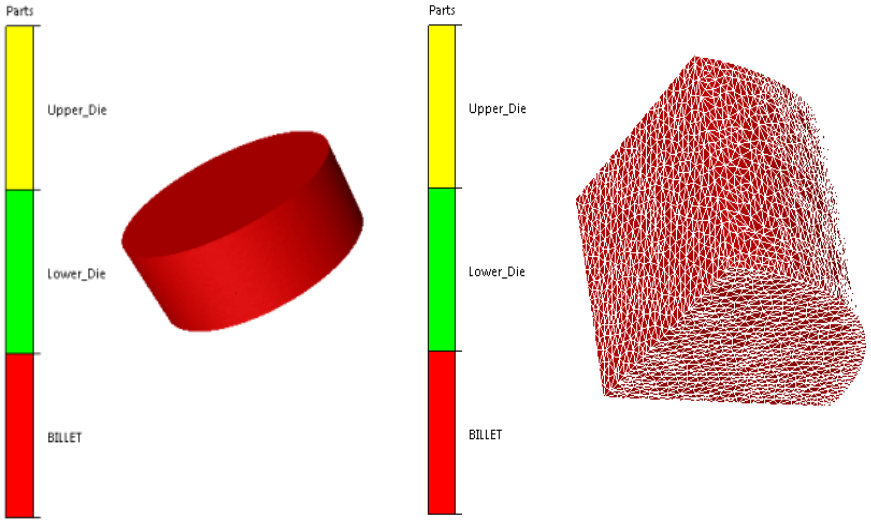

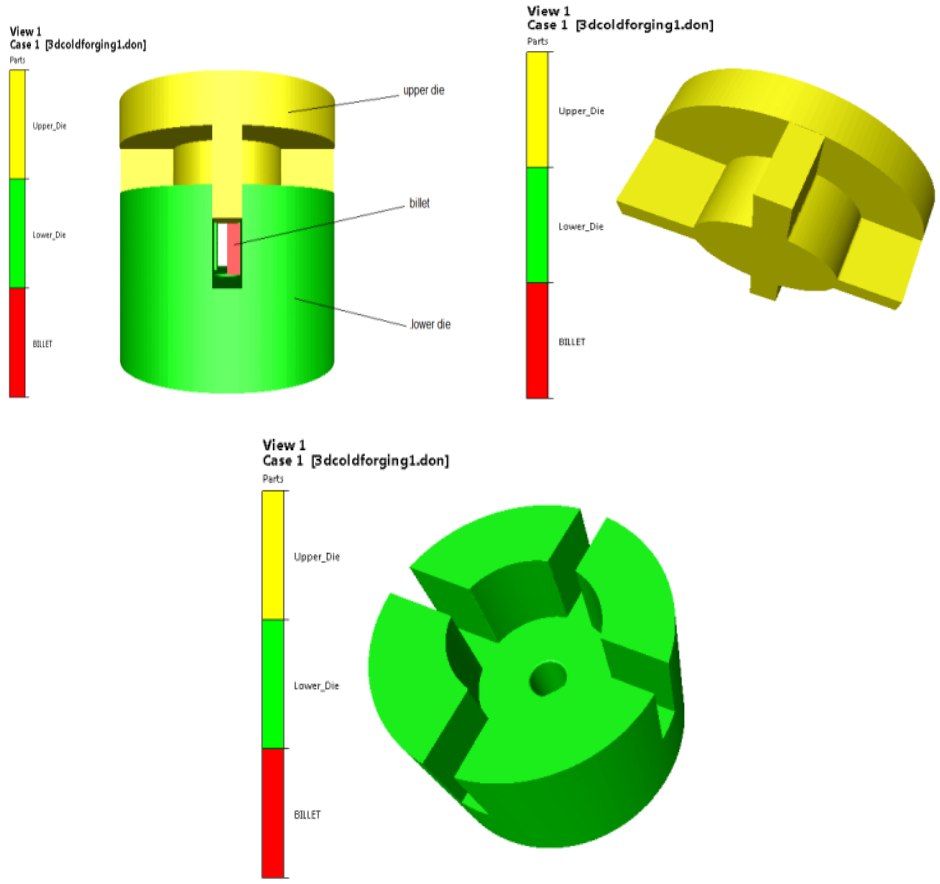

Fig. 3. Initial mesh of the billet, and the geometrical models of the dies.

RESULTS AND DISCUSSIONS

After the model has been created, a number of simulations were run to study the effect of lubrication conditions on the metal flow. The results obtained for equivalent strains, von Mises stress, energy exchange due to friction and deformation force distribution in different lubrication conditions are presented in figures below.

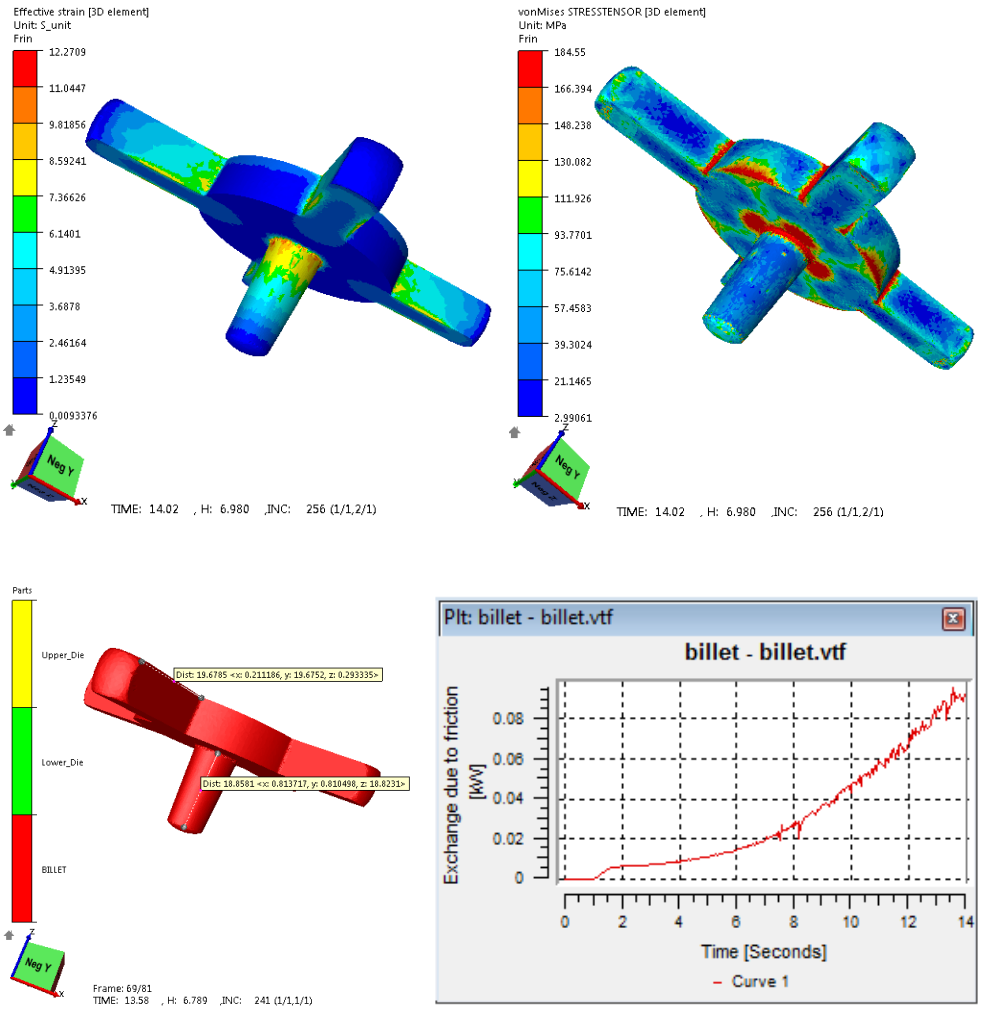

Fig. 4. Distribution of effective strain, von Mises stress and exchange energy due to friction in the billet for friction coefficient μ=0,4.

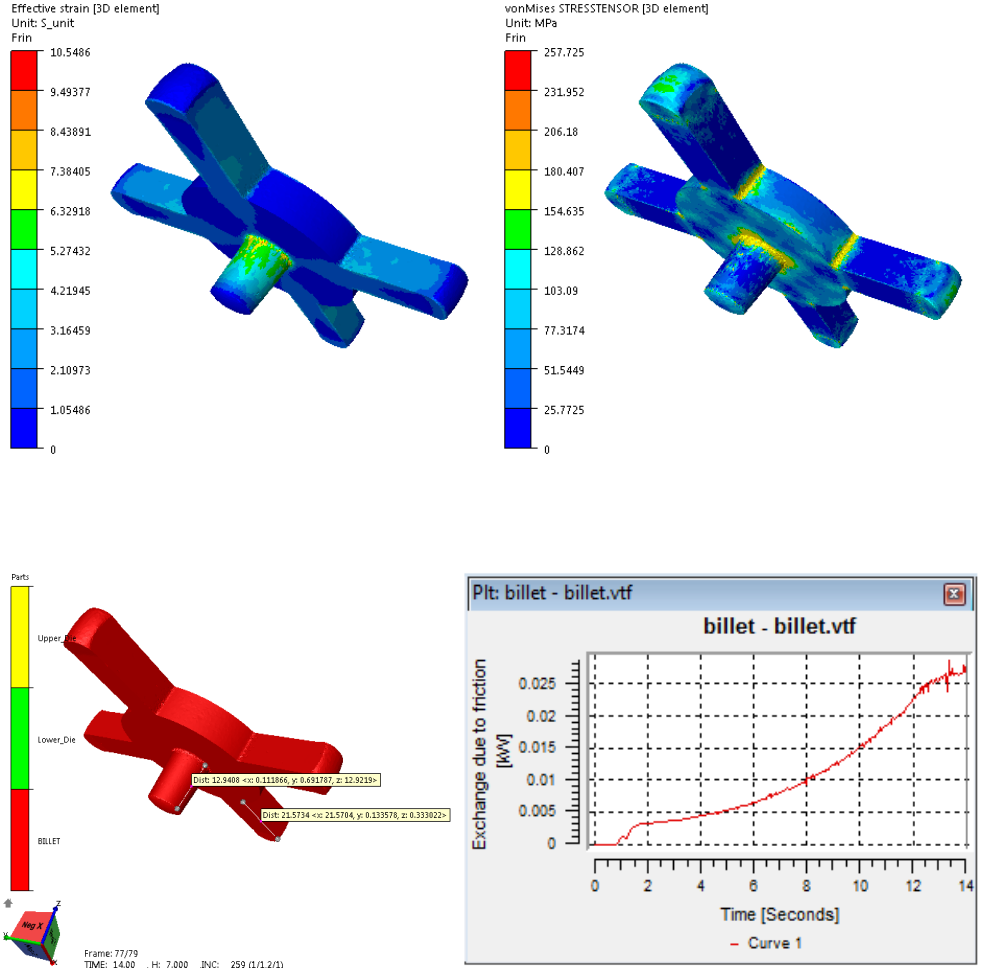

Fig. 5. Distribution of effective strain, von Mises stress and exchange energy due to friction in the billet for friction coefficient μ=0,1.

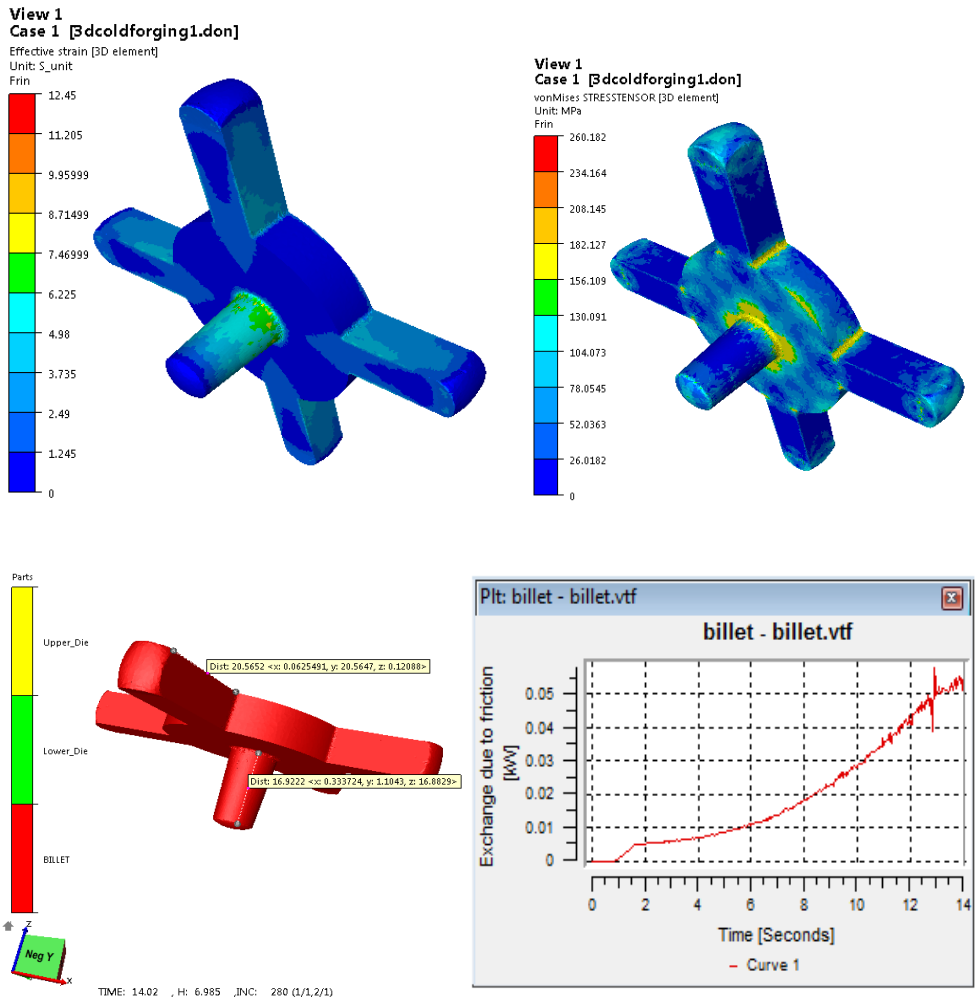

Fig. 6. Distribution of effective strain, von Mises stress and exchange energy due to friction in the billet for friction coefficient μ=0,2.

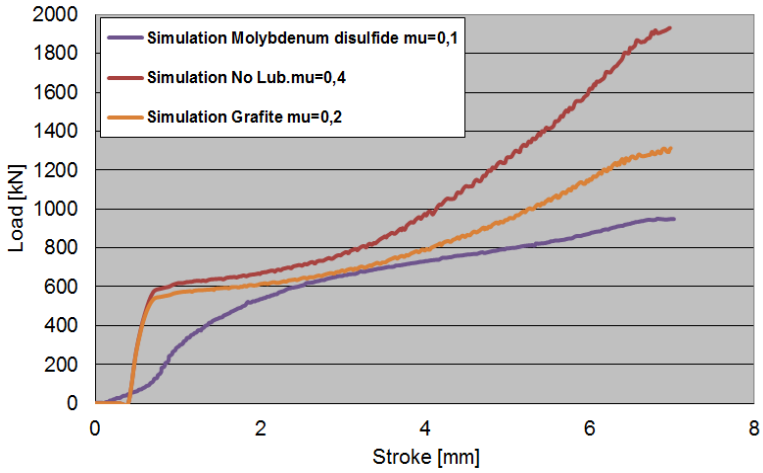

Fig. 7. Deformation force distribution.

By referring to Fig.7; it indicates that the total forming load was increased with the values of friction coefficient. The highest maximum forming load was produced when no lubrication is used, which has the highest friction coefficient value. On the other hand, the lowest maximum forming load was generated as molybdenum disulfide was applied. It was found that the forming load values exhibited by no lubrication, graphite, and molybdenum disulfide were 1900kN, 1300 kN and 950 kN, respectively. It has been evaluated from the FE results that the forming load was found to be proportional to the friction coefficients, as the friction values increased, the die life decreased as higher friction coefficients required higher load to fill the die cavity. Based on the analyses, the friction utilized in the die design to a great extent influenced the metal flow as it can be seen in figures 4,5 and 6. By increasing the coefficient of friction from 0,1 to 0,4 increases also the effective strain and von Mises stress. The increase in von Mises stress value determine an increase in die wear and the fatigue life would be reduced. From the analysis, the highest maximum stress in the billet was found as 185 MPa with friction coefficient of 0.4, whilst the lowest value of maximum stress was 154 MPa with friction coefficient value of 0.1.

In summary, the optimal value of friction coefficient in impression die cold forging of A6060 aluminium alloy was 0.1, in which the lubricant consisted of molybdenum disulfide.

CONCLUSIONS

Computer-aided engineering (CAE) simulation is a useful tool to optimize, validate, verify and hence, generate the design solutions before they are implemented. The results can be utilized to analyze the tool design and forming processes during

the designing stage as well as in the trouble shooting stage. In the current study, the effect of friction coefficients were studied on the material flow in impression die cold forging. Workpiece and die assembly components were constructed in the CAD models before the commercial FEM-code ForgeTM was implemented.

It has been evaluated from the FE results that the forming load was found to be proportional to the friction coefficients, as the friction values increased, the die life decreased as higher friction coefficients required higher load to fill the die cavity.

REFERENCES

1. Ab-Kadir A.R., Othman A.R., Samad Z, Khaleed Hussain. M. T., Abdullah A.B., Effect of Corner Radius and Friction Parameters on the Optimization of the Cold Forging Die Design, *Modern Applied Science,* vol.3, no.2, pp. 177-189 (2009).
2. Altan T., Ngaile G., Shen G., Cold and Hot Forging, Fundamentals and Applications, *ASM International* (2005).
3. Chenot J.L., Massoni E., „Finite element modelling and control of new metal forming processes", in *International J. Machine Tools & Manufacture*, vol. 46, no. 11 (2006), pp.1194–1200.
4. Hartley P., Pillinger I., „Numerical simulation of the forging process", in *Comput. Methods Appl. Mech. Eng*. vol. 195, pp. 6676–6690 (2006).
5. Jun, B. Y., Kang, S. M. Lee, M. C. Park, R. H. and Joun, M. S., 'Prediction of geometric dimensions for cold forgings using the finite element method', *J. Mater. Process. Technol*. 189, 459-463 (2007).
6. Marie S., Ducloux R., Lasne P., Barlier J. and Fourment L., Inverse Analysis of Forming Processes based on FORGE environment, *Key Engineering Materials* Vols. 611-612, pp 1494-1502 (2014).
7. Mohammadi M., Sadeghi M., Numerical and experimental investigation of forging process of a CV joint outer race, *International Journal of Research and Reviews in Applied Sciences* Volume 2, Issue 1 (2010).
8. Ngaile, G., Saiki, H., Ruan, L. and Marumo, Y., 'A tribo-testing method for high performance cold forging lubrications'; *WEAR*, 262, 684-692 (2007).
9. Pop M., Frunza D., Finite element analysis of superalloys forward extrusion, *Journal of Optoelectronics and Advanced Materials*, vol.17, no.7-8 (2015).
10. Valberg H.S., Applied Metal Forming Including FEM Analysis, Cambridge University Press, 2010.
11. Zhang Y., Huang J., Lin X., Fanga Q., Numerical simulation analysis on cold closed-die forging of differential satellite gear in car, *Materials Science Forum* Vols. 575-578, pp 517-524 (2008).

STUDIA UBB PHYSICA, Vol. 61 (LXI), 1, 2016, pp. 47-51
(RECOMMENDED CITATION)

Dedicated to Professor Dr. Cozar Onuc on His 70th Anniversary

STRUCTURAL CHANGES INDUCED BY ACTINIDES INCORPORATION IN SODA-PHOSPHATE GLASSES

S. SIMON[a], I. ARDELEAN[a], V. SIMON[a,*]

ABSTRACT. Soda-phosphate glasses incorporating uranium and thorium were investigated with respect to structural effect of UO_3 and ThO_2 content added to P_2O_5-Na_2O glass matrix, as well as to the structural effect of the self-irradiation of the actinide containing glass samples. XRD analysis proves the amorphous state of the as-prepared samples up to 20 mol %. FTIR results support the depolymerisation of the phosphate glass network by progressive increase of the amount of actinide oxide incorporated in the host glass. The self-irradiation determines the occurrence of structural defects evidenced by EPR analysis.

Keywords: *phosphate glasses; self-irradiation; structure.*

1. INTRODUCTION

Oxide glasses have potential application as suitable materials for the embedding and safe storage, i.e., for the immobilization and long-term confinement of nuclear wastes [1-4]. The property of these materials is to retard the release of radionuclides to the biosphere until their radioactivity is reduced to negligible levels. The introduction of radioactive isotopes in glass matrices will induce structural changes in the glass network. The soda-phosphate matrices enter as components of vitreous systems proposed for nuclear waste disposal [5]. The structural modification of the glass matrices induced by the incorporated radioisotopes may afect their stability and storage properties.

[a] *Babes-Bolyai University, Faculty of Physics & Interdisciplinary Research Institute on Bio-Nano Sciences, Cluj-Napoca, Romania*
* *Corresponding author: viosimon@phys.ubbcluj.ro*

This paper reports on structural changes occured in a soda-phosphate glass matrix hosting uranium and thorium, as evidenced by X-ray diffraction, infrared spectroscopy, and electron paramagnetic resonance spectroscopy.

2. EXPERIMENTAL

Glass samples incorporating up to 20 mol % UO_3 and ThO_2 in $2P_2O_5$ Na_2O glass matrix were prepared by melting of $(NH_4)_4HPO_4$, $Na_2CO_3 \cdot 10H_2O$, UO_3 and $Th(NO_3)_2 \cdot 4H_2O$, respectively, used as precursors of P_2O_5, Na_2O, UO_3 and ThO_2 oxides, respectively. The corresponding mixtures of reagents were melted at 1250 ^oC and quickly undercooled at room temperature by pouring in stainless crucibles.

The samples density was measured at room temperature using the Arhimedes method with decationized water as immersion fluid. X-ray diffraction analysis was carried out with Shimadzu LabX XRD-6000 diffractometer, using Cu K_α radiation (λ = 1.5405 Å) with Ni-filter. The measurements were performed in 2θ geometry, with a scanning speed of 5^o/min, for 2θ angles ranging between 10^o and 100^o. The operation voltage was 40 kV and the current was 30 mA. Fourier transform infrared (FTIR) spectra were recorded at a resolution of 4 cm^{-1} with a Bruker Equinox 55 spectrometer, at room temperature. Electron paramagnetic resonance measurements were performed at room temperature with a JEOL JES-3B spectrometer operating at 9.4 GHz (X-band).

3. RESULTS AND DISCUSSION

Density measurements indicate an increase of density values from 2.2 g/cm^3 for the host matrix to 2.5 g/cm^3 for the sample with 20 mol % actinide oxide. These values are not only on the account of samples composition, but they are also influenced by the degree of structural compactness due to geometrical configuration modifications in the glass network related to the coordination change of the former ions and the variation of dimensions of the interstitial holes [6]. The addition of UO_3 or ThO_2 leads to the increased breaking of the P-O-P bonds in the phosphate structural units and implicitely to the decrease of the number of bridging oxygens.

The XRD patterns of the as-prepared samples (Fig. 1) attest their vitreous state. For barium borosilicate glasses containing ThO_2 samples prepared at 1000 ^oC [3] three sharp peaks superimposed over the broad pattern were recorded at 27.6^o, 45.8^o and 54.3^o which are characteristic of crystalline ThO_2 [JCPDS - file card 42-1462] and denote a partial phase separation of ThO_2 in the glass matrix. The higher melting temperaure of our ThO_2-P_2O_5-Na_2O system impeded such a phase separation up to x = 20 mol % ThO_2.

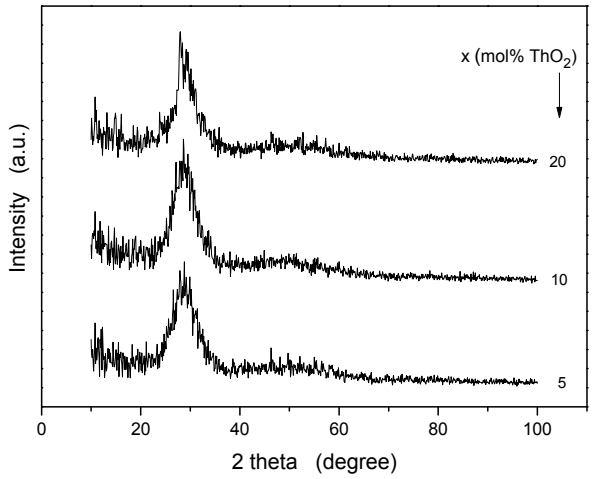

Fig. 1. XRD patterns of $xThO_2 \cdot (100\text{-}x)[2P_2O_5 \cdot Na_2O]$ samples

The FTIR spectra recorded from thorium containing samples (Fig. 2) consist of large absorption bands typical for the vitreous samples. The main absorption bands are centered around 485, 540, 615, 770, 920, 1120 and 1260 cm^{-1}. Absorption bands assignable to ThO_2 [7] are not detected. All these bands recorded in the spectral range up to 1300 cm^{-1} are assigned to vibrations of P–O bonds in $(PO_4)^{3-}$ structural units. The $(PO_4)^{3-}$ tetrahedra interconnected to form the phosphate glass network may occur as Q^3, Q^2, Q^1 and Q^0 species according to the number of the bridging oxygens in (PO_4) units, expressed by *n* in this Q^n notation.

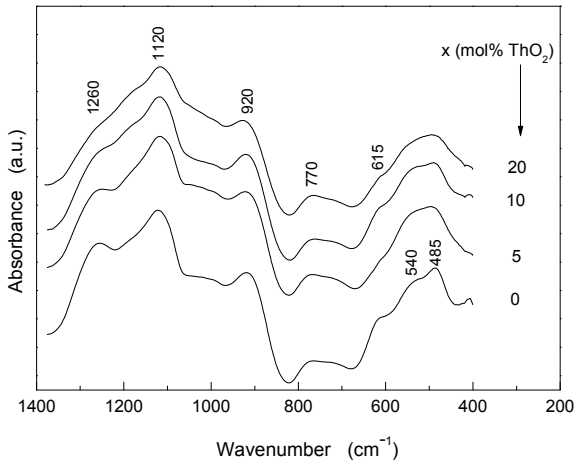

Fig. 2. FTIR spectra of $xThO_2 \cdot (100\text{-}x)[2P_2O_5 \cdot Na_2O]$ samples

The progressive addition of thorium influences the position of the infrared absorption bands, mainly a shift of 770 cm^{-1} band to lower wavenumbers is observed, as well as the broadining of all bands due to the increase of the structural disorder by enhancement of non-bridging oxygens on account of bridging oxygens shared by the phosphate tetrahedra. This structural change implies to a certain extent the glass network depolymerisation of ThO_2 hosting material.

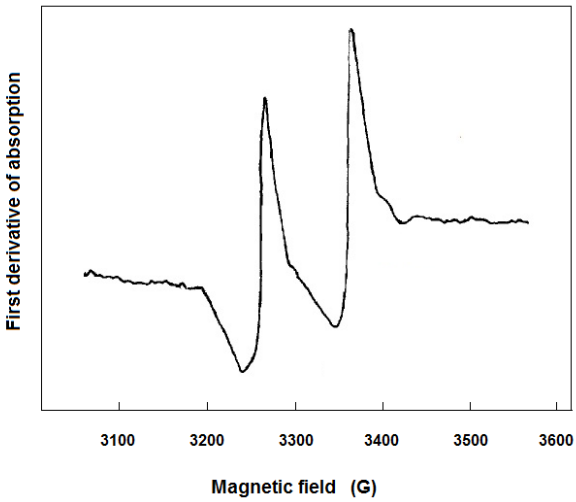

Fig. 3. EPR spectrum recorded from the sample containing 5 mol % UO_3.

The EPR spectra of as prepared samples embedding radioactive nuclides contain no resonance signal, but already after storage for a week an EPR signal (Fig. 3) arising from defects of electron trapped at a non-bridging oxygen vacancy type is observed [8]. The doublet structure is due to the interaction of the electron with the nearest of the neighboring phosphorus nuclei.

4. CONCLUSIONS

The investigation of $xUO_3 \cdot (100-x)[2P_2O_5 \cdot Na_2O]$ and $xThO_2 \cdot (100-x)[2P_2O_5 \cdot Na_2O]$ systems with $0 \leq x \leq 20$ mol % followed the structural changes in the glass matrix induced by increasing content of actinide oxide and by the inside delivered radiation. Actinides incorporation in P_2O_5-Na_2O glass matrix up to 20 mol % preserves the vitreous state of the as prepared samples. Nevertheless, actinide oxide addition causes the depolymerisation of the phosphate glass network as proved by FTIR spectroscopic results. Due to the self-irradiation owing to radioactive decay of the actinides, structural defects of oxygen vacancy type were evidenced by EPR spectroscopy.

REFERENCES

1. G. Karakurt, A. Abdelouas, J.-P. Guin, M. Nivard, T. Sauvage, M. Paris, J.-F. Bardeau, Understanding of the mechanical and structural changes induced by alpha particles and heavy ions in the French simulated nuclear waste glass*, J. Nucl. Mater.* (2016) 475, 243-254.
2. J.-H. Hsu, J.W.Newkirk, C.-W. Kim, R.K. Brow, M.E. Schlesinger, C.S. Ray, D.E. Day, The performance of Inconel 693 electrodes for processing an iron phosphate glass melt containing 26 wt.% of a simulated low activity waste, *J. Nucl. Mater.* (2014) 444, 323-330.
3. R.K. Mishra, V. Sudarsan, A.K. Tyagi, C.P. Kaushik,Kanwar Raj, S.K. Kulshreshtha, Structural studies of ThO2 containing barium borosilicate glasses, *J. Non-Cryst. Solids* (2006) 352, 2952–2957.
4. C.-W. Kim, D.E Day, Immobilization of Hanford LAW in iron phosphate glasses, *J. Non-Cryst. Solids* (2003) 331, 20-31.
5. V. Simon, Ionic field strength changes in soda-phosphate glasses induced by thorium, *Eur. Phys. J. Appl. Phys*. (2004) 25, 93-97.
6. L. Barbieri, A.B. Corradi, C. Leonelli, C. Siligardi, T.Manfredini, G.C. Pellacani, Effect of TiO_2 addition on the properties of complex aluminosilicate glasses and glass-ceramics, *Mater. Res. Bull.* (1997) 32, 637-648.
7. S. Simon, I. Ardelean, I. Bratu, D.U. Reckert, V. Simon, Nuclear activity and IR investigation of ThO_2-P_2O_5-Na_2O glasses, *Mater. Lett.* (1998) 37, 227–230.
8. V. Simon, I. Ardelean, O. Cozar, S. Simon, Valence states of uranium and gamma irradiation defects in sodaphosphate glasses, *J. Mater. Sci. Lett.* (1996) 15, 784-785.

STUDIA UBB PHYSICA, Vol. 61 (LXI), 1, 2016, pp. 53-62
(RECOMMENDED CITATION)

Dedicated to Professor Dr. Cozar Onuc on His 70th Anniversary

THE PRODUCTION OF THE RADIOISOTOPES ^{165}Dy, ^{166}Ho, ^{171}Er, ^{124}Sb FOR BRACHYTHERAPY USE

OANA FLORINA STAN[a], L. DARABAN[a*], C. COSAR[a], B. BARNA[a]

ABSTRACT. The thermal neutron cross-sections (σ) of the reactions ^{164}Dy(n,γ) ^{165}Dy, ^{165}Ho(n,γ)^{166}Ho, ^{170}Er(n, γ)^{171}Er, ^{123}Sb(n, γ)^{124}Sb were measured by the activation method. The powder samples were irradiated in an isotropic neutron field obtained from the ^{241}Am-Be and ^{239}Pu-Be neutron sources, moderated with paraffin wax. The γ-ray spectra from the irradiated samples were measured by high resolution γ-ray spectrometry with a calibrated n-type Ge detector. The thermal neutron cross-sections for the reactions studied has been determined to be: for ^{164}Dy(n,γ) ^{165}Dy reaction 2400±200 barns, for ^{165}Ho(n,γ)^{166}Ho reaction 55.3±12 barns, for ^{170}Er(n, γ)^{171}Er reaction 1.3±2 barns and for ^{123}Sb(n, γ)^{124}Sb reaction 3.5±0.5 barns. The thermal neutron cross sections for the reactions ^{164}Dy(n,γ) ^{165}Dy, ^{165}Ho(n,γ)^{166}Ho and ^{123}Sb(n, γ)^{124}Sb are in good agreement, within limits of uncertainty, with most of the values in the literature. The thermal neutron cross section for the reaction ^{170}Er(n, γ)^{171}Er was not in good agreement with the values in the literature, but it is a measurement that has been made, and it can be evaluated again in the future.

Keywords: *neutrons, gamma spectroscopy, capture reactions, effective section, isotopes radioactive*

1. INTRODUCTION

Brachytherapy dates back to 1901 and is commonly used as an effective treatment for cervical, prostate, breast, and skin cancer and can also be used to treat tumors in many other body sites. Radioactive seeds or sources are placed in or near the tumor itself, giving a high radiation dose to the tumor while reducing the radiation exposure in the surrounding healthy tissues. This work presents radioactive seeds that are obtained after a nuclear reaction with neutrons.

[a] *"Babes-Bolyai" University, Cluj-Napoca, Romania*
[*] *Corresponding author: liviu.daraban@phys.ubbcluj.ro*

Neutron activation cross-section data have become important for theoretical and experimental studies concerning the interaction of neutron with matter. There are some (n,γ) reactions that can be used to determine the thermal neutron cross-sections. The aim of this present work is to measure the cross-sections for dysprosium, holmium, erbium and antimony, respectively of the reactions: $^{164}Dy(n,\gamma)^{165}Dy$, $^{165}Ho(n,\gamma)^{166}Ho$, $^{170}Er(n,\gamma)^{171}Er$, and $^{123}Sb(n,\gamma)^{124}Sb$. An accurate determination of thermal neutron cross-section is important because it is generally used for reactivity control or adjustment in reactor cores and in-core flux measurements in very small distances of core lattices. We found in literature a number of experimental and evaluated data on the thermal neutron capture cross-sections for the reactions mentioned and we compared them with the results obtained in this work.

2. EXPERIMENTAL PROCEDURE

2.1. Neutron source

The irradiation of samples was performed by the neutrons from a combination of sources: a 33 Ci ^{239}Pu-^{9}Be source and a 5 Ci ^{241}Am-^{9}Be source which are immersed in paraffin moderator with (see Fig.1) a width of 3-4 centimeters in order to obtain 61.5 % thermal neutrons for a divergent flux. [1].

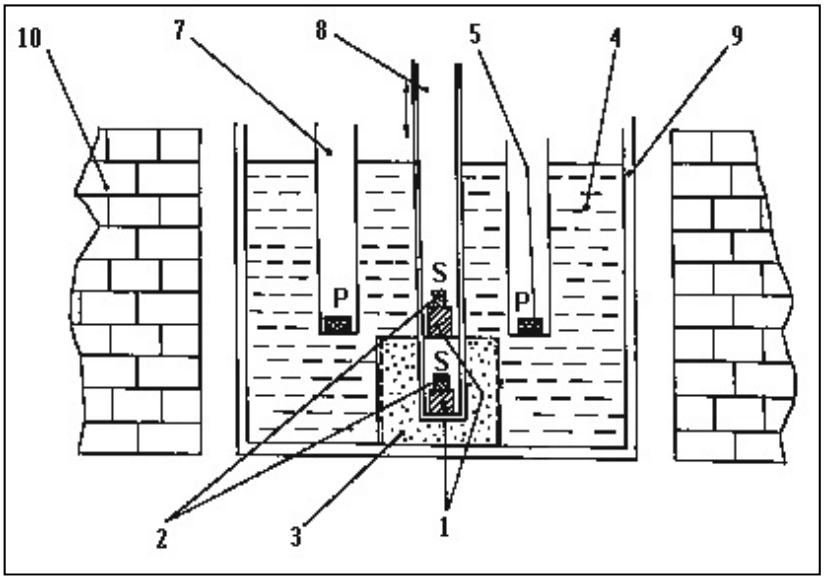

Fig. 1. Configuration of the neutron sources Am-Be and Pu-Be:
1) Am-Be source, 2) Pu-Be source, 3) boron paraffin, 4) pure paraffin for thermalization, 5) the sample introduced for irradiation, 7) irradiation channel, 8) central channel for fast neutrons irradiation, 9) Fe walls with paraffin, 10) boron paraffin bricks for protection.

2.2. Sample irradiation

The analysis is made on solid samples, transformed in powder: metallic Dy, erbium oxide powder (Er_2O_3), metallic Ho, metallic Sb. The samples are weighed out and the results are presented in Table 1.

Table 1. Weight of the samples

Sample	Weight (g)
Dy metalic	1.445
Ho metalic	1.1737
Er_2O_3	2.152 (1.882 Er_2)
Sb metalic	2.1529

After the thermalization of the neutrons in paraffin towards the irradiation channel, the neutrons are going to be captured by the samples, where the reactions ^{164}Dy(n,γ)^{165}Dy, ^{165}Ho(n,γ)^{166}Ho, ^{170}Er(n, γ)^{171}Er, ^{123}Sb(n, γ)^{124}Sb take place.

The samples were irradiated with a flux of $3.05 \cdot 10^5$ n/cm^2·s and the irradiation times for the reactions were chosen for a period greater than 3.5 half-lives, yielding enough activity to be measured in a γ-ray counting system (Table 2). [2]

Table 2. The half-lifes of the isotopes

The isotopes	Half-life ($T_{1/2}$)
^{165}Dy	2.3 h
^{166}Ho	26 h
^{171}Er	7.5 h
^{124}Sb	60 d

2.3. Measurement of activity

The induced gamma activities emitted from the activation samples were measured by using a high-resolution γ-ray spectrometer. The γ-ray spectrometer was a GC1019 type Canberra high-purity germanium (HPGe)-detector. The HPGe-detector was operated at liquid nitrogen temperature and was coupled with a 3106D Canberra type High-Voltage module, an Ortec amplifier and a computer-based multichannel analyzer. The detector was shielded by a lead armor NZ-138 type. The spectrum analysis was done using the Genie-2000 computer program. The detection efficiency for the γ-ray spectrometer was calibrated with a set of standard sources:

^{241}Am (59.541 keV), ^{22}Na (511.006 keV), ^{137}Cs (661.657 keV), ^{60}Co (1173.237 keV and 1332.501 keV). At the instant when the activation has been terminated, (t=0), the activity of the samples is given by the following expression:

$$\Lambda_0 = \frac{\sigma m N_A \phi \chi S}{M}, \quad (1)$$

where

Λ_0 [Bq] = the number of disintegrations per second of the element in the sample,
σ [cm^2] = cross-section of the reaction,
m [g] = mass of the target element,
N_A = Avogadro's number (6.023×10^{23} molecules/mole,
ϕ [neutrons/cm^2s] = neutron flux,
χ [%] fraction of the target isotope in the sample (isotopic abundance),
S = saturation factor, $1 - e^{-\lambda t}$ where $\lambda=0.693/T_{1/2}$, t = the irradiation time,
M = atomic weight of the element. [3]

Table 3. The molecular masses of the target elements and the isotopic abundance in nature of the initial radionuclides

Element	The molecular mass (M)	Isotop	Isotopic abundance χ (%)
Dy	162.5	^{164}Dy	28.18
Ho	164.9	^{165}Ho	100
Er	167.26	^{170}Er	14.91
Sb	121.76	^{123}Sb	42.64

In order to find out the cross-section σ, we have to determine the induced activity Λ_0. For this we will use the absolute activity using a thorium (Th) sample with his activity known. We use another formula:

$$\varepsilon_f = \frac{N_i}{\varepsilon_g \cdot \Lambda \cdot p_i \cdot t}, \quad (2)$$

where

N_i = the area under the photopeak,
ε_g = geometrical efficiency (the probability that a certain radiation falls on detector),
Λ = source activity (absolute),
p_i = decay fraction of the unknown activity, which is the fraction of the total disintegrations in which the measured gamma is emitted,
t = the measuring time of the spectrum [4]; for the measuring time we chose a value of 6 hours, in order to obtain all the photopeaks (radioisotopes) of Th.

Using some important photopeaks from the Th spectrum with the greatest p_i, we can obtain an efficiency curve that would be useful to find out the induced activity for whatever photopeak from the spectrum of the radioisotopes ^{165}Dy, ^{166}Ho, ^{171}Er, ^{124}Sb. (Figure 2, 3, 4 and 5)

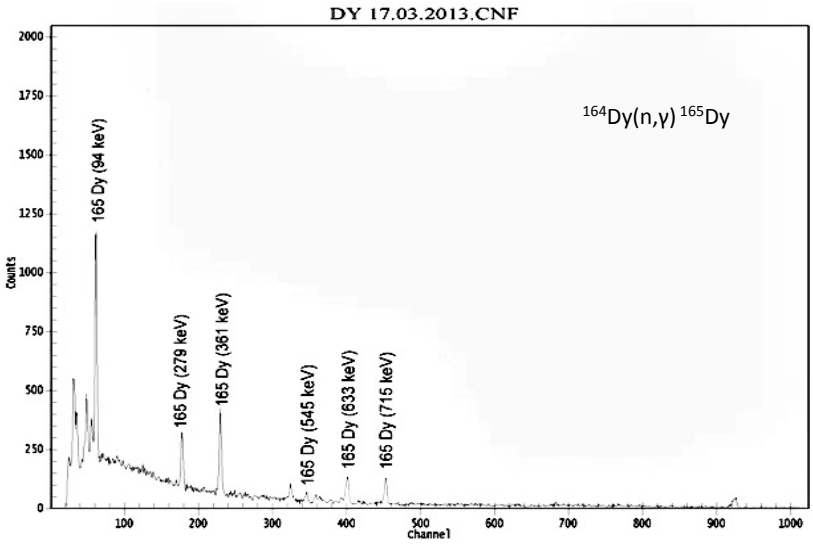

Fig. 2. The spectrum of ^{165}Dy showing the main radionuclides and their γ-energies in keV

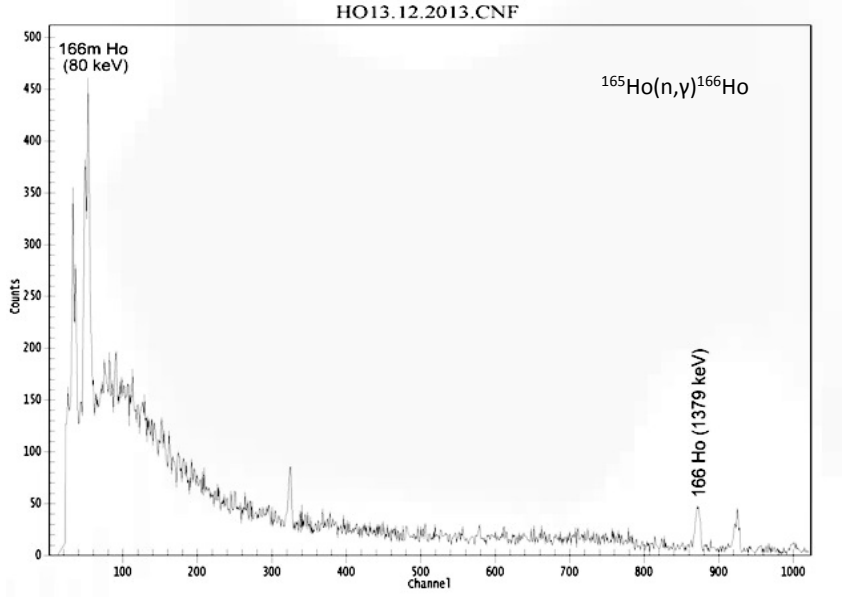

Fig. 3. The spectrum of ^{166}Ho showing the main radionuclides and their γ-energies in keV

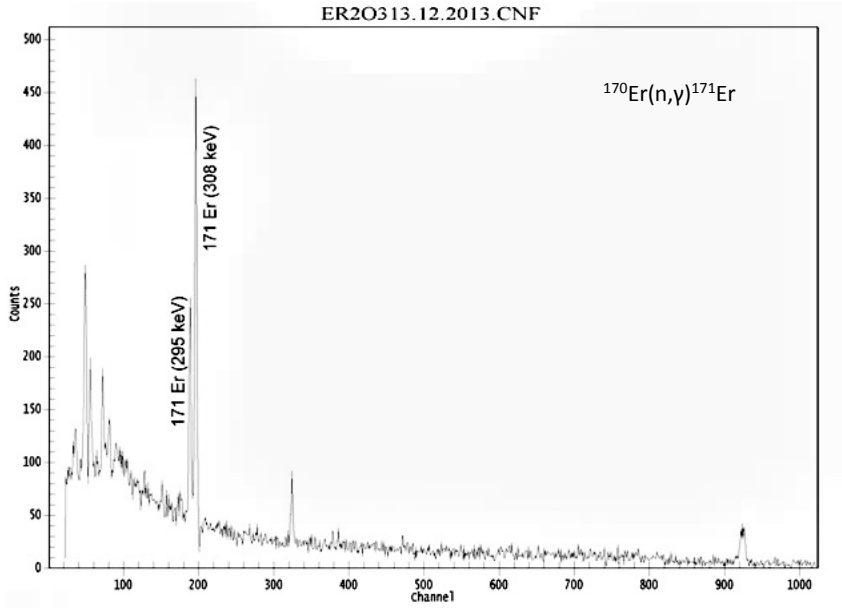

Fig. 4. The spectrum of ^{171}Er showing the main radionuclides and their γ-energies in keV

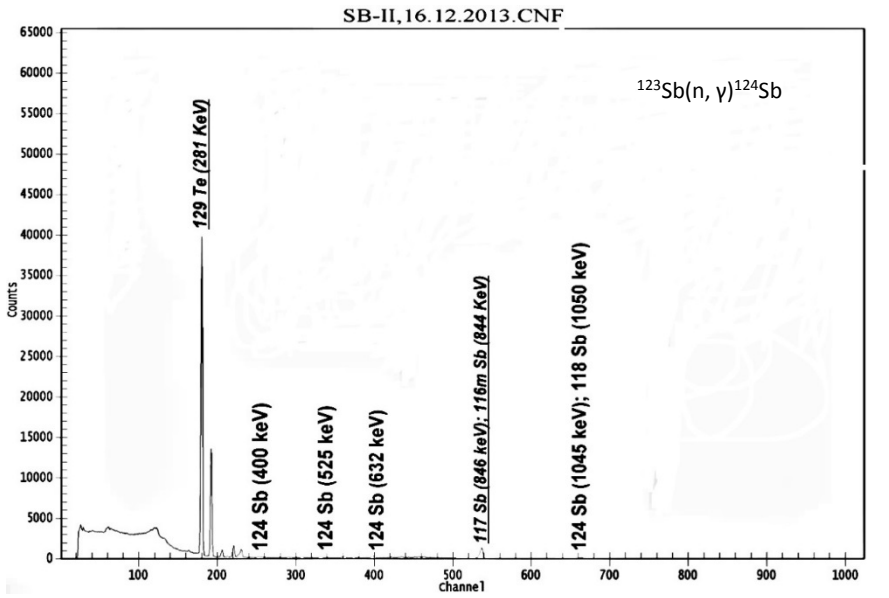

Fig. 5. The spectrum of ^{124}Sb showing the main radionuclides and their γ-energies in keV

To measure the activities of ^{164}Dy(n,γ)^{165}Dy, ^{165}Ho(n,γ)^{166}Ho, ^{170}Er(n, γ)^{171}Er, ^{123}Sb(n, γ)^{124}Sb reactions, we have chosen the γ-ray peaks with high intensity (p_i), well-separated, and relatively low background (Table 4).

Knowing the values from Table 3 too, we could calculate the cross-sections of the reactions using the formula (1).

Table 4. Nuclear data decay used for determination of the induced activity

Reaction	Main γ-rays		Activity
	Energy (keV)	Intensity p_i (%)	
^{164}Dy(n,γ)^{165}Dy	94	3.5784	146.0865504
	361	0.8400	
^{165}Ho(n,γ)^{166}Ho	80	12.7050	686.4544856
	1379	0.93	
^{170}Er(n, γ)^{171}Er	295	28.9	16.89549826
	308	64.4	
^{123}Sb(n, γ)^{124}Sb	253	99	750.5485954
	666	99.6	

3. RESULTS AND DISCUSSION

The thermal neutron cross-section for the ^{164}Dy(n,γ)^{165}Dy reaction given in Table 5 together with other literature values is 2400±200 barns. This value is close to within 4.16-4.76 % with the values obtained by RNAL, NGATLAS, JEF 2.2., Heft and Sehgal et al., but disagrees with the measurements of Johnsrud et al., Goldhaber and Muehlhause, Alstad et al. by 12.5-16.66 %.

Table 5. Thermal neutron cross-section for ^{164}Dy(n,γ) ^{165}Dy reaction

Year	References other works	Thermal neutron cross-section σ (barn)
2014	This work	2400±200
2005	Yucel [5]	2672±104
2001	Cho et al. [5]	2656±98
2000	RNAL [5] [55]	2520
1999	Holden [5]	2700
1998	ENDF/B-VI [5]	2651.63
1997	NGATLAS [5]	2520
1996	JEF 2.2 [5]	2520
1996	NuDat [5]	2650±100
1993	Griffin et al. [5]	2650±100

Year	References other works	Thermal neutron cross-section σ (barn)
1984	Simonits et al. [5]	2660±133
1984	Mughabghab [5]	2650±278
1978	Heft [5]	2300±200
1977	Lucas et al. [5]	2695
1976	Erdtmann [5]	2700±300
1974	Rzves and Zieba [5]	2700±200
1973	BNL [5]	2700±75
1972	Alstad et al. [5]	2800±110
1972	Fawcett et al. [5]	2700±200
1970	Vertebnyj et al. [5]	2740±45
1968	Goldman et al. [5]	2600
1968	Holden and Walker [5]	2600
1967	Scoville [5]	2600±410
1964	Esch and Feiner [5]	2700±200
1959	Sehgal et al. [5]	2490±300
1959	Johnsrud et al. [5]	2100
1958	House and Frost [5]	2750±150
1956	Walker [5]	2630±200

The thermal neutron cross-sections for the $^{170}Er(n, \gamma)^{171}Er$ reaction given in Table 6 together with other literature values is 1.3±2 barns. This value disagrees with all the values given by 69.7-89.33 %.

Table 6. Thermal neutron cross-section for $^{170}Er(n,\gamma)^{171}Er$ reaction

Year	References	Thermal neutron cross-section σ (barn)
2014	This work	1.3±2
2007	Yucel [7]	7.99±0.56
2003	De Corte [7]	8.86±0.35
1997	Knopf and Waschkowski [7]	15±1
1989	De Corte and Simonits [7]	8.85±0.27
1978	Heft [7]	6.0±1
1972	Glomset and Pappas [7]	5.8±0.3
1968	Vertebnyj et al. [7]	12±5
1967	Gilette [7]	5.70±0.15
1963	Mangal and Gill [7]	4.3±0.65
1954	Barnes [7]	8.72±1.78
2007	NuDat [7]	5.8±0.3
2006	ENDFB-VII [7]	8.85
2005	JEFF 3.1 [7]	5.776
2003	Kolotov and De Corte [7]	8.86±0.35

Year	References	Thermal neutron cross-section σ (barn)
2002	JENDL 3.3 [7]	5.776
1999	Holden [7]	6±1
1984	Mughabghab [7]	5.8±0.3
1976	BROND 2.2 [7]	5.8±0.12

The thermal neutron cross-sections for the ^{165}Ho(n,γ)^{166}Ho reaction given in Table 7 together with other literature values is 55.3±12 barns. This values is close to within 5.17-9.83 % with the values obtained by Holden, De Corte, Rajput et al., Nguyen, Yucei et al., but disagrees with the measurements of ENDF/B-VII.0, Mughabghab, Danon et al., JFF2.2, IAEA, Scoville and Rogers by 17.18-17.91 %.

Table 7. Thermal neutron cross-section for ^{165}Ho(n,γ)^{166}Ho reaction

Year	References	Thermal neutron cross-section σ (barn)
2014	This work	55.3±12
2010	Nguyen [8]	59.7±2.5
1997	S. I. Kafala [6]	61.2
2009	Rajput et al. [8]	58.98±2.1
2006	ENDF/B-VII.0 [8]	64.67
2005	Yucei et al. [8]	59.2±2.5
2003	De Corte [8]	58.5±1.3
2003	Mughabghab [8]	64.7±1.2
1999	Holden [8]	58
1998	Danon et al. [8]	64.4±2.8
1997	Katala et al. [8]	61.2±0.8
1994	JFF2.2 [8]	66.59
1989	De Corte [6]	58.1
1987	IAEA [6]	64.7
1987	Gryntakis et al. [8]	61.2±1.1
1984	Mughabghab [8]	61.2±1.1
1984	Simonits et al. [8]	61.2±3
1978	Heft [8]	61.4±1.0
1976	Erdtmann [8]	63±3.3
1974	Ryves and Zieba [8]	61.2±1.1
1972	Steinnes [8]	65±2
1969	Walker [8]	63
1968	Scoville and Rogers [8]	67
1967	THAI-AEC-10 [8]	64
1967	Zimmerman et al. [8]	60±2
1967	Stephenson [8]	67
1962	Keisch and Faler [8]	64±6
1951	Pomerance [8]	64±3

The thermal neutron cross-sections for the $^{123}Sb(n, \gamma)^{124}Sb$ reaction given in Table 8 together with other literature values is 3.5 ± 0.5 barns. This value is close to within 7.4-20.63 % with all the values given.

Table 8. Thermal neutron cross-section for $^{123}Sb(n,\gamma)^{124}Sb$ reaction

Year	References	Thermal neutron cross-section σ (barn)
2014	This work	3.5 ± 0.5
1997	S. I. Kafala [6]	4.41
1989	De Corte [6]	4.08
1987	IAEA [6]	4.156
1978	Heft [6]	3.78

4. CONCLUSIONS

The thermal neutron cross-sections for the $^{164}Dy(n,\gamma)^{165}Dy$, $^{165}Ho(n,\gamma)^{166}Ho$, $^{170}Er(n,\gamma)^{171}Er$, $^{123}Sb(n, \gamma)^{124}Sb$ reactions have been measured using the activation method and are almost all in good agreement with the values from literature.

REFERENCES

[1] T. Fiat, L. Dărăban, Instalaţie pentru analize de compoziţie bazate pe absorbţia neutronilor, *Studia UBB Physica*, 1976

[2] L. Dărăban, *Curs de fizică nucleară*, Universitatea Babeş-Bolyai, Cluj-Napoca, 2006

[3] EG & G ORTEC, *Neutron activation analysis* (slow neutrons), Experiment 17

[4] O. Cozar, *Detectori de radiaţii. Spectroscopie Gama*, Presa Universitară Clujeană, Cluj-Napoca, 2006

[5] M.Karadag, H. Yucel, Thermal neutron cross-section and resonance integral for $^{164}Dy(n,\gamma)^{165}Dy$ reaction, *Nuclear Instruments and Methods in Physics Research A,* vol. 550, pag. 626-636, 2005

[6] S. I. Kafala, T. D. MacMahon, S. B. Boryakov, Neutron activation for precise nuclear data, *Journal of Radioanalytical and Nuclear Chemistry,* vol. 215, pag. 193-204, 1997

[7] H. Yucel, M. Guray Budak, M. Karadag, Measurement of thermal neutron section and resonance integral for the ^{170}Er (n,γ) ^{171}Er reaction by using a ^{55}Mn monitor, *Physical Review C,* vol.l 76, 2007

[8] Van Do Nguyen, Duc Khue Pham, Tien Thanh Kim, Guinyun Kim, Manwoo Lee, Kyung Sook Kim, Heung-Sik Kang, Moo-Hyun Cho, In Soo Ko, Won Namkung, Measurement og thermal neutron section and resonance integral for the $^{165}Ho(n,\gamma)^{166g}Ho$ reaction using electron linac-based neutron source, *Nuclear Instruments and Methods in Physics Research B,* Vol. 269, pag. 159-166, 2011

STUDIA UBB PHYSICA, Vol. 61 (LXI), 1, 2016, pp. 63-74
(RECOMMENDED CITATION)

Dedicated to Professor Dr. Cozar Onuc on His 70th Anniversary

CONFORMATIONAL LANDSCAPE AND UV-VIS SPECTRUM OF S-BISOPROLOL

EMIL VINŢELER[a], VASILE CHIŞ[a,*]

ABSTRACT. The conformational changes of bisoprolol **(BISO)** are crucial for understanding its interaction with the receptor and the mechanism of action. Therefore, here we investigated the free energy conformational landscape of the free bisoprolol base, aiming at describing the 3D structures and energetic stability of its conformers. Twenty-three unique conformers, within an energy window of 2.44 kcal·mol^{-1} were identified by conformational search in gas-phase, at B3LYP/6-31+G theoretical level of theory. Among these, the 10 most stable were further refined in water at the same level of theory. The most stable conformers in gas-phase exhibit an S-shape structure. The most stable conformer was used to compute the absorption spectrum of bisoprolol.

Keywords: *bisoprolol; conformational landscape.*

1. INTRODUCTION

Bisoprolol with the IUPAC name (RS)-1-{4-[(2-isopropoxyethoxy)methyl] phenoxy}-3-(isopropylamino)propan-2-ol (BISO, see Fig. 1), is a cardio-selective beta1-adrenergic blocking agent, mainly used in the treatment of hypertension and heart failure [1-2]. Bisoprolol is a second generation agent, having higher beta-1 selectivity with respect to first generation agents like propranolol and timolol (that are non-selective to beta-1 and beta-2 adrenergic receptors) and to other second generations agents as metoprolol, atenolol and betaxolol [3-4]. The beta-blocker agents are usually administrated as racemic mixtures of S- and R-enantiomers and the affinity of these enantiomers to beta-1 and beta-2 adrenoceptors can be markedly different [5-7]. Bisoprolol is also provided as a racemic mixture where the S-enantiomer is

[a] *Babeş-Bolyai University, Faculty of Physics, 1 Kogălniceanu, RO-400084 Cluj-Napoca, Romania*
** Corresponding author: vasile.chis@phys.ubbcluj.ro*

responsible for most of the beta-1 blocking activity [8-9]. Due to higher beta-1 selectivity, [3H]-bisoprolol was used as radioligand to count the density of beta-1 adrenoceptors in different organs, especially in heart [9]. Having different affinities to beta-1 and beta-2 adrenoreceptors, [^{11}C]S-bisoprolol and its mirror form were used as radioligands in lung, heart and brain PET studies [10].

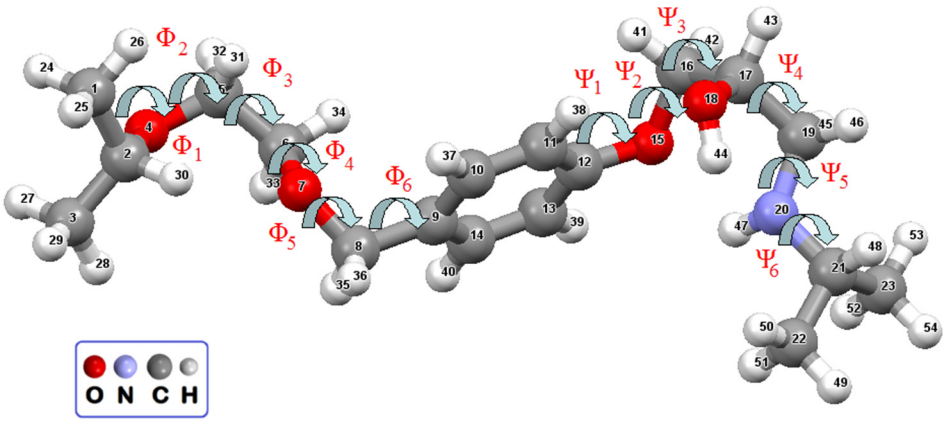

Fig. 1. Optimized molecular structures of the most stable conformer of S-bisoprolol in gas-phase at B3LYP/6-31+G level of theory, with the atom numbering scheme and the twelve dihedral angles defining the possible conformers.

The UV-Vis spectrum of bisoprolol in water and hydrochloric acid solution was obtained in work [11], in methanol with water [12] and with other drugs [13-14]. The absorption spectrum is influenced by Boltzmann populations of different conformers of bisoprolol. In this work we study the conformers in gas-phase and water and use the most stable conformer in water to compute the absorption spectrum of bisoprolol.

2. COMPUTATIONAL DETAILS

The conformational space of S-bisoprolol was initially explored with the Tinker software, using MMFF94 molecular mechanics force field [15] that has been developed based on quantum mechanics methods with the specific aims of being used in pharmaceutical science for predicting molecular geometries, conformational energies and energetic of drug-receptor interactions [16-19].

A systematic conformation search was performed using the MMFF94 molecular mechanics force field via Tinker software (convergence criterion was chosen to the default value of 10^{-4} kcal·mol^{-1}·Å^{-1}). This way, we identified 2x136x737=200464 conformations of BISO (136 conformers for fragment A and 737 conformers for fragment B within an energy window of 64 kcal·mol^{-1}, see fig. 1). The factor of two appears because there are two ways of gluing together fragments A and B to build the bisoprolol molecule. The fragment A contains the atoms 1-14 (see fig.1), while fragment B contains the atoms 9-23. They have in common the benzene group containing the atoms 9-14.

For the next part of the study we used the hybrid B3LYP exchange-correlation functional [20-23] in conjunction with Pople's 6-31+G basis set [24]. From the first most stable 23 unique conformers, whose relative free energies in gas-phase are lower than 2.44 kcal·mol^{-1} were selected the first 10 conformers and re-optimized in water at B3LYP/6-31+G level of theory. In Tables 1 and Fig. 2 are presented these first 10 most stable conformers whose relative free energies are less or comparable with the room temperature energy (0.592 kcal·mol^{-1}).

Frequency calculations confirmed that all the optimized geometries correspond to minima on the potential energy surface. The optimization of bisoprolol geometry and calculations of vibrational frequencies were performed with the Gaussian09 software package [25]. Boltzmann weighting factors for each conformer are derived at room temperature (T=298 K) by using the relative free energies (ΔG). The latter values are obtained from the frequency calculations including thermal corrections to energies [26]. Figures representing the structures of BISO have been created using the Mercury 3.3 [27] and Molegro Molecular Viewer [28] program packages.

3. RESULTS AND DISCUSSION

3.1. Conformation landscape

Bisoprolol conformers can be generated by varying the torsion angle around twelve rotatable bonds (see Fig. 1): C2-O4, O4-C5, C5-C6, C6-O7, O7-C8, C8-C9 and C12-O15, O15-C16, C16-C17, C17-C19, C19-N20, N20-C21. Table 1 summarizes the dihedral angles Φ_1-Φ_6 and Ψ_1- Ψ_6 that characterize the ten most stable conformers whose structures are shown in Fig. 2. Their names, relative Gibbs energies and populations are summarized in Table 2. Besides the ten most stable conformers, Fig. 2 includes also the optimized conformations of S- and R-bisoprolol obtained by using as starting geometries these ligands coupled with the beta-1 receptor ligand pocket structures found in two states (2VT4) [31] and (2Y03) [34].

Table 1. B3LYP/6-31+G calculated dihedral angles (degrees) characterizing the ten most stable *S*-bisoprolol conformers in water

Conformer	Φ_1	Φ_2	Φ_3	Φ_4	Φ_5	Φ_6
A1-B1-S (1)	76.4	177.8	74.4	175.2	69.1	68.7
A1'-B1-S (2)	-77.5	-176.9	-76.1	-179.5	-70.6	-69.7
A2-B1-S (3)	156.8	-92.7	73.6	-175.4	-67.9	-66.8
A3'-B1-S-(4)	-74.8	-174.0	-73.6	88.7	71.5	65.3
A2'-B1-S (5)	-157.3	92.8	-72.4	176.9	69.1	68.8
A3-B1-S (6)	76.4	174.9	74.9	-86.8	-72.1	-68.3
A2-B1-U (7)	156.7	-93.6	72.8	-174.4	-68.4	--69.9
A2-B2-S (8)	156.3	-93.2	72.3	-174.6	-69.1	-70.4
A4-B1-S (9)	74.2	172.8	-72.0	90.3	71.3	65.8
A3-B2-S (10)	75.2	174.1	74.0	-85.8	-71.9	-71.1
	Ψ_1	Ψ_2	Ψ_3	Ψ_4	Ψ_5	Ψ_6
A1-B1-S (1)	-26.4	105.4	47.8	-84.8	-152.6	170.7
A1'-B1-S (2)	-26.8	106.6	48.1	-85.0	-152.4	170.2
A2-B1-S (3)	-24.1	105.5	47.9	-84.9	-153.0	170.5
A3'-B1-S-(4)	-29.0	106.8	48.1	-85.2	-151.6	170.5
A2'-B1-S (5)	-26.7	106.3	48.0	-85.1	-152.5	170.2
A3-B1-S (6)	-26.3	106.1	48.4	-84.9	-153.7	170.4
A2-B1-U (7)	153.9	106.0	47.9	-85.5	-151.6	170.0
A2-B2-S (8)	-24.7	105.4	48.4	-84.1	-156.3	76.4
A4-B1-S (9)	-28.8	107.2	48.5	-85.3	-152.3	170.4
A3-B2-S (10)	-27.6	106.3	48.5	-83.7	-156.5	76.6

(1)

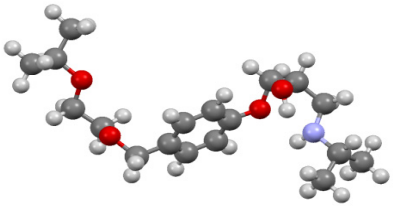

(2)

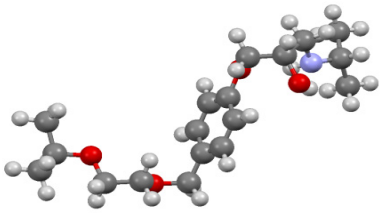

(3)

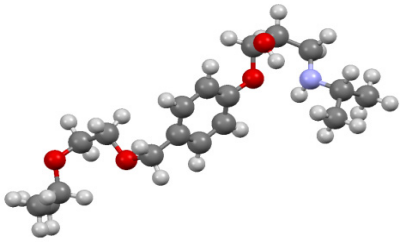

(4)

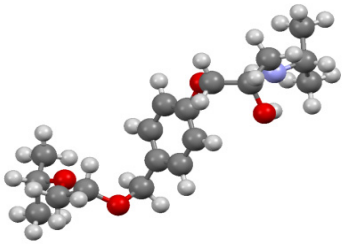

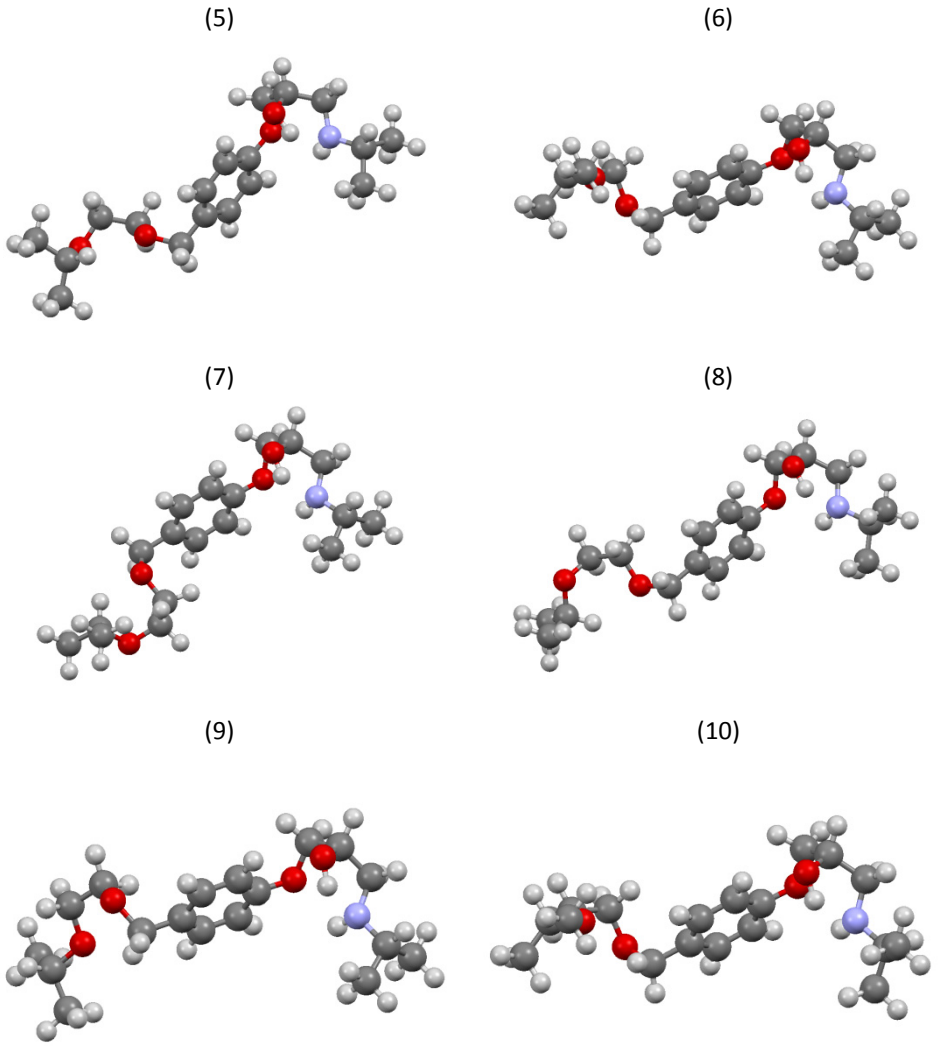

Fig. 2. B3LYP/6-31+G optimized structures of the ten most stable S-bisoprolol conformers in water.

It is important to note here that for bisoprolol's conformers there are two kind of structural transformations that do not affect their energies: the first one is related to the rotation of benzene ring along the C9-C12 axis, while keeping unchanged all the other dihedrals. Such transformations involve changes of the dihedrals Φ_6 (O7-C8-C9-C10) $\rightarrow$ O7-C8-C9-C14 and Ψ_1 (C11-C12-O15-C16) $\rightarrow$ C13-C12-O15-C16.

Another transformation that changes the structure, but not the energy, is the mirror symmetry related to transformation of dihedral angle $\Phi_6 \rightarrow 180 - \Phi_6$ and $\Psi_1 \rightarrow 180 - \Psi_1$ and the change of sign of the other five dihedral angles Φ and Ψ. To avoid counting the symmetry-related conformations, only those conformers are considered in Table 2 that have the sixth dihedral angle Φ_6 between -70° and 70° and the first dihedral angle Ψ_1 negative.

Table 2. Relative free energies and Boltzmann populations of the ten most stable conformers of S-bisoprolol in gas-phase and water (B3LYP/6-31+G level of theory) at room temperature

Conformer	Gas-phase B3LYP/6-31+G		Water B3LYP/6-31+G	
	ΔG (kcal·mol^{-1})	Population (%)	ΔG (kcal·mol^{-1})	Population (%)
A1-B1-S (1)	0.45	8.13	0.00	33.29
A1'-B1-S (2)	0.51	7.42	0.27	21.07
A2-B1-S (3)	0.01	17.08	0.68	10.73
A3'-B1-S-(4)	0.37	9.41	0.86	7.94
A2'-B1-S (5)	0.00	17.35	1.05	5.77
A3-B1-S (6)	0.19	12.53	1.10	5.26
A2-B1-U (7)	0.60	6.35	1.11	5.17
A2-B2-S (8)	0.48	7.81	1.17	4.68
A4-B1-S (9)	0.46	8.05	1.36	3.43
A3-B2-S (10)	0.65	5.87	1.51	2.67

The conformational analysis shows that for each dihedral angle there are three different conformers (when the third atom involved in dihedral angle is carbon) and two different conformers (when the third atom involved in dihedral angle is oxygen or nitrogen). The number of different conformers of fragment A is $2^2 \cdot 3^4 = 324$, the theoretical maximum value being larger than 136, the value obtained with Tinker software and MMFF94 force field, due to steric interactions. The number of different conformers of fragment B is $2^4 \cdot 3^4 = 1296$, where the number of conformers is doubled two times, one time due to the chiral center and the second time due to two orientations of hydroxyl group. The theoretical maximum value for fragment B is larger than 737, the value obtained with Tinker software and MMFF94 force field, due to steric interactions. The fragments A and B have benzene group in common that act as space separator and the conformers with low energy of the two fragments are practically independent in bisoprolol. The fragments A and B can be glued together in bisoprolol on the same side (U-like shape) or on different sides (S-like shape) relative to benzene plane giving a total number 2x136x737=200464 of conformations of bisoprolol molecule.

In Table 1 it can be seen that the ten most stable conformers contain only two unique fragments B and seven unique fragments A with minor changes of dihedral angles that glue together in nine S-like shapes and one U-like shape. The fragments B1 and B2 differ only in the sixth dihedral angle Ψ_6, but for fragments A is a greater variety with all dihedral angles being different. However this variety is only apparent, because the pairs A1 and A1', A2 and A2' and also fragments A3 and A3' are mirror forms with respect to a plane perpendicular to benzene plane. The energy difference between conformers **(3)** and **(5)** having fragments A2 and A2' respectively is only 0.01 kcal·mol^{-1} in gas-phase, but is a significant 0.37 kcal·mol^{-1} in water (see Table 2). The conformers **(6)** and **(9)** having fragments A3 and A3' have large energy differences in gas-phase as well as in water.

The most stable conformer of S-bisoprolol in gas-phase is conformer **(5)** and in water is conformer **(1)** (see Table 2). The energy difference 0.43 kcal·mol^{-1} of conformer **(3)** and **(7)** is determined by the different gluing of fragments A2 and B1 in S-shape and U-shape respectively.

3.2. UV-VIS spectrum of bisoprolol

The experimental absorption spectrum of bisoprolol fumarate in water [11] (see Fig. 3) is characterized by absorption maxima at wavelengths of 229 nm, 271 nm and a shoulder at 276 nm. The simulated spectrum of S-bisoprolol monomer (see Fig. 3) presents an absorption maximum at wavelength of 229.1 nm. The simulated spectrum of fumaric acid alone presents an absorption maximum at wavelength of 231.5 nm and has the same intensity with that bisoprolol monomer. The absorption of fumaric acid is obscured by bisoprolol due to the stochiometry of 2:1 in bisoprolol fumarate and cannot be responsible for the peak at wavelength of 271 nm. In Table 3 it is observed another mild absorption band of bisoprolol monomer at wavelength of 249.4 nm. This band could be enhanced and shifted to larger wavelengths by the interaction of bisoprolol monomer with fumaric acid as happens with other salts dissolved in water. In work [11] was obtained also the absorption spectrum for bisoprolol in hydrocloric acid solution indicating a decrease in the intensity of peak at wavelength of 229 nm, but not of that at 271 nm. The ionization state of the weak fumaric acid is influenced by modification of pH having two acid dissociation constants of 3.03 and 4.44. The increase of pH decreases the amount of fumaric acid and the intensity of peak at 229 nm. The fact that the peak at wavelength of 271 nm is not influenced by modification of pH indicates that it is not due to interaction bisoprolol-fumaric acid, another possibility being the formation of bisoprolol dimmers. We conclude that the absorption maximum at wavelength of 271 nm might be produced by the absorption band at 249.4 nm of bisoprolol molecule that is shifted and enhanced by the interaction with another bisoprolol monomer.

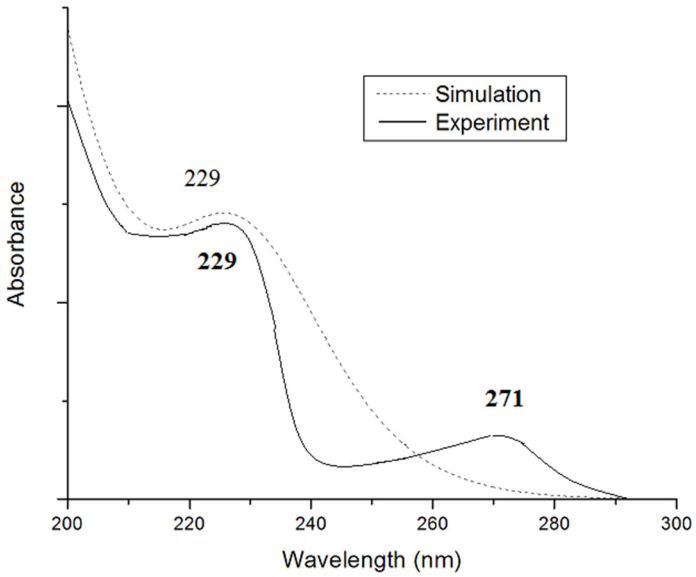

Fig. 3. The experimental absorption spectrum ob bisoprolol fumarate [11] and simulated absorption spectrum of the most stable conformer of S-bisoprolol, at B3LYP/**6-31+G** level of theory, in water at room temperature.

Table 3. TD-DFT B3LYP/6-31+G calculated electronic transitions of the most stable conformer (1) of bisoprolol in water at room temperature

λ(nm)	f[a)]	Transitions	Contributions %
249.4	0.0262	H→L	54.34
		H→L+1	22.19
230.1	0.0557	H-1→L+1	78.78
229.1	0.2373	H→L+1	39.15
		H→L	20.37
218.8	0.0251	H→L+2	69.79
214.0	0.0274	H-5→L+2	39.07
		H-2→L+1	34.38
206.9	0.0292	H-2→L+1	26.89
		H-3→L	21.61
203.8	0.0552	H→L+4	75.42
201.1	0.0341	H→L+5	30.21
		H→L+6	25.81

[a)]only transitions with f>0.025 are included

In Table 3 are shown the simulated absorption bands of the most stable conformer (1) of bisoprolol with the main band around 229 nm, due mainly to HOMO → LUMO + 1 transition and HOMO→LUMO transition. The experimental spectrum (see Fig. 3) shows the increase of absorbance for wavelengths near 200 nm indicating the presence of another important peak for wavelengths lower than 200 nm. Indeed, the simulated absorption spectrum indicates the existence of a peak at wavelength of 186 nm (not listed in Table 3) with the intensity three times larger than that of the peak at wavelength of 229 nm.

4. CONCLUSIONS

Using molecular mechanics and DFT quantum chemistry methods we characterized the ten most stable conformers of S-BISO with relative free energies in water within 1.51 kcal·mol^{-1}. The simulated absorption peak of the most stable conformer of S-bisoprolol presents a peak at wavelength of 229 nm in good agreement with the experimental data [11]. However the peak at wavelength of 271 nm requires a further investigation and most probable is determined by bisoprolol dimmers.

REFERENCES

[1] Prichard BN (1987) Bisoprolol: a new beta-adrenoceptor blocking drug. *Eur Heart J. Suppl M:* 121-129.

[2] Lancaster SG, Sorkin EM (1988) Bisoprolol. A preliminary review of its pharmacodynamic and pharmacokinetic properties, and therapeutic efficacy in hypertension and angina pectoris. *Drugs*. 36(3):256-285.

[3] Wellstein A, Palm D, Belz GG (1986) Affinity and selectivity of β-adrenoceptor antagonists in vitro. *J Cardiovasc Pharmacol* 8 (Suppl. 11): 36–40.

[4] Wellstein A, Palm D, Belz GG, Leopold G, Bühring KU, Pabst J. (1986) Concentration kinetics of propranolol, bisoprolol and atenolol in humans assessed with chemical detection and a subtype selective adrenoceptor*, J Cardiovasc Pharmacol* 8 (Suppl 11): 41-45.

[5] Morris T, Kaumann AJ (1984) Different steric characteristics of b1- and b2-adrenoceptors. *Naunyn-Schmiedebergs Arch. Pharmacol*., 327, 176-179.

[6] Wahlund G, Nerme V, Abrahamsson T, Sjöquist PO (1990) The beta 1- and beta 2-adrenoceptor affinity and beta 1-blocking potency of S- and R-metoprolol. *Br J Pharmacol* 99(3): 592-596.

[7] Nathanson JA (1988) Stereospecificity of beta adrenergic antagonists: R-enantiomers show increased selectivity for b2 receptors in ciliary process. *J. Pharmacol. Exp. Ther.* 245: 94-101.

[8] Brodde OE (1986) Bisoprolol (EMD 33512), a highly selective b1-adrenoceptor antagonist: in vitro and in vivo studies. *J. Cardiovasc. Pharmacol*. 8: 29-35

[9] Kaumann AJ, Lemoine H (1985) Direct labelling of myocardial b1-adrenoceptors - comparison of binding affinity of 3H-(-)- bisoprolol with its blocking potency. *Naunyn-Schmiedeberg's Arch. Pharmacol*. 331: 27-39.

[10] Soloviev DV, Matarrese M, Moresco RM, Todde S, Bonasera TA, Sudati F, Simonelli P, Magni F, Colombo D, Carpinelli A, Kienle MG, Fazio F. (2001) Asymmetric synthesis and preliminary evaluation of (R)- and (S)-[11C]bisoprolol, a putative beta1-selective adrenoceptor radioligand. *Neurochem Int*. 38(2):169-180.

[11] Vislous OO, Bevz NYu, Georgiyants VA, Zhivora NV (2014) Development of the "dissolution" test for bisoprolol tablets *News Pharm.* 1(77):49-53.

[12] Kumbhar ST, Shinde PP, Shinde DB, Solankar PB (2013) Visible Spectrophotometric Method For Estimation Of Bisoprolol From Its Bulk And Tablet Formulation. *Asian J Pharm Clin Res* 6(4):103-105

[13] Wedian F, Lataifeh A (2013) Application of the Bivariate Calibration for Simultaneous Determinations of Hydrochlorothiazide/Enalapril Maleate and Hydrochlorothiazide/ Bisoprolol Fumarate in Drug Tablets. *Int J Chem*. 5(2):29-37

[14] Kakde RB, Kotak VH, Barsagade AG, Chaudhary NK, Kale DL (2008) Spectrophotometric Method for Simultaneous Estimation of Amlodipine Besylate and Bisoprolol Fumarate in Pharmaceutical Preparations. *Research J. Pharm. and Tech*. 1(4):513-515

[15] Shi Y, Xia Z, Zhang J, Best R, Wu C, Ponder JW, Ren P (2013) Polarizable atomic multipole-based AMOEBA force field for proteins. *J Chem Theory Comput* 9:4046–4063.

[16] Halgren TA (1996) Merck molecular force field. I. Basis, form, scope, parameterization, and performance of MMFF94. *J Comput Chem* 17:490–519.

[17] Halgren TA (1996) Merckmolecular force field. II.MMFF94 van der Waals and electrostatic parameters for intermolecular interactions. *J Comput Chem* 17:520–552.

[18] Halgren TA (1996) Merck molecular force field. III. molecular geometries and vibrational frequencies for MMFF94. *J Comput Chem* 17:553–586.

[19] Halgren TA (1996) Merck molecular force field. IV. Conformational energies and geometries for MMFF94. *J Comput Chem* 17:587–615.

[20] Becke AD (1993) Density-functional thermochemistry. III. The role of exact exchange. *J Chem Phys* 98:5648–5652.

[21] Lee C, Yang W, Parr RG (1988) Development of the Colle-Salvetti correlation-energy formula into a functional of the electron density. *Phys Rev B* 37:785–789.

[22] Vosko SH, Wilk L, Nusair M (1980) Accurate spin-dependent electron liquid correlation energies for local spin density calculations: a critical analysis. *Can J Phys* 58:1200–1211.

[23] Stephens PJ, Devlin FJ, Chabalowski CF, Frisch MJ (1994) Ab initio calculation of vibrational absorption and circular dichroism spectra using density functional force fields. *J Phys Chem* 98:11623–11627.

[24] Hehre WJ, Ditchfield R, Pople JA (1972) Self—consistent molecular orbital methods. XII. further extensions of gaussian—type basis sets for use in molecular orbital studies of organic molecules*. J Chem Phys* 56:2257–2261.

[25] Frisch MJ, Trucks GW, Schlegel HB, Scuseria GE, Robb MA, Cheeseman JR, Scalmani G, Barone V, Mennucci B, Petersson GA, Nakatsuji H, Caricato M, Li X, Hratchian HP, Izmaylov AF, Bloino J, Zheng G, Sonnenberg JL, Hada M, Ehara M, Toyota K, Fukuda R, Hasegawa J, Ishida M, Nakajima T, Honda Y, Kitao O, Nakai H, Vreven T, Montgomery JA Jr, Peralta JE, Ogliaro F, Bearpark M, Heyd JJ, Brothers E, Kudin KN, Staroverov VN, Keith T, Kobayashi R, Normand J, Raghavachari K, Rendell A, Burant JC, Iyengar SS, Tomasi J, Cossi M, Rega N, Millam JM, Klene M, Knox JE, Cross JB, Bakken V, Adamo C, Jaramillo J, Gomperts R, Stratmann RE, Yazyev O, Austin AJ, Cammi R, Pomelli C, Ochterski JW, Martin RL, Morokuma K, Zakrzewski VG, Voth GA, Salvador P, Dannenberg JJ, Dapprich S, Daniels AD, Farkas O, Foresman JB, Ortiz JV, Cioslowski J, Fox DJ (2010) GAUSSIAN 09 C.01. Wallingford, Gaussian Inc.

[26] Willoughby PH, Jansma MJ, Hoye TR (2014) A guide to small molecule structure assignment through computation of (^{1}H and ^{13}C) NMR chemical shifts. *Nat Protoc* 9:643–660.

[27] Macrae CF, Edgington PR,McCabe P, Pidcock E, Shields GP, Taylor R, Rowler M, van de Streek J (2006) Mercury: visualization and analysis of crystal structures. *J Appl Crystallogr* 39:453–457.

[28] Molegro Molecular Viewer, version 2.5. Molegro ApS; Aarhus, Denmark: 2012.

[29] Dewar MJS, Thiel W (1977) Ground-States of Molecules. 38. The MNDO Method: Approximations and Parameters, *J. Am. Chem. Soc*. 99: 4899-4907.

[30] Dewar MJS, Zoebisch EG, Healy EF, (1985) AM1: A New General Purpose Quantum Mechanical Molecular Model*, J. Am. Chem. Soc.* 107: 3902-3909.

[31]Warne T, Serrano-Vega MJ, Baker JG, Moukhametzianov R, Edwards PC, Henderson R, Leslie AG, Tate CG, Schertler GF (2008) Structure of a beta1 adrenergic G-protein-coupled receptor. *Nature* 454:486–491.

[32]Moukhametzianov R, Warne T, Edwards PC, Serrano-Vega MJ, Leslie AG, Tate CG, Schertler GF (2011) Two distinct conformations of helix 6 observed in antagonist-bound structures of a beta1 adrenergic receptor. *Proc Natl Acad Sci* USA 108:8228–8232.

[33]Warne T, Edwards PC, Leslie AG, Tate CG (2012) Crystal structures of a stabilized beta1 adrenoceptor bound to the biased agonists bucindolol and carvedilol. *Structure* 20: 841–849.

[34]Warne T, Moukhametzianov R, Baker JG, Nehme´ R, Edwards PC, Leslie AG, Schertler GF, and Tate CG (2011) The structural basis for agonist and partial agonist action on a beta1 adrenergic receptor. *Nature* 469:241–244.

[35] Rasmussen SG, Devree BT, Zou Y, Kruse AC, Chung KY, et al. (2011) Crystal structure of the beta(2) adrenergic receptor-Gs protein complex. *Nature* 477: 549–555.
[36] Kenakin T, (2002) Drug efficacy at G protein-coupled receptors, *Annu. Rev. Pharmacol. Tox*, 42:349-379.
[37] Borchard U (1998) Pharmacological properties of β-adrenoceptor blocking drugs, *J Clin Bas Cardiol* 1: 5.
[38] Kobilka BK, Deupi X (2007) Conformational complexity of G-protein-coupled receptors, *Trends Pharmacol. Sci.* 28(8): 397-406.
[39]Bhattacharya S, Hall S, Li H, Vaidehi N (2008) Ligand-Stabilized Conformational States of Human β2 Adrenergic Receptor: Insight into G-Protein-Coupled Receptor Activation. *Biophys. J.* 94: 2027–2042.
[40] Bhattacharya S, Vaidehi N (2010) Computational Mapping of the Conformational Transitions in Agonist Selective Pathways of a G-Protein Coupled Receptor. *J. Amer. Chem. Soc.* 132: 5205–5214.

STUDIA UBB PHYSICA, Vol. 61 (LXI), 1, 2016, pp. 75-81
(RECOMMENDED CITATION)

Dedicated to Professor Dr. Cozar Onuc on His 70th Anniversary

IDENTIFICATION OF ALKALOIDS IN THE *CLAVICEPS PURPUREA* FUNGUS

I. BRATU[a*], C. MARUTOIU[b], Z. MOLDOVAN[a], IRINA KACSO[a], SIMINA DREVE[a] AND DELIA NICA BADEA[c]

ABSTRACT. Modern nutritionists worldwide require quality foods, based on crude vegetables and breads. Important nutritional benefits are provided by bakery products based on rye (*Secale cereale L.*), still contaminated rye flour with the fungus *Claviceps purpurea* may occur. Still a lot of dangerous substances can be found accidentally in natural products, causing accidental intoxication or even death. The present case study is meant to find quick analysis on unprocessed rye flour, *Secale cereale,* in order to define the presence of main compounds indicating contamination with *Claviceps purpurea.* Qualitative analysis using spectrofluorimetry confirmed literature data and revealed presence of gluten, ergometrine, growth factors, ergoalkaloids, lysergic acid and starch.

Keywords: *qualitative analysis,* Claviceps purpurea *fungus, alkaloids, rye flour, bread, spectrofluorimetry*

INTRODUCTION

Naturally produced alkaloids can be found in plants, synthesized for protection against herbivores and other enemies. For example common plant families which produce tropane alkaloids are the Brassicaceae (mustard family), Solanaceae (nightshade or potato family) Gramineae (rye) and Erythroxylaceae (coca family) [1].

[a] *National Institute for Research and Development of Isotopic and Molecular Technologies, 67-103 Donát, 400293, Cluj-Napoca, Romania*

[b] *"Babes-Bolyai" University Cluj-Napoca, Faculty of Orthodox Theology, Nicolae Ivan st, 400609 Cluj-Napoca, Romania*

[c] *Constantin Brancusi University, 30 Eroilor st., 210135 Tg. Jiu, Romania*

* *Corresponding author: ibratu@itim-cj.ro*

Claviceps purpurea is a fungus growth in food grain during wet seasons, particulary in rye. Ingested it disturbes activity of Central Nervous System, producing a disease named "ergotism" and, eventually, death [2]. Vasospasm related to ergot intoxication has been recognized since the Middle Ages, when it occurred due to ingestion of rye contaminated with the mold *Claviceps purpurea*. Today ergotism is a rare cause of peripheral ischaemia, most often associated with ergotamine tartrate therapy for migraine headaches [3]. Nevertheless, an awareness of this condition is important, as cases of ergotism may still occur. At present the dose of alkaloids in *Claviceps purpurea* in relation with the fungal species and, respectively, of geographical distribution of host plant it's not known. For example alkaloids from *Claviceps purpurea grown* up on rye (*Secale cereale L.)* are different than those grown up in/on other grasses. In order to identify and monitor all the factors responsible in speciation of alkaloids generated by *Claviceps purpurea* in every kind of grasses, targeted and performant research have to be organized [4].

Last decade specific literature contains some important references on qualitative and quantitative analysis of bioactive drugs of natural origin using fluorimetry principles. Techniques for the analysis of drug samples are classified into three categories (see Table 1) based on their maximum potential discriminating power. However, the classification of a technique may be lower, if the sample, analyte or mode of operation diminishes its discriminating power. Examples of combination of analytic techniques in efficient analysis of alkaloids may include:

- an infrared spectroscopy technique applied to a mixture which produces a combined spectrum;

- a mass spectrometry technique which only produces molecular weight information.

Categories of analytic techniques are determined mainly upon their complexity versus time and efficiency of results, meaning that most simple and rapid-giving useful information (confirming or denying the presence of a certain compound in the examined sample) are methods included in category C, and the most detailed information being obtained after careful examination using category A methods.

Table 1: Categories of Analytical Techniques [5].

Category A	*Category B*	*Category C*
Infrared Spectroscopy	Capillary Electrophoresis	Color Tests
Mass Spectrometry	Gas Chromatography	Fluorescence Spectroscopy
Nuclear Magnetic Resonance Spectroscopy	Ion Mobility Spectrometry	Immunoassay
Raman Spectroscopy	Liquid Chromatography	Melting Point
X-ray Diffractometry	Microcrystalline Tests	Ultraviolet Spectroscopy

Rapid and efficient analytic techniques applied for quality control of common commercial products is widely reported, as modern bioprocess control of biomass, protein, and alkaloid concentrations during cultivation of *Claviceps purpurea,* using fluorescence spectroscopy, presenting the applicability of this instrumental analysis for bioproducts control and monitoring [5, 6].

FLUORESCENCE SPECTROSCOPY-METHOD

The fluorimetry gives enhanced sensitivity over other "Category C" analytic methods for those compounds which are naturally fluorescent. Drugs with good fluorophores include several antimalarials, natural alkaloids such as ergometrine, lysergic acid diethylamine (LSD), tetracycline derivatives, propanolol and derivatives, etc. Generally more rigid the substituted aromatic structures give increased fluorescence [10]. Excitation spectra are usually used to confirm the identity of components and to select an optimum excitation wavelength for quantitative analysis. The emission spectrum is then used for qualitative and quantitative analytic applications.

The fluorescence measurements were performed on rye flour and on *Claviceps purpurea sclerotia* powder respectively using the ABLE & JASCO FP-6500 spectrofluorimeter equipped with a xenon flash lamp for the excitation light. The measurements were carried out exciting the solid samples (disposed in a specific holder for solid samples) at excitation wavelengths corresponding to the main compounds possible to be found in the samples. For all the measurements an excitation band width of 3 *nm* and an emission band width of 5 *nm* were applied.

RESULTS AND DISCUSSION

In Fig. 1 the fluorescence spectra of flour of *Secale cereale* (SC) and *Claviceps purpurea* (CP) for gluten identification are represented.

Emission maxima at 318 *nm* and at 410 *nm* respectively found in both *Secale cereale* (SC) and of *Claviceps purpurea* (CP) samples are in good agreement with literature data [8]; the differences noticed are mainly due to the examination of analytically unprocessed samples in our present case study. Identification of ergot alkaloids in different products by HPLC with fluorescence detector is early reported in literature [9]. For excitation at 320 *nm* ergometrine and their derivatives fluoresce at an emission wavelength of 405 *nm*, as it is represented in Fig. 2, but most probably is a non-specific emission, or is covered by the gluten emission occurred at 410 *nm* [11, 12].

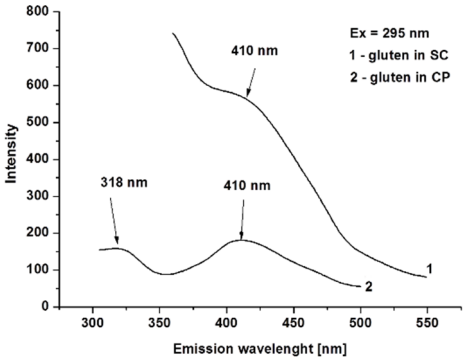

Fig. 1. Fluorescence spectra of flour of *Secale cereale* (SC) and of *Claviceps purpurea* (CP)

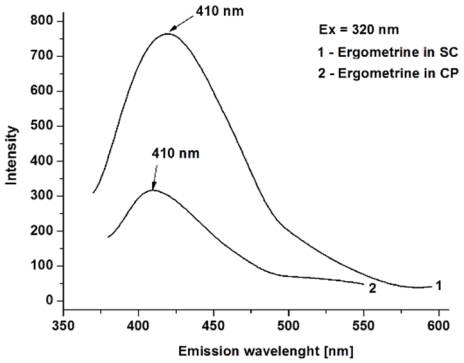

Fig. 2. *Fluorescence spectra of flour of* Secale cereale *(SC) and of* Claviceps purpurea *(CP) for the ergometrine identification*

In Fig 3 the fluorescence spectra obtained by excitation at 350 *nm* of the two samples - rye flour of *Secale cereale* (SC) and sclerota powder of *Claviceps purpurea* (CP), respectively are presented. As it can be seen rye flour (SC) exhibits an emission at 425 *nm* and sclerota powder (CP) has a broad emission band between 414 *nm* and 423 *nm*. Excitation at 360 *nm* reveals emissions at 431 *nm* for SC and at 423 *nm* – 426 *nm* for CP respectively, confirming presence of lysergic acid in both samples.

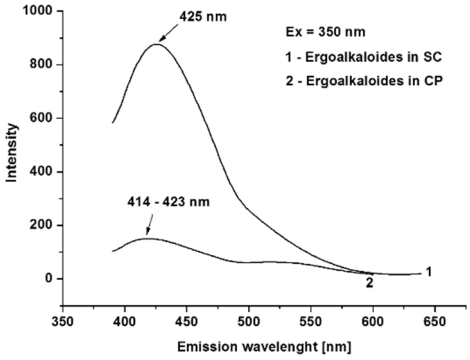

Fig. 3. Ergoalkaloides in integral rye flour, *Secalum Cereale*, and in sclerota powder of *Claviceps purpurea*

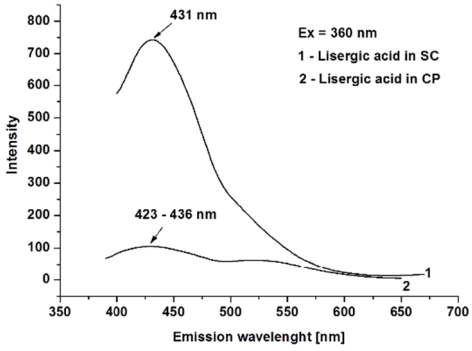

Fig. 4. Lisergic acid in integral rye flour, *Secalum Cereale*, and in sclerota powder of *Claviceps purpurea*

In the same time the growth factors, were put into evidence applying excitation wavelengths of 390 *nm* for NADPH, see Fig 5, or, respectively, of 450 *nm* for flavine, see Fig. 6. NADPH and flavine are biogenic fluorophors exhibiting emissions as follows: Em NADPH = 456 *nm* for both SC and CP, Em flavine = 507 *nm* for SC and Em flavine = 513 *nm*-516 *nm* for CP.

All these results confirmed the existence of ergoalkaloids in the two samples, as expected, and are in good agreement with literature data [7, 13].

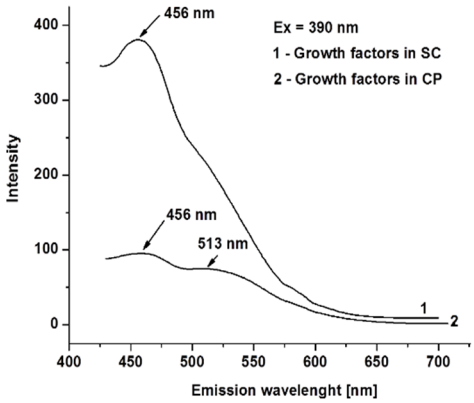

Fig. 5. Growth factors – NADPH – in integral rye flour, *Secalum Cereale*, and in sclerota powder of *Claviceps purpurea*

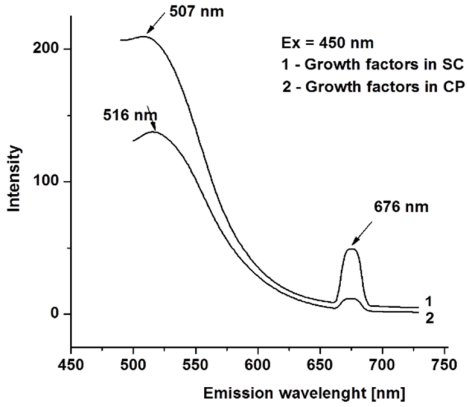

Fig. 6. Growth factors – flavine – in integral rye flour, *Secalum Cereale*, and in sclerota powder of *Claviceps purpurea*

Starches can be colorimetric identified in substances by using a solution of iodine and potassium iodide (I_2, KI). A color change from dark blue to black will occurs [14]. In Codex Alimentarius are not validated yet fluorimetric determinations [15], even if regional accepted protocols are applied. For quantitative determinations starch extracts incubated 30 min at room temperature exhibits fluorescence at 530 *nm* excitation and emission at 585 *nm*. [16]. Our experiment confirms the existence of starch, due to fluorescence emission signal at 795 *nm* excited at 530 *nm* (like in the protocol above specified). Shift of emission wavelenght from 585 *nm* to 795 *nm* can be caused by the fact that present fluorimetric identification of starch was done on solid unprocessed samples of integral rye flour, *Secalum Cereale* and of sclerota powder of *Claviceps purpurea*, respectively.

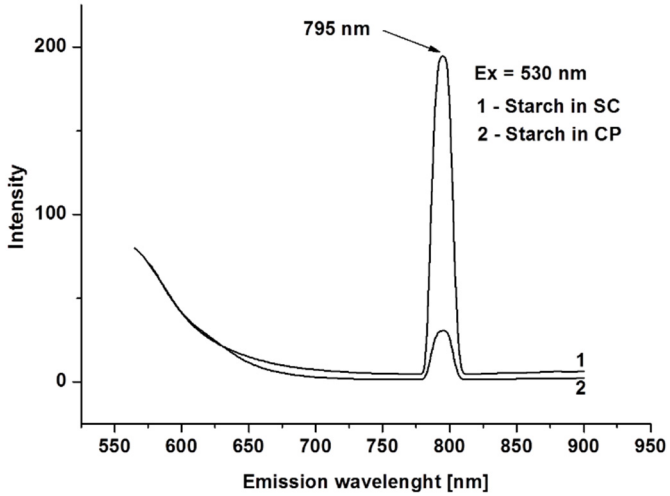

Fig. 7. Starch identification in *Secalum Cereale* (SC) integral rye flour and in sclerota powder of *Claviceps purpurea* (CP).

CONCLUSION

Qualitative identification of main constituents and alkaloids in integral rye flour, *Secalum Cereale*, and sclerota powder of *Claviceps purpurea* using spectrofluorimetry demonstrated the progress of application of above specified method in quick analysis of alkaloids. In further experiments extraction and purification of compounds of interest as well as quantitative analysis will follow, proving the efficacy and reliability of spectrofluorimetry for alkaloids quantification in food products. The fluorimetry has the advantage that the results could be read within 1–5 hours and the reproducibility was superior to other methods.

REFERENCES

1. Jan Jirschitzka, Gregor W. Schmidt, Michael Reichelt, Bernd Schneider, Jonathan Gershenzon and John C. D'Auria – "Plant tropane alkaloid biosynthesis evolved independently in the *Solanaceae* and *Erythroxylaceae"*, Proceedings of the National Academy of Sciences USA, Early Edition, June 6-th 2012, DOI: 10.1073/pnas.1200473109, *PNAS* vol **109**(26) (2012) 10304-10309.
2. Analysis of Drugs and Poisons - www.medicinescomplete.com/mc/clarke/current

3. R. Fischbach, W. Gross-Fengels, R. Schmidt. Ergotism: an occasional unrecognized cause of acute ischemia of the extremities. [German] *Rontgenblatter* **43**(5) (1990) 213-219.
4. European Commission, Official Journal of E U, EU Recommendation (2012/154/UE).
5. Scientific Working Group for the Analysis of Seized Drugs (SWGDRUG) Recommendations, UNITED STATES Department of Justice, Drug Enforcement Administration, Executive Office of the President Office of National Drug Control Policy, Counterdrug Technology Assessment Center, Washington D.C., 2011.
6. C. Mărutoiu, L. Oprean, O.F. Mărutoiu, M.L. Soran, C. Tigae, M.C. Goncea – "Quality control of commercial mustard by thin-layer chromatography", *J. Planar Chromatogr.-Mod. TLC*, **18** 104 (2005) 282-284.
7. Daniela Boehl, Dörte Solle, Bernd Hitzmann, Thomas Scheper, „Chemometric modelling with two-dimensional fluorescence data for *Claviceps purpurea* bioprocess characterization" *Journal of Biotechnology* **105** (2003) 179-188.
8. S. G. Stevenson and K. R. Preston, "Intrinsic Fluorescence and Quenching Studies of Gluten Proteins", *Cereal. Chem.* **71**(2) (1994) 155-159.
9. W. Slavin, A.T.R. Williams, R. F. Adams, "A fluorescence detector for high pressure liquid chromatography", *J. of Chromatography* **134**(1) (1977) 121-130.
10. Robert J. Flanagan, Andrew A. Taylor, Ian D. Watson, Robin Whelpton, "Fundamentals of analytical toxicology", John Wiley & Sons Ltd., 2007, London, United Kingdom.
11. A. H. Beckett, J. B. Stenlake, "Practical Pharmaceutical Chemistry, Part II, Athlone Press, 1988, London, United Kingdom.
12. European Food Safety Authority (EFSA), Parma, Italy, *EFSA Journal* **10**(7) (2012) 2798.
13. Schulmann, S., Molecular Luminescence Spectroscopy - Methods & Application,/Part 1, Chemical Analysis, vol.77. Wiley & Sons, New York, 1985.
14. Indiana Biology Standards Resource, B.1.4, B.1.6 / Curriculum Framework, 2003, USA.
15. CODEX ALIMENTARIUS, Recommended methods of analysis and sampling, *Codex stan 234-1999.*
16. www.medibena.com, E2SD001, Bioassay Systems – Starch, 2008.

STUDIA UBB PHYSICA, Vol. 61 (LXI), 1, 2016, pp. 83-91
(RECOMMENDED CITATION)

Dedicated to Professor Dr. Cozar Onuc on His 70th Anniversary

LIDOCAINE - HSA BINDING CHARACTERIZED BY FLUORESCENCE SPECTROSCOPY AND MOLECULAR DOCKING

S. NEAMTU[a], L. BUIMAGA-IARINCA[a], M. BOGDAN[a], I. TURCU[a,*]

ABSTRACT. Quenching fluorescence and molecular docking methods were used to evaluate changes in the local environment of intrinsic fluorophores of HSA in the presence of lidocaine and to calculate the binding parameters that characterize drug-protein interaction. We show that lidocaine induces significant fluorescence quenching of tryptophan and changes in conformation of IIA domain of HSA. The bimolecular quenching rate constant calculated using Stern-Volmer equation indicates a direct binding as the cause of fluorescence quenching. The protein-ligand association constant determined from Trp fluorescence quenching data showed a weak binding of lidocaine to HSA. The molecular docking calculations indicates three docking sites for lidocaine, in IIIA and IIA and IB domains of HSA, with preference for cavities located in IIIA.

Keywords: *fluorescence quenching spectroscopy; lidocaine-HSA interaction; molecular docking.*

INTRODUCTION

A fundamental characteristic of serum albumin (HSA), the most abundant protein of plasma, is the high ability to bind reversibly and to transport a large variety of drugs. HSA plasma abundance makes it an important factor in the pharmacokinetic behavior of many drugs, affecting their efficacy, toxicity and rate

[a] *National Institute for Research and Development of Isotopic and Molecular Technologies, Molecular and Biomolecular Physics Department, 65-103 Donat, 400293 Cluj-Napoca, Romania*
[*] *Corresponding author: ioan.turcu@itim-cj.ro*

of drug delivery [1]. Studies related to drugs - HSA interaction give us a better understanding about drug binding process, drug delivery, how competition equilibria could affect drug availability, metabolism and excretion rate, which are of great importance for drug pharmacology and pharmacodynamics [2]. From structural viewpoint the albumin molecule has three homologous domain (I, II and III), each containing two subdomain (A and B) stabilized by 17 disulfide bridges. Three specific drug binding sites were identified in HSA molecule: Sudlow's sites located in subdomain IIA (drug site I) and in subdomain IIIA (drug site II) and recently, subdomain IB which was defined as the third major drug binding region of HSA, based on circular dichroism spectroscopic approach [3].

Lidocaine is a local anesthetic used in antiarrhythmic medication that works by blocking sodium channels. Studies concerning lidocaine binding to HSA are related mainly to equilibrium dialysis, crystallographic analysis [4, 5] and to a homogenous enzyme immunoassay [6]. Based on crystallographic data, Hein et al. [5] assert that lidocaine has a unique binding site located in the subdomain IB of HSA and that tryptophan residue (Trp 214) is not directly involved in lidocaine binding; but the structural features at the residue could be modified as a result of the lidocaine binding. Additionally, fluorescence experiments put in evidence HSA fluorescence quenching and a blue shift of the spectra that suggests lidocaine-induced conformational changes in the Trp environment.

In the present report we used two complementary and alternative methods for investigation and characterization of HSA – lidocaine interaction: fluorescence spectroscopy and molecular docking. Our goal was to identify the binding sites of lidocaine and to quantitatively characterize the binding affinity.

METHODS

Fluorescence quenching spectroscopy

Fluorescence quenching is a phenomenon where the light emitted by a fluorophore is diminished by the action of ligand. The phenomenon depends on the availability of HSA fluorophores (tryptophan and tyrosine) to the ligand. Trp-214 residue is the main intrinsic fluorophore of human albumin located in drug site I of IIA subdomain and its fluorescence quenching was used to find the lidocaine-HSA binding parameters. Using a synchronous fluorescence method to record the emission spectra of Trp we were able to provide additional information about the molecular environment in the vicinity of HSA intrinsic fluorophores.

The analysis of the experimental data based on Stern-Volmer equation (Eq 1) allows us to identify the nature of the interaction between protein and ligand and respectively between a process of dynamic collisional interaction and a process based on the formation of molecular complexes:

$$\frac{F_0}{F} = 1 + k_q \tau_0 [Q] = 1 + K_{SV}[Q] \quad (1),$$

where F_0 and F are the fluorescence emission intensity of HSA without and with the addition of a known concentration of quencher [Q], K_{SV} is the Stern-Volmer quenching constant, k_q is the bimolecular quenching rate constant, and τ_0 is the fluorescence lifetime of the unquenched fluorophore. k_q has a great importance because it is directly related to the sterical and electrical availability of fluorophore. As the fluorophore is more exposed, the fluorescence quenching efficiency (measured by k_q) is higher. For a collisional process, k_q cannot be larger than $2x10^{10}$ $M^{-1}s^{-1}$ [7].

In order to determine the association constant of protein-ligand complex, the experimental data have been fitted with the function proposed by M. van de Weert [8] which assumes a 1:1 stoichiometry and in normalized version can be expressed as:

$$\frac{F_{corr}}{F_0} = 1 + \left(\frac{F_c}{F_0} - 1\right) \frac{[P]_t + [Q]_a + K_d - \sqrt{([P]_t + [Q]_a + K_d)^2 - 4[P]_t[Q]_a}}{2[P]_t} \quad (2)$$

where F_{corr} is the measured fluorescence corrected for the inner-filter effect, F_0 is the fluorescence in the absence of lidocaine, F_c is the fluorescence of the fully complexed HSA, K_d is the dissociation constant, $[P]_t$ is the concentration of HSA, and $[Q]_a$ is the concentration of added lidocaine.

The inner-filter effect corrections were done according to the formula:

$$F_{corr} = F_{obs} 10^{\frac{A_{exc} + A_{em}}{2}} \quad (3)$$

where F_{corr} is the corrected fluorescence value, F_{obs} the measured fluorescence value, A_{exc} and A_{em} the measured absorbance values at the excitation and emission wavelengths, respectively.

Molecular docking simulations

Crystallographic data for albumin were downloaded from RCSB PDB website [http://www.rcsb.org/pdb/explore/explore.do?structureId = 1AO6]. The data for lidocaine molecule used as ligand in this study was downloaded from [https://pubchem.ncbi.nlm.nih.gov/compound/lidocaine] NCBI Chemistry website. The

optimized 3D structures of molecules were obtained with Gaussian09. AutoDockTools was used to build the input files (ligand + HSA) [http://autodock.scripps.edu/resources/adt] while the docking calculations were performed by using AutodockVina [http: //autodock.scripps.edu] [9] (open source). Viewing the results and some structure calculations were performed with VMD software [http://www.ks.uiuc.edu/Research/vmd/] and with Chimera1.9 [https://www.cgl.ucsf.edu/chimera/].

VINA code combines two methods, Monte Carlo and Simulated Annealing respectively, into a Lamarkian genetic algorithm LGA. It takes into account a temperature of 298.15 K performing 10 independent runs and starting with 150 random conformations. The calculation involves a random conformation disturbance and a local optimization (algorithm Broyden-Fletcher-Goldfarb-Shanno) followed by and an assessment in which the result is accepted or not. Each local optimization involves several evaluations of the scoring function and of its coordinates in term of position-orientation-twist. The number of optimization steps is heuristically determined, depending on the size and flexibility of the ligand. Each simulation may produce more results, automatically grouped and sorted to produce the final result. The code output results in nine possible locations for docking. To clearly indicate the binding sites of lidocaine in HSA we thus calculated 100 possible locations by using a 126x126x126 Å region with a grid of 0.375 Å. All the calculations were made by explicitly taking into account the polar hydrogens of HSA and by treating the ligand as flexible.

EXPERIMENTAL

Chemicals

Serum albumin, fraction V (fatty acid free, 99%) was purchased from Sigma – Aldrich Chemie GmbH. Lidocaine hydrochloride was achieved as 40 mg/ml sterile isotonic saline solution. All other reagents used were of analytical grade and double distilled water was used throughout the experiments.

Fluorescence measurements

The fluorescence spectra were measured at room temperature on a JASCO – 6500 spectrofluorimeter equipped with a Xenon lamp and 1.0 cm quartz cell. The HSA fluorescence emission spectra were recorded in the wavelength range of 300 – 500 nm, upon excitation at λ_{ex} = 295 nm. Synchronous fluorescence measurements were used to put in evidence the influence of lidocaine at the level of HSA intrinsic fluorophores,

tyrosine (Tyr) and tryptophan (Trp). The emission spectra were recorded in the wavelength range 280-340 nm upon excitation shifted with $\Delta\lambda_{tyr}$ = 30 nm for Tyr and in the range 310-380 nm with $\Delta\lambda_{trp}$ = 60 nm for Trp.

The UV-vis absorption spectra were recorded on a double beam JASCO–550 spectrophotometer equipped with 1.0 cm quartz cell, in the range of 250 – 500 nm.

Solutions were prepared at room temperature using double distilled water and 50 mM Tris/HCl (pH 7.4) as buffer. The HSA concentration was kept fixed at 4 μM and the lidocaine concentration was varied from 0 to 20 mM (2, 4, 6, 8, 10, 15, 20 mM).

RESULTS AND DISCUSSION

Tryptophan fluorescence quenching by lidocaine

Fig. 1 illustrate changes in the emission spectra of HSA fluorescence at 295 nm excitation wavelength and Fig. 2 the fluorescence spectra of tyrosine and tryptophan in the presence of lidocaine, obtained by synchronous fluorescence measurements. When the concentration of albumin were fixed at 4μM and lidocaine concentration was gradually increased, HSA and Trp fluorescence emission intensity decreased significantly and is accompanied by a maximum shift that suggests conformation changes of HSA molecule.

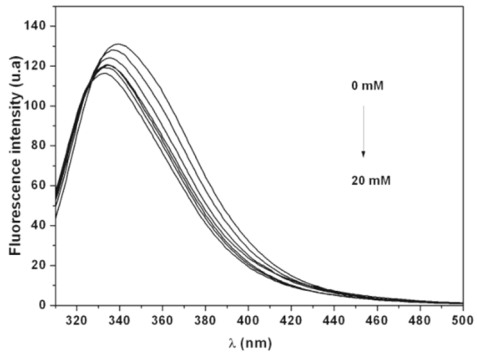

Fig. 1. Fluorescence emission spectra of HSA 4 μM, in the presence of lidocaine in the range of 2-20 mM
λ_{ex} = 295 nm

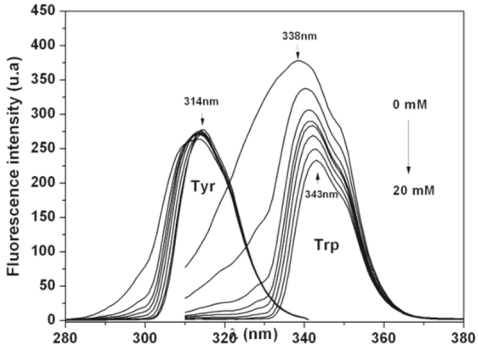

Fig. 2. The synchronous fluorescence spectra of tyrosine (Tyr) and tryptophan (Trp) in the presence of 0 – 20 mM lidocaine concentrations

Synchronous fluorescence measurements (Fig. 2) showed a reduction in the tyrosine emission spectra area with increasing lidocaine concentration but no fluorescence quenching.

Besides a significant quenching of Trp fluorescence, a 5 nm red shift of spectra maximum is observed which corresponds to changes of the polarity around the chromophore molecule. According to the accepted interpretation of changes in polarity of chromophore neighborhood [10], the red shift of Trp λ_{max} suggests a more polar environment for tryptophan residue as a result of HSA lidocaine interaction. The shift of the maximum intensity in the case of tyrosine was insignificant, reflecting little transformation around this fluorophore.

As can be seen from Stern-Volmer curve (Fig. 3), the plot of F_0/F_{corr} versus lidocaine concentration [Q] exhibits a good linearity (R = 0.8986). The values obtained for K_{SV} and k_q parameters were: K_{SV} = (2.31±0.088) x 10^5 M^{-1} and k_q= 3.3 x 10^{13} $M^{-1}s^{-1}$, using a typical HSA average lifetime without quencher of 7 ns [11].

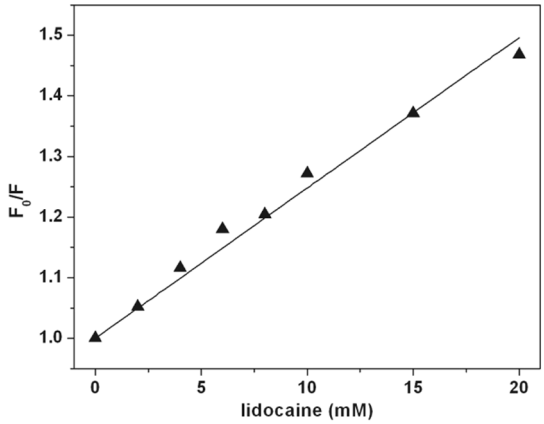

Fig. 3. The Stern-Volmer curve for lidocaine quenching fluorescence of tryptophan

The calculated bimolecular quenching constant (k_q) is too large to be consistent with collisional quenching (>2x10^{10} $M^{-1}s^{-1}$) indicating that a binding event is the most likely cause of quenching.

Binding constant of lidocaine-HSA molecular complex

The dissociation constant K_d of drug-protein complex was determined from the decrease of Trp fluorescence intensity with the lidocaine concentration (Fig. 4) using the fitting function given by Ec. (2). The determined value was K_d = 1.51 x 10^{-2} M, corresponding to an association constant K_a = 0.66 x 10^2 M^{-1}. The small value of the binding constant reveals a weak lidocaine-HSA interaction, in agreement with equilibrium dialysis data (0.5 – 5 x 10^2 M^{-1}) previously reported [4,5,6].

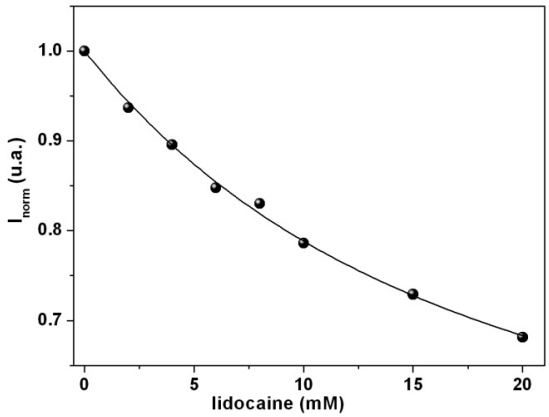

Fig. 4. Fitted curves of Trp fluorescence quenched by lidocaine

Molecular docking analysis of lidocaine – HSA binding

An alternative way to investigate lidocaine - HSA binding is by molecular docking calculations which besides the binding sites give also a qualitative assessment of the molecular interaction in terms of binding energy. The calculated energies of lidocaine - HSA interaction for 100 potential docking locations varies between - 6.7 kcal mol^{-1} (- 0.3 eV) and - 4.6 kcal mol^{-1} (- 0.2 eV). The energy difference between the conformers with the strongest and the smallest docking energy is only 1.61 kcal mol^{-1} (0.07eV). All these interaction energies are very small, indicating no chemical interaction. We may suppose that the lidocaine binds with HSA by weak physisorption, probably due to van der Waals interactions. Moreover, energy difference of about 1.6 kcal mol^{-1} (0.07 eV) between lidocaine conformers indicate that the molecule suffer no major deformations, another hint of relatively weak interaction with HSA.

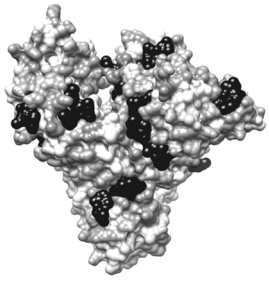

Fig. 5. 3D representation of HSA with binding sites depending on the likelihood of lidocaine docking.

Fig. 6. Preferential binding sites of lidocaine in HSA molecule.

In terms of binding sites, the molecular docking also returns interesting results. We may see in Fig. 5 that lidocaine is able to dock in many region of HSA. It only seems to prefer the hydrophobic cavities.

A closer analysis revealed that lidocaine have three preferential docking locations placed in the segment IIIA, IIA and IB of HSA molecule (Fig. 6). The binding probabilities in each site are 18%, 15 % and 13% respectively. A detailed image is presented in Fig. 7a and b, where we may see the lidocaine molecule and its vicinity in segments IIA and IIIA.

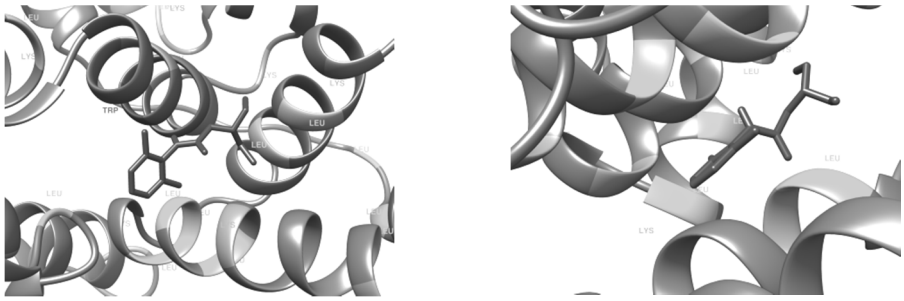

Fig. 7. Detail image of the lidocaine interaction with albumin.

We see that no direct interaction occurs between tryptophan and lidocaine, although they are quite close. In both segments IIA and IIIA the lidocaine is mainly surrounded by leucine and lysine.

CONCLUSIONS

Theoretical investigations based on molecular docking calculations points out three docking sites for lidocaine, located in IIIA, IIA and IB domains of HSA molecule, with highest affinity for the IIIA domain. This first result is in agreement with the three-site model of drug-HSA binding proposed recently in the literature [3]. Besides these particular sites there are many others with a very low binding affinity spread all around the HSA molecule surface. The binding energies obtained by docking calculations are relatively small indicating a weak physisorption mechanism, probably due to van der Waals interactions.

By fluorescence quenching spectroscopy applied on Trp 214 fluorophore we are able to find an association constant $K_a = 0.66 \times 10^2\ M^{-1}$ for lidocaine - HSA binding. This value characterizes in a quantitative manner the binding affinity of lidocaine to IIA domain which hosts the single tryptophan residue of the HSA molecule. The weak

interaction between lidocaine and the IIA domain of HSA signify that this binding site is only a minor carrier for this drug molecule. Additionally we were able to put into evidence conformational changes in the Trp 214 neighborhood as a result of lidocaine-HSA binding.

Previously reported values for the binding constant, determined from equilibrium dialysis (3.1×10^2 M^{-1}) [5] and homogeneous enzyme immunoassay (5.1×10^2 M^{-1}) [6] are several times higher as compared to the value obtained by us. The most probable explanation is that the above mentioned techniques are global methods taking into account all the binding sites of the HSA molecules.

As a final conclusion we emphasize that for a thoroughly characterization of the lidocaine-HAS association one need several complementary investigation techniques able to capture the complexity of the binding process.

ACKNOWLEDGMENTS

This work was financially supported by ANCS Romania, Project PN 09-4402 13.

REFERENCES

[1] M. Fasano1, S. Curry, E. Terreno, M. Galliano, G. Fanali, P. Narciso, S. Notari and P. Ascenzi, *IUBMB Life*, 57(12), 787 (2005).
[2] T Peters, "All about Albumin: Biochemistry, Genetics, and Medical Applications" Academic Press: San Diego, CA, USA, 1996.
[3] F. Zsila, *Mol. Pharmaceutics*, 10 (5), 1668 (2013).
[4] E. Krauss, C. F. Polnaszek, D. A. Scheeler, H. B. Halsall, J. H. Eckfeldt, J. L. Holtzman, J. *Pharmacol. Exp. Ther*., 239, 754 (1986).
[5] K. L. Hein, U. Kragh-Hansen, J. P. Morth, M. D. Jeppesen, D. Otzen, J. V. Møller, P. Nissen, *J. Struct. Biol.,* 171, 353 (2010).
[6] D. N. Bailey, J. R. Briggs, *Ther. Drug. Monit*., 26, 40 (2004).
[7] J. R. Lakowicz, "Principles of Fluorescence Spectroscopy", 3rd ed., Springer, New York**.** 2006.
[8] M. van de Weert, L. Stella, *J. Mol. Struct*., 998, 144 (2011).
[9] O. Trott, A. J. Olson, *J. Comput. Chem.*, 31, 455 (2010).
[10] J. N. Miller, *Proc. Anal. Div. Chem. Soc.,* 16, 203 (1979).
[11] M. Amiri, K. Jankeje, J. R. Albani, *J. Fluoresc*. 20m 651 (2010).

STUDIA UBB PHYSICA, Vol. 61 (LXI), 1, 2016, pp. 93-98
(RECOMMENDED CITATION)

Dedicated to Professor Dr. Cozar Onuc on His 70th Anniversary

Fe_2O_3 PARTICLES AS PRECURSORS FOR α''-$Fe_{16}N_2$ PHASE SYNTHESIS

R. A. ONE[a], R. BORTNIC[a], S. MICAN[a,*], L. BARBU-TUDORAN[b], V. POP[a]

ABSTRACT. In this work we investigate the structural properties and microstructure of Fe_2O_3 particles synthesized using the sol-gel method. Differential thermal and thermogravimetric analysis showed that the organic matrix is completely burned off at temperatures higher than 520 °C. The sample annealed at 550 °C for 12 h contained only the Fe_2O_3 phase. The obtained hematite particles are micrometer sized and have an elongated shape. Taking into account the cheap and available sol-gel precursors, the possibility of using these particles in α''-$Fe_{16}N_2$ synthesis is discussed.

Keywords: *Hematite, Sol-gel synthesis, Shape anisotropy, X-ray Diffraction, Calorimetry, Annealing.*

INTRODUCTION

In the last 20 years an increased interest for rare earth free magnetic materials has been observed [1]. The recent rare earth crisis has led to the opening of various research directions for studying rare earth free magnetic materials and since then many alloys, compounds and synthesis pathways have been investigated [2-4]. A promising alternative to rare earth-based magnets is the α''-$Fe_{16}N_2$ phase which presents enhanced magnetic properties compared to those of α-Fe [5]. Different synthesis techniques for obtaining the α''-$Fe_{16}N_2$ phase have been reported, however, they faced difficulties regarding phase purity and expected properties [5-9]. One of the main difficulties in obtaining the α''-$Fe_{16}N_2$ phase is its low decomposition temperature, around 200 °C [10].

[a] *Babeş-Bolyai University, Faculty of Physics, 1 M. Kogălniceanu, 400084 Cluj-Napoca, Romania.*

[b] *National Institute for R&D of Isotopic and Molecular Technologies, 75-103 Donath, 400293, Cluj-Napoca, Romania.*

[*] *Corresponding author: sever.mican@phys.ubbcluj.ro*

The α”-$Fe_{16}N_2$ phase synthesis method with the highest yield proposes the nitridation of metallic iron under anhydrous ammonia at low temperatures [11, 12]. The metallic iron is usually obtained from iron oxides by reduction under hydrogen at temperatures around 400-500 °C [11]. It was reported that the Fe particle size strongly affects the yield of α”-$Fe_{16}N_2$ phase formation during the nitridation reaction, smaller particles leading to higher α”-$Fe_{16}N_2$ phase concentrations [11]. In this work we investigate the crystal structure and microstructure of Fe_2O_3 powders synthesized using the sol-gel method. Fine Fe_2O_3 powders with nanometer-size particles and various microstructures can be obtained using the sol-gel process [13], which could then be used as starting materials for preparing $Fe_{16}N_2$. The possibility of using these particles as precursors for synthesizing α”-$Fe_{16}N_2$ magnetic materials is discussed.

EXPERIMENTAL DETAILS

The hematite particles were obtained via the sol-gel combustion method. Iron chloride hexahydrate ($FeCl_3 \cdot 6H_2O$) was used as an iron source. Pectin and sucrose were added as polycondensation, respectively gelation agents, in order to prevent Fe_2O_3 particle growth during the gel combustion. The mixture was stirred vigorously for 25 minutes. The sol was dried for 48 h at 90 °C in a sand bath in open air. The dried gel was annealed at 550 °C for 12 h in air. Differential thermal analysis (DTA) and thermogravimetric analysis (TGA) measurements were performed in air using a Q600 SDT thermal analyzer made by TA instruments. The heating rate during the DSC/TGA measurements was 20 °C/min. SEM images were collected using a Hitachi SU8230 scanning electron microscope. X-ray diffraction (XRD) measurements were performed at room temperature using a Bruker D8 Advance diffractometer using Bragg-Brentano focusing geometry and Cu Kα radiation. The lattice parameters were determined using the Powdercell software.

RESULTS AND DISCUSSIONS

The X-ray diffraction patterns of the dried gel and the sample annealed at 550 °C for 12 h in air are shown in Figure 1. The as-obtained dried gel shows a diffraction pattern which is characteristic for amorphous materials, consisting of a background signal of decreasing intensity with increasing 2θ angle. This behaviour could be attributed to the organic part bonded with the iron oxide in the gel which prevents the crystalline ordering of the iron oxide.

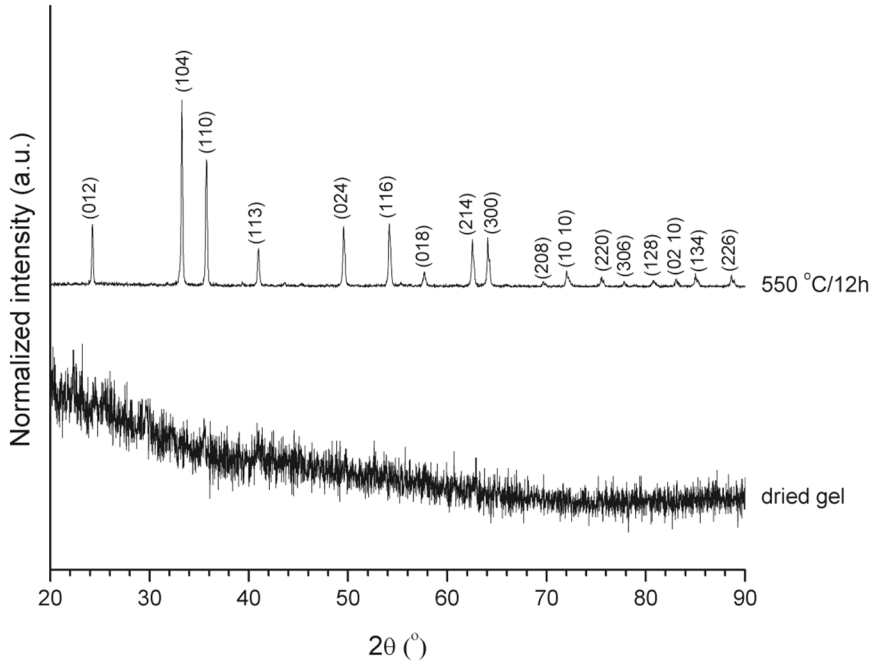

Fig. 1. X-ray diffraction patterns of the as-obtained dried gel and the sample annealed at 550 °C for 12 hours in air. The miller indices of the Fe_2O_3 phase are indicated on top of their respective peaks.

To find out about the optimum annealing temperature, in order to burn the organic part of the dried gel, we performed a simultaneous differential thermal analysis (DTA) and thermogravimetric analysis (TGA) measurement from room temperature up to 1000 °C. The DSC/TGA curves are shown in Figure 2. The DTA curve shows one broad peak centered on 250 °C, an intense peak at 460 °C and a small shoulder around 520 °C. The TGA derivative versus temperature curve showed one narrow peak at 200 °C with a shoulder around 250 °C and an intense peak at 460 °C with a small shoulder at 520 °C. The peaks at 200 and 250 °C correspond to the elimination of water from the gel structure, accounting for a weight loss of around 40% - Figure 2 inset. The peaks at 460 and 520 °C were attributed to the burning of the organic part of the gel, the sample mass decreasing from 60% to around 10% of the initial mass. The TGA signal remains constant from 550 °C to 1000 °C, meaning that the burning of the organic part was complete after 520 °C.

To ensure the complete elimination of the organic part we chose to anneal the gel at 550 °C for 12 h in air. The X-ray diffraction pattern of the annealed gel - Figure 1 - shows that the sample is single phase, consisting of hematite (Fe_2O_3).

The lattice parameters of the obtained Fe_2O_3 phase are a = 5.03 Å and c = 13.77 Å, in good agreement with previously reported data [14]. The XRD peaks of the annealed sample are intense and narrow, indicating micrometer size crystallites.

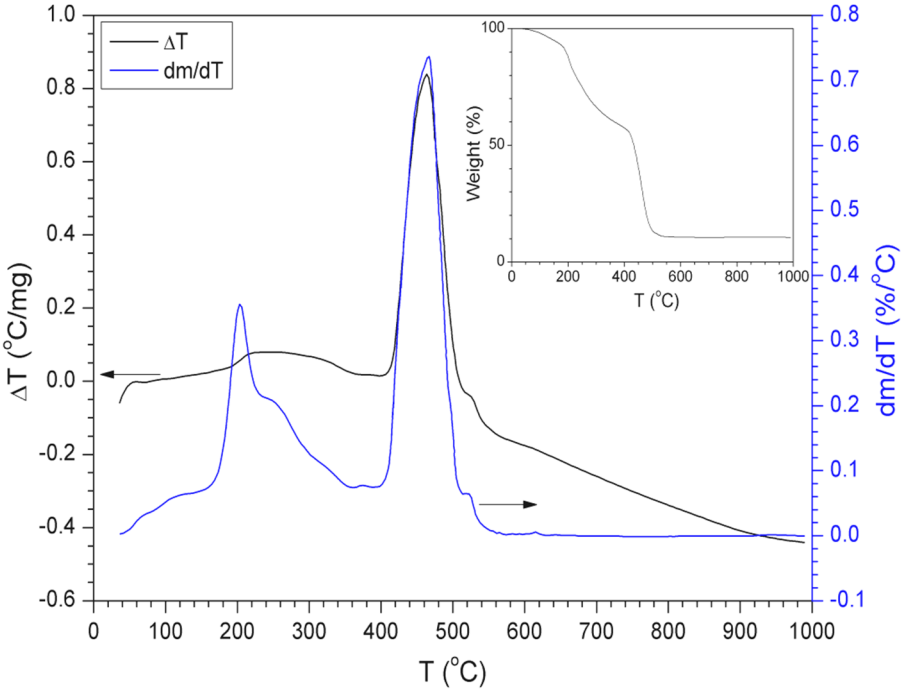

Fig. 2. DTA/TGA curves of the dried gel sample. The main figure shows the DTA signal and the derivative of the TGA signal as a function of temperature. The TGA signal is shown in the inset.

In order to study the morphology and microstructure of the as-obtained dried gel and annealed samples, we performed scanning electron microscopy (SEM) measurements on the two samples. The collected SEM images are shown in Figure 3. The as-obtained dry gel consists of elongated particles with sizes of the order of 10-100 nm - Figure 3 (a, b) - a characteristic of materials synthesized through the sol-gel method. However, after annealing the dry gel at 550 °C for 12 h in air, the SEM images show that the sample is comprised of micrometer size particles with elongated shapes and a rather narrow size distribution - Figure 3 (c, d). This behaviour could be explained by the fact that as the organic part is burned off, iron oxide particles start to crystallize. The fact that the particles are micrometer size could mean that the annealing time was too long. Shorter annealing times could lead to smaller particle

sizes within the 50-100 nanometer range, which are optimum for α"-$Fe_{16}N_2$ synthesis [11]. The elongated shape of the hematite particles makes them promising precursors for synthesizing α"-$Fe_{16}N_2$ magnetic materials with shape anisotropy.

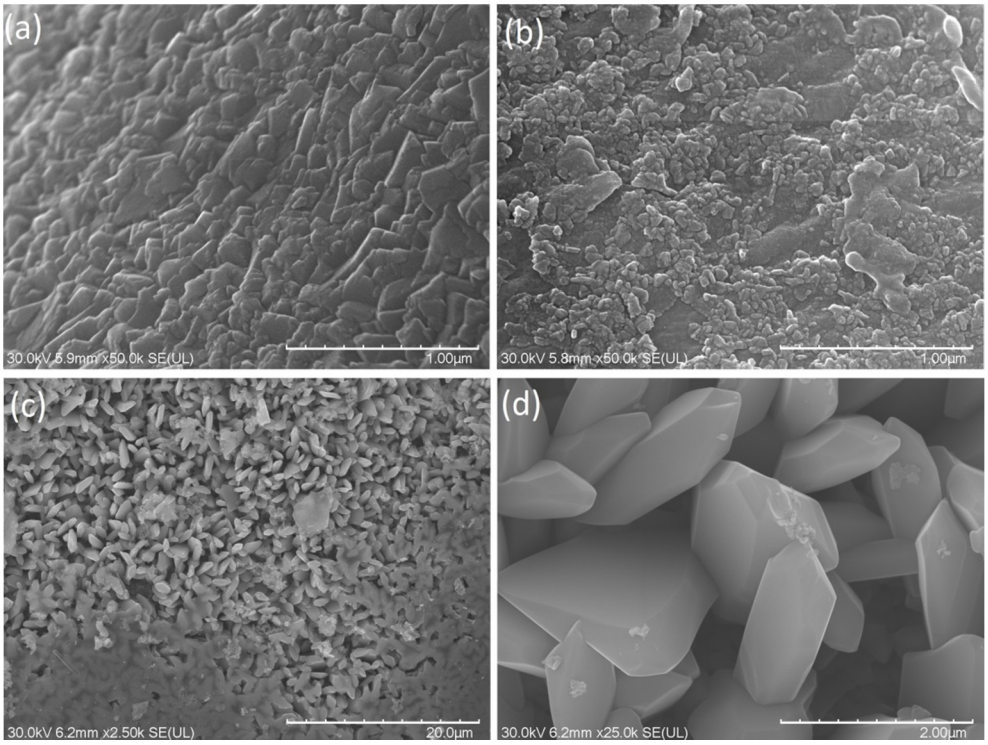

Fig. 3. SEM images of the as-obtained dry gel (a, b) and the sample annealed at 550 °C for 12 h in air (c, d).

CONCLUSIONS

The structure and microstructure of Fe_2O_3 particles synthesized by the sol-gel method were investigated. The X-ray diffraction pattern of the as-obtained dried gel showed that the sample was amorphous, characteristic for materials obtained using the sol-gel method. DTA/TGA measurements showed that the organic matrix of the gel is completely burned off at temperatures above 520 °C. The sample annealed at 550 °C for 12 h in air was found to be single phase, consisting of micrometer size Fe_2O_3 particles with an elongated shape and a rather

narrow size distribution. These results showed that the sol-gel technique can be used to synthesize particles with different geometries, making them suitable for magnetic materials preparation with induced shape anisotropy. The cheap and available precursors also make this method promising for large-scale synthesis of acicular Fe_2O_3 particles and consequently α"-$Fe_{16}N_2$ magnetic materials with enhanced shape anisotropy.

ACKNOWLEDGMENTS

The authors would like to acknowledge support from the Romanian Ministry of Education and Research, Grant PN-II-PT-PCCA-2013-4-0971.

REFERENCES

[1] D. Li, D. Pan, S. Li, Z. Zhang, *Sci. China-Phys. Mech. Astron.*, 59, 1-17 (2016).
[2] A. Makino, P. Sharma, K. Sato, A. Takeuchi, Y. Zhang, K. Takenaka, *Nat. Sci. Reports*, 5, 16627 (2015).
[3] S. Mican, D. Benea, R. Hirian, R. Gavrea, O. Isnard, V. Pop, M. Coldea, *J. Magn. Magn. Mater.*, 401, 841-847 (2016).
[4] J.M. D. Coey, *J. Appl. Phys.* 76, 6632 (1994).
[5] T.K. Kim, M. Takahashi, *Appl. Phys. Lett.* 20, 492 (1977).
[6] K.H. Jack, *Proc. R. Soc. A*, 208, 200 (1951).
[7] X. Wang et al, *Appl. Surf. Sci.*, 220, 30-29 (2003).
[8] T. Ogawa, Y. Ogata, R. Gallage, N. Kobayashi, N. Hayashi, Y. Kusano, S. Yamamoto, K. Kohara, M. Doi, M. Takano, M. Takahashi, *Appl. Phys. Express*, 6, 073007 (2013).
[9] T. Ogi, A. B. D. Nandiyanto, Y. Kisakibaru, T. Iwaki, K. Nakamura K. Okuyama, *J. App. Phys.,* 113, 164301 (2013).
[10] S. Yamamoto, R. Gallage, Y. Ogata, Y. Kusano, N. Kobayashi, T. Ogawa, N. Hayashi, Kaori Kohara, M. Takahashi, M. Takanoa, *Chem. Commun.*, 49, 7708-7710 (2013).
[11] S. Kikkawa, K. Kubota, T. Takeda, *J. Alloy. Compd.,* 449, 7-10 (2008).
[12] S. Kikkawa, A. Yamada, Y. Masubuchi, T. Takeda, *Mater. Res. Bull.,* 43, 3352-3357 (2008).
[13] K. Rath, *Science and Technology Review*, 24-26, May 2005.
[14] R. L. Blake, R. E. Hessevick, *Am. Mineral.*, 51, 123-129 (1966).

STUDIA UBB PHYSICA, Vol. 61 (LXI), 1, 2016, pp. 99-108
(RECOMMENDED CITATION)

Dedicated to Professor Dr. Cozar Onuc on His 70th Anniversary

CYANOBACTERIA DETECTION AND RAMAN SPECTROSCOPY CHARACTERIZATION WITH A HIGHLY SENSITIVE, HIGH RESOLUTION FIBER OPTIC PORTABLE RAMAN SYSTEM

SIMONA CINTA PINZARU[a*], CSILLA MÜLLER[a], IOANA BREZESTEAN[a], DANIEL BARCHEWITS[b], BRANKO GLAMUZINA[c]

ABSTRACT. Raman spectroscopy of cultivated Synechocystis sp. AICB 51 strain cyanobacteria is reported both at single cell level and in bulk solution. Two types of equipment, a lab-based Raman system and a portable, high resolution fiber optic Raman system respectively, were employed, to characterize the bacteria and to assess the capability of the portable instrument to reproduce the lab results for environmental application purpose. Additional cyanobacteria isolated from the Adriatic Sea, probably Synechococcus (not yet genetically identified) was employed for Raman spectroscopy characterization. Both cyanobacteria strains showed characteristic bands at 1516, 1156 and 1006 cm^{-1}, consistent with the three main Raman modes of beta-carotene in protein-carotenoid-complex from cyanobacteria, slightly different from those of pure beta-carotene. The portable system showed additional performance in recording higher signal to noise ratio in a faster and flexible way. A photoprotective energy dissipating mechanism involved upon laser exposure could be responsible for the similar Raman output of the two strains.

Keywords: *cyanobacteria, Raman spectroscopy, portable Raman system, carotenoids.*

[a] *Department of Biomolecular Physics, Babes-Bolyai University, Kogalniceanu 1, RO-400084, Cluj-Napoca, Romania.*
[b] *B&W Tek Europe GmbH, Seelandstraße 14-16, 23569 Lübeck, Germany.*
[c] *Department of Aquaculture, University of Dubrovnik, Ćira Carića 4, 20000 Dubrovnik, Croatia.*
[*] *Corresponding author: simona.cinta@phys.ubbcluj.ro*

INTRODUCTION

Cyanobacteria are among the widest spread microorganisms worldwide and their capability to adapt, survive in extreme conditions and fabricate the building blocks of the organic world within the photosynthetic process, still attach large interest for the nanotechnology-based sensing of environmental conditions as well as on their response to the environmental changes. Detection of cyanobacteria is of crucial importance in understanding microbial world and cyanobacteria research evolved in a broad area of biomedical, environmental or terrestrial and extraterrestrial applications [1-3]. Here we describe the Raman spectroscopy detection of cyanobacteria using a portable, high resolution fiber optic Raman system. Further, we demonstrate the unique capability of the Raman spectroscopy with portable instruments to promptly assess the carotenoid species in the cultivated batches of microorganisms when the 532 nm line is pre-resonantly used.

Anticipating that portable Raman mini-spectrometers could be part of a suite of analytical instrumentation in the forthcoming environmental monitoring programs or submersible and extraterrestrial missions, it is critically important to examine the spectral information that could be acquired with portable instruments from attempts to determine key molecular signatures of microorganisms under various (hostile) conditions or in real world environmental samples. Furthermore, the exploration of the Raman signature of various cyanobacteria strains poses a double aim: to understand their behavior when microorganisms are exposed specific conditions and to achieve the enhanced capability of detection in real world samples. Although abundant data are available on microbial pigments [3], it is surprisingly to note that limited information or applications are available to date on these aspects raised above.

EXPERIMENTAL

Cyanobacteria. A batch sample of cyanobacteria (Synechocystis sp. AICB 51 strain) was kindly provided by Professor N. Dragos from Biology Department of Babes-Bolyai University. The genus is a mesophilic cyanobacterium able to use the inorganic carbon added to the growth medium (Zarrouk) [4] as $NaHCO_3$. The sample was taken before the exponential grow phase and the cells density was estimated as about 0.5 $x10^5$ cells/ml from the optical density measurements. Cyanobacteria growing conditions as well as the chemical composition are described in details elsewhere [5, 6]. The genus was found strongly dependent on the temperature,

with optimal growing condition at 30°C, in fluorescent light with 630 $\mu mol \cdot m^{-2} \cdot s^{-1}$ irradiance. A specific growth rate of 0.8 $days^{-1}$ and a doubling time of 1.2 days was concluded at optimal temperature. An additional genus of cyanobacteria (most likely Synechococcus sp. in a mixed culture, strain not yet genetically identified) was isolated from open waters of South Adriatic Sea. A small batch sample of about 20 ml was available courtesy of Eng. biologist Dr. Stijepo Ljubimir, from Institute for Marine and Coastal Research, University of Dubrovnik, Croatia.

Equipment. A Renishaw InVia confocal Raman system equipped with a video camera was used for high resolution (0.5 cm^{-1}) Raman spectra acquisition and micrographs collection. A diode pumped solid state (DPSS) air cooled laser operating at 532 nm line was used for pre-resonant excitation of the cyanobacteria, with 15 s integration time, 6 acquisitions and 5% output power (10 mW).

A portable, i-Raman Plus spectrometer from B&W TEK [7] was employed for the fast assessment of the real world samples of salty waters as well as the cultivated batches. The instruments provide both the 532 and 785 nm line for excitation and the adaptability to a microscope and a fiber optic probe. The *BAC102 Raman Trigger Probe* offers a trigger function which is designed for versatility in reaching samples with difficult accessibility.

RESULTS AND DISCUSSIONS

Typical Raman signal recorded with the lab-based Raman system of the bulk cyanobacteria is shown in the Fig. 1a) in comparison with the FT-Raman signal of powder beta-carotene [8]. The beta-carotene spectrum characterization and vibrational analysis was provided elsewhere [8]. A detail of the ν_1 mode of the polyene chain centered at 1512 cm^{-1} and assigned to the conjugated C=C bond is showed in the Fig. 1b), where the corresponding band of cyanobacteria appeared shifted to 1516 cm^{-1} and considerably broadened. Tschirner et al [9, 10] shown that the prominent peak at ca. 1525 cm^{-1} of beta-carotene in solutions is composed of two closely spaced modes, both of which dominated by C=C stretching coordinates of the polyene chain, and this is an intrinsic characteristic of the molecule. Therefore, the observation of the main carotenoid band at 1522 cm^{-1} at single cell level, does not necessarily reveal a different carotenoid compound. Micrograph (20 x objective) of the Synechocystis collected with the Raman microscope from the drop coated depositions of cyanobacteria culture on a hydrophobic slide is showed in the Fig. 1c and their optical microscopy image obtained with an inversed microscope (100x objective) is showed in the Fig. 1 d.

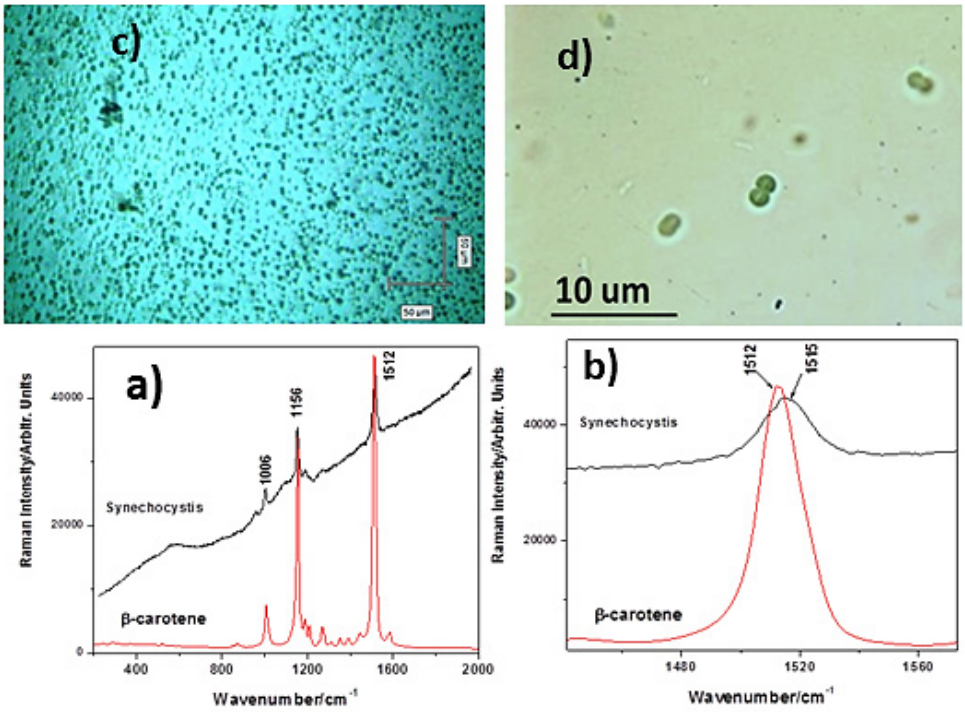

Fig. 1. Raman signal collected with a lab-based instrument (InVia, Renishaw) with 15 sec integration time from Synechocystis cyanobacteria (bulk) compared to the FT-Raman spectrum of beta-carotene powder a); detail of the v_1 Raman mode b); micrograph of the cyanobacteria seen through the Raman microscope (20x objective) c) and through an inversed optical microscope (100x objective), d).

Live cells from both cyanobacteria cultures were further characterized by Raman micro-spectroscopy with a lab-based high resolution instrument. Video-camera of the system allowed the visualization of their motility before complete aqueous medium evaporation. Wetting again the completely dried strain resulted after drop coating deposition on the hydrophobic slide with distilled water, resulted in restarting cell gliding and/or rolling motility, confirming their live status. The measured cyanobacteria were optically inspected before and after careful laser exposure and showed intact image. Raw micro-Raman spectra and their corresponding background subtracted signals are showed in the Fig. 2.

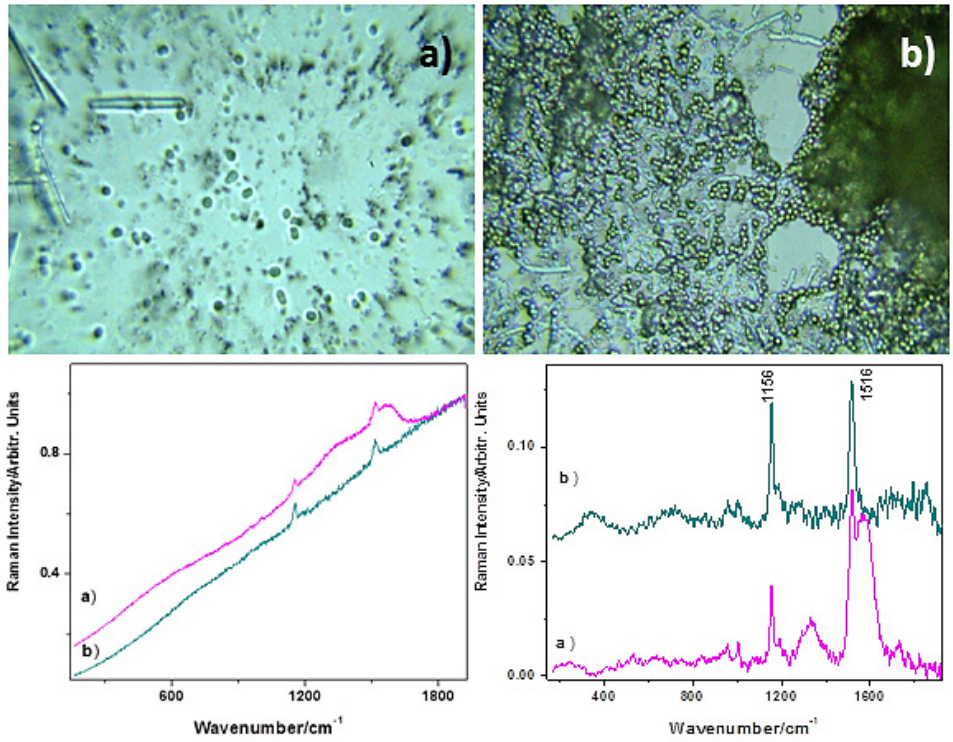

Fig. 2. Normal Raman spectra collected from the *in vivo* cyanobacteria single cells deposited on a hydrophobic slide: a) Synechocystis, b) Synnechococcus. The spectra were normalized by total integration time. Excitation: 532 nm. Laser power 1 mW. Left: raw signal; right: background subtracted. Y offset was applied for clarity. Excitation: 532 nm, 1mW. The corresponding optical microscopy images (50x objective) of the bacteria are showed in the top.

Raman spectroscopy of single cyanobacteria cell with a portable Raman system coupled with the Raman Video Microsampling System (BAC151B) allowed assessing cyanobacteria specimens from the optical field. Although their motility is reduced during water evaporation on the hydrophobic plate, during laser exposure a motility drift was discernable. However, their spectra revealed the typical bands observed at 1522 and 1158 cm^{-1} upon substantial fluorescence background.

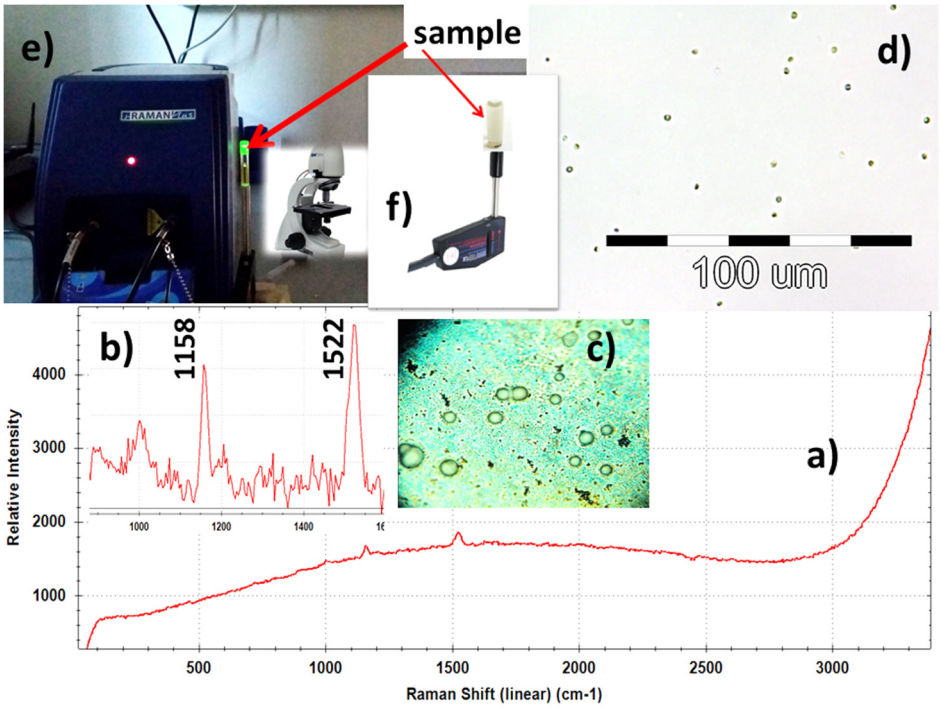

Fig. 3. Raman spectrum of single cyanobacteria (Synechocystis sp. AICB 51 strain a) collected through the Raman Video Micro-sampling System (BAC151B) with the portable instrument. On passing from bulk measurement to the single cells, the trigger was coupled to the microscope equipped with a video camera. Excitation: 532 nm, 5 s acquisition. The background subtracted signal from single cell is shown in insertion (b), highlighting the two major bands characteristic to carotenoids. Micrograph of the cyanobacteria (c) deposited on a hydrophobic slide was collected with the Raman instrument video-camera and the light microscopy image obtained with an inversed optical microscope (Leica, 100x objective) is shown in d). A picture of the instrument highlighting the fiber optic probe with a detail of the trigger and a bulk sample is shown in f) insertion.

Bulk cyanobacteria Raman spectra

Typical Raman signal of bulk cyanobacteria in 1ml glass vial collected with the portable system is shown in the Fig. 4, in comparison with the Raman spectrum of the same sample collected with the lab-based system under lateral laser focus. The spectra were normalized to the total integration time in the BWSpec acquisition software.

An increased background of the bulk cyanobacteria was observed in the case of lateral illumination through the vial glass wall, in detriment of the spectral information. In the case of portable system, the trigger facility allows to set the sample vial on its top (as shown in the Fig. 3e), resulting a longer optical path through the same sample and avoiding the signal loss due to the bacteria deposition on the bottom of the vial which results in decreasing cells concentration during measurement. Regarding the possible "defense" mechanism of live cyanobacteria to avoid too strong light energy during laser exposure, the complex photochemical processes [11] could certainly influence their Raman spectroscopy as well as their fluorescence output. These aspects will be addressed elsewhere. Technically assessing, taking the same cyanobacteria sample from a lab-based Raman characterization to a portable system, an improved signal-to-noise ratio and a substantially decreased background was observed as showed in the Fig. 4.

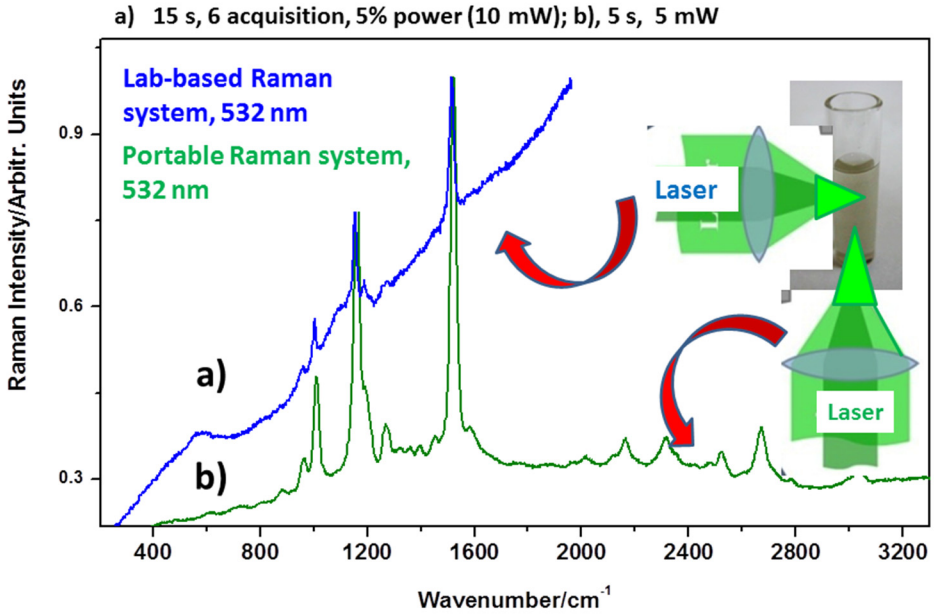

Fig. 4. Raman spectra of bulk cyanobacteria (Synechocystis sp. AICB 51 strain recorded with the lab-based Raman system, a), compared to the corresponding signal provided by the portable system b) through the bottom of a glass vial of 1 ml capacity. Excitation: 532 nm, 15 s, 6 acquisition, 10 mW (a) and 5 s, 5 mW (b).

Thus, in the high wavenumber range the overtones [8] of the carotenoids bands could be easily observed. Additional weak bands arising from other components of the bulk cells were discernable. The culture medium revealed notable band arising from the sulfate group stretching mode at 978 cm^{-1} (spectrum not shown here).

The main advantage of the portable instrument arises from the unique combination of wide spectral interval and high resolution, in the range from 65 cm^{-1} to 4000 cm^{-1}, enabling one step fast measurement both in the low and high spectral range. The detection is achieved with a high quantum efficiency CCD array. Passing from micro-sampling accessory to trigger and back is fast and user friendly, requiring several seconds trivial operation. Unlike portable system, the lab-based one requires longer time for setting the experimental acquisition, impose longer acquisition time when all the spectral range (100-3600 cm^{-1}) is envisaged, making difficult Raman measurement of light sensitive samples over the whole spectral range in one acquisition. Additionally, on passing from micro-Raman to bulk liquid measurement accessory in a lab-based system is supplementary time consuming, in detriment of the experiment flexibility when dealing with live cells or large number of samples.

The flexible, lightweight design of the portable instrument and low power consumption provide substantially improved research grade Raman spectroscopy capabilities over the existing lab-based systems. Additionally, the fiber optic probe can be used with a cuvette holder, a video microscope, an XYZ positioning stage probe holder and a BWIQ multivariate analysis software and BWID identification software. The software output provides all the spectral information like peak pixel, relative intensity, Raman shift, FWHM, in just one click, thus adding enormous help for fast analysis of large number of samples. Thus, the portable instrument capability predicts a wide range of biomedical or environmental applications that certainly are under way.

CONCLUSIONS

The results clearly suggest that cyanobacteria could be instantly Raman spectroscopy characterized *in vivo* and under the 532 nm excitation, the Raman signal is consistent with the characteristic pre-resonance modes of carotenoids. Both cyanobacteria strains exhibited similar Raman modes associated to their carotenoids content, which are known to be pre-resonantly excited when the 532 nm laser line is employed. Regarding the capability of the portable instrument to promptly achieve Raman characterization of cyanobacteria, it demonstrated better performances in obtaining high quality Raman signal than the lab-based instrument, due to its optimized

technical characteristics, prompt response, complex information providing, user friendly software for data acquisition and processing and high flexibility for sampling. These capabilities combined with Raman spectroscopy user expertise, suggest further possibility to monitor cyanobacteria cultivation and growing in specific bioreactors, in a non-destructive manner, where the growing conditions are determinant for their chemical composition and carotenoids accumulation.

ACKNOWLEDGEMENT

This work was possible due to the NEWFELPRO Grant Nr. 5/2014 of the Government of the Republic of Croatia and the Ministry of Science, Education and Sport (MSES) co-financed through the Marie Curie FP7-PEOPLE-2011-COFUND. Cs. M. acknowledges the Sectorial Operational Program for Human Resources Development 2007-2013, co-financed by the European Social Fund, project nr. POSDRU/159/1.5/S/ 132400. The Babeş-Bolyai University Research Infrastructure Project financed by the Romanian Government, PN II-Capacities, Integrated Network for Interdisciplinary Research (INIR) is highly acknowledged. Special thanks to Professor N. Dragos from Biology Department of Babes-Bolyai University, Cluj-Napoca, and Dr. Stijepo Ljubimir from the Institute of Coastal and Marine Research of the University of Dubrovnik, Croatia, are acknowledged for their kindness to provide the cyanobacteria samples.

REFERENCES

1. J. Ni. Woodhouse, A. S. Kinsela, R. N. Collins, Lee Chester Bowling, G. L Honeyman, J. K Holliday and B. A. Neilan, *The ISME Journal*, (2015), doi:10.1038/ismej.2015.218.
2. V. End de Oliveiraa, M.A.C. Neves Mirandab, M. Carolina Silva Soaresc, Howell G.M. Edwardsd, Luiz Fernando Cappa de Oliveira, *Spectrochim. Acta Part A: Molecular and Biomolecular Spectroscopy*, 150, 5, 373–380 (2015).
3. Jan Jehlička, Howell G.M. Edwards and Aharon Oren, *Appl. and Env. Microbiol*., 80, 11 3286-3295, (2014).
4. Zarrouk C. Ph.D. thesis. Paris, France: University of Paris; 1966.
5. A. Mircea; M.I. Ovidiu, R. Sandulescu, N. Dragos, *Studia UBB Chemia*, 59, 4, 47 (2014).
6. T. Tarko, A. Duda-Chodak and M. Kobus, *Czech J. Food Sci.*, 30, 3, 258–267 (2012).
7. http://bwtek.com/products/i-raman/
8. S. Cintă Pinzaru, Cs. Müller, S. Tomšić, M. M. Venter, I.B. Cozar, and B. Glamuzina, *J. Raman Spectrosc.*, 46: 597–604 (2015). doi:10.1002/jrs.4713.

9. N. Tschirner, M. Schenderlein, K. Brose, E. Schlodder, M.A. Mroginski, C. Thomsen, P. Hildebrandt, *Phys. Chem. Chem. Phys*., 11, 11471 (2009).
10. N. Tschirner, M. Schenderlein, K. Brose, E. Schlodder, M.A. Mroginski, P. Hildebrandt, C. Thomsen, *Phys. Stat. Sol.* (b), 2008, 245, 2225.
11. D. Kirilovskya, C.A. Kerfeld, *Biochimica et Biophysica Acta (BBA) - Bioenergetics*, 1817, 1 (2012), 158–166. http://dx.doi.org/10.1016/j.bbabio.2011.04.013